Vapor-liquid equilibrium properties from molecular simulation and experiment

zur Erlangung des akademischen Grades eines

DOKTORS DER INGENIEURWISSENSCHAFTEN (Dr.-Ing.)

der Fakultät für Maschinenbau

der Universität Paderborn

genehmigte

DISSERTATION

von

Dipl.-Wirt.-Ing. Thorsten Windmann, M.Sc.

aus Bielefeld

Tag des Kolloquiums: 9. Dezember 2014

Referent: Prof. Dr.-Ing. Jadran Vrabec

Korreferent: Prof. Dr.-Ing. Hans Hasse

Vorwort

Die vorliegende Arbeit entstand im Rahmen meiner Tätigkeit als Wissenschaftlicher Mitarbeiter am Lehrstuhl für Thermodynamik und Energietechnik der Universität Paderborn von März 2009 bis Februar 2014. Mein besonderer Dank gilt Herrn Prof. Dr.-Ing. Jadran Vrabec, der mich betreut und in jeder Hinsicht gefördert hat. Ohne ihn wäre die Erstellung der Arbeit nicht möglich gewesen. Herrn Prof. Dr.-Ing. Hans Hasse möchte ich für die freundliche Übernahme des Koreferates danken. Weiterhin bin ich Elmar Baumhögger und Dr. Gerd Herres zu großem Dank verpflichtet. Die zahlreichen Diskussionen mit ihnen über die experimentelle sowie die theoretische Thermodynamik haben wesentlich zum Erfolg meiner Arbeit beigetragen. Dies gilt ebenso für die tatkräftige Unterstützung durch Rüdiger Pflock und Alexander Reimann, bei denen ich mich ebenfalls bedanke. Für das Gelingen der Arbeit war die Kooperation mit Kollegen aus der Wissenschaft unerlässlich. In diesem Zusammenhang gilt mein bester Dank Benjamin Bork, Prof. Dr. Chieh-Ming Hsieh, Dr. Colin Glass, Prof. Dr.-Ing. Dieter Gorenflo, Dr. Ekaterina Elts, Frithjof Dubberke, Dr. Gabor Rutkai, Dr.-Ing. Gabriela Guevara-Carrión, Illya Shevchuk, JP Dr.-Ing. Martin Horsch, Monika Thol, Steffen Reiser, Dr.-Ing. Stephan Deublein und Dr.-Ing. Thorsten Merker für eine durchweg produktive und erstklassige Zusammenarbeit. Die Arbeit mit Studierenden während meiner Zeit als Wissenschaftlicher Mitarbeiter hat mir viel Freude bereitet und vieles erleichtert. Mein herzlicher Dank gilt stellvertretend Andreas Köster, Matthias Linnemann und Philipp Komodromos für die sehr gute und enge Zusammenarbeit. Besonders hervorheben möchte ich das ausgezeichnete, kollegiale und freundschaftliche Klima im Lehrstuhlteam. Hierfür gilt mein Dank allen Kollegen. Namentlich möchte ich hier Gerrit Sonnenrein, Stefan Eckelsbach und Svetlana Miroshnichenko nennen. Für die unermüdliche Unterstützung im privaten Bereich möchte ich meinen Eltern Anita und Joachim, meinem Bruder Stefan und meiner Theda einen ganz lieben Dank aussprechen.

Detmold, im Juli 2014 Thorsten Windmann

Contents

List of Symbols

Latin letters

a, b	Parameters of the Peng-Robinson equation of state
c	Speed of sound
c_1, c_2, c_3	Mathias-Copeman parameters
c_p	Isobaric heat capacity
D_i	Self-diffusion coefficient of the component i
Δh_v	Enthalpy of vaporization
f	Helmholtz energy
f	Fugacity
$g(r)$	Radial distribution function
g^E_∞	Excess Gibbs energy at infinite pressure
h	Enthalpy
H_i	Henry's law constant of component i
k_B	Boltzmann constant
k_{ij}	Binary interaction parameter of the quadratic mixing rule
l_{ij}, l_{ji}	Binary interaction parameters of the Huron-Vidal mixing rule
m	Mass
M	Molar mass
n	Molar amount of substance
N	Number of molecules
p	Pressure
q	Point charge

Q	Quadrupole moment magnitude
r	Distance between two Lennard-Jones sites
R	Universal gas constant
T	Temperature
T_d	Desired temperature
T_m	Measured temperature
T_p	Temperature of the pressure transducer
v	Specific volume
V	Volume
x_i	Mole fraction of component i in the liquid phase
x	Cartesian direction
X_i	Measured variable
y	Mole fraction of component i in the gas phase
y	Cartesian direction
z	Axial position of the spindle press
z	Cartesian direction
Z	Measured variable

Greek letters

α	Alpha function of the Peng-Robinson equation of state
β	Isothermal compressibility
ε	Lennard-Jones energy parameter
ε_0	Permittivity of vacuum
θ	Inclination angle with respect to the z axis
λ	Thermal conductivity
μ	Dipole moment magnitude
ν	Shear viscosity
ξ	Binary interaction parameter
ρ	Density
σ	Lennard-Jones size parameter
φ	Azimuthal angle with respect to the x-z plane
φ	Fugacity coefficient
ω	Acentric factor

Subscript

0	Reference state
1	State before the filling process
2	State after the filling process
abs	Absolute
ace	Acetone
c	Critical point
cell	Measurement cell
dif	Differential
gas	Gas
i	Component *i*
j	Component *j*
liq	Liquid
m	mixture
max	Maximum
s	Saturated

Superscript

0	Ideal
$'$	Saturated liquid line
$''$	Saturated vapor line
ρ	Density
deg	Degree
eos	Equation of state
id	Ideal
L	Local
res	Residual
sim	Simulation

Vector properties

ω	Molecular orientation

Abbreviations

BMBF	Bundesministerium für Bildung und Forschung
CFC	Chlorofluorocarbon
D4	Octamethylcyclotetrasiloxane
DDB	Dortmunder Datenbank
DFG	Deutsche Forschungsgemeinschaft
EMD	Equilibrium molecular dynamics
EOS	Equation of state
GWP	Global warming potential
LJ	Lennard-Jones
MC	Monte Carlo
MD	Molecular dynamics
MDB	Merseburger Datenabank
MM	Hexamethyldisiloxane
μVT	Ensemble with constant chemical potential, constant volume and constant temperature
NIST	National Institute for Standards and Technology
NpT	Ensemble with N particles, constant pressure and constant temperature
NVE	Ensemble with N particles, constant volume and constant energy
NVT	Ensemble with N particles, constant volume and constant temperature
ODP	Ozone depletion potential
ORC	Organic Rankine cycle
PFC	Perfluorocarbons
PR	Peng-Robinson
Pt100	Platinum resistance thermometer with a basic resistance of 100 Ω
QC	Quantum chemical
RDF	Radial distribution function
$ScCO_2$	Supercritical carbon dioxide
VLE	Vapor-liquid equilibrium

Abstract

Molecular simulation is applied in combination with experimental investigations to obtain thermodynamic properties. Two newly constructed experimental apparatuses for the measurement of the vapor-liquid equilibrium (VLE) behavior of mixtures are presented. Next, a brief introduction into molecular simulation, as well as into the Peng Robinson equation of state (EOS) is given. Furthermore, the integration of the radial distribution function into the simulation tool *ms*2 is discussed.

For the mixtures nitrogen + acetone and oxygen + acetone, a set of new VLE data are generated by molecular simulation and experiment. For further applications, the Peng-Robinson EOS is adjusted to the obtained data.

In addition, new force field models are developed for the siloxanes hexamethyldisiloxane and octamethylcyclotetrasiloxane, for decafluorobutane, for hydrazine and for its derivatives monomethylhydrazine as well as 1,1-dimethylhydrazine and validated with experimental data from the literature. Unlike dispersive interactions are adjusted to experimental data from the literature for various mixtures containing the hydrazines. Furthermore, the Peng-Robinson EOS is adjusted for these mixtures. Additionally, the Henry's law constant for the solubility of different gases in liquid hydrazine, monomethylhydrazine and dimethylhydrazine is computed.

The mixture carbon dioxide + 2,2-dimethyl-1-propanol is studied by experiment. New VLE data for this mixture are reported for the two isotherms 333 and 353 K. The Peng-Robinson EOS is adjusted to these data points as well.

Zusammenfassung

In der vorliegenden Arbeit werden thermodynamische Größen durch molekulare Simulation und experimentelle Untersuchungen bestimmt. Es werden zwei neu konstruierte Versuchsanlagen vorgestellt, mit denen das Dampf-Flüssig Phasengleichgewicht (VLE) von Mischungen vermessen werden kann. Weiterhin wird eine Einführung in die molekulare Simulation gegeben, sowie die Peng-Robinson Zustandsgleichung (ZGL) diskutiert. Zudem wird die Erweiterung des Simulationstools *ms*2 mit der radialen Paarverteilungsfunktion vorgestellt.
Eine Vielzahl an neuen Daten wird mit Hilfe der molekularen Simulation und experimenteller Untersuchungen für die Mischungen Stickstoff + Aceton und Sauerstoff + Aceton gewonnen. An diese Daten wird die Peng-Robinson ZGL für weiterführende Anwendungen angepasst.
Weitere Kraftfelder werden für die beiden Siloxane Hexamethyldisiloxan und Octamethylcyclotetrasiloxan, für Decafluorobutan, sowie für Hydrazin und seine Derivate Monomethylhydrazin and 1,1-Dimethylhydrazine entwickelt und anhand von experimentellen Daten aus der Literatur validiert. Für mehrere Mischungen mit Hydrazin werden die ungleichen Wechselwirkungen und die Peng-Robinson ZGL an experimentelle Daten aus der Literatur angepasst. Zudem werden Henrykonstanten für die Löslichkeit verschiedener Gase in flüssigem Hydrazin, Monomethylhydrazin und Dimethylhydrazin berechnet.
Die Mischung Kohlenstoffdioxid + 2,2-Dimethyl-1-Propanol wird experimentell untersucht und neue VLE Daten werden für die Temperaturen 333 und 353 K angegeben. Außerdem wird die Peng-Robinson ZGL an die gemessenen Punkte angepasst.

1 Introduction

Knowledge of the behavior of materials and substances is essential in nearly all fields of engineering. An example for this is the Collaborative Research Center Transregio 75 (SFB-TRR75) [1, 2], in which various research groups examine droplet dynamics under extreme ambient conditions, as for instance the behavior of acetone droplets in a nitrogen and oxygen environment [3, 4]. For this purpose, vapor-liquid equilibrium (VLE) data of the binary mixtures nitrogen + acetone and oxygen + acetone are needed. The SFB-TRR75 is not the only example. Further projects which depend on the knowledge of the fluid behavior are presented below. Thus, the aim of the present work was to support these projects with the required thermodynamic VLE properties.
Molecular simulation as an innovative method was used in addition to experiments to obtain thermodynamic properties in this work. In this simulation approach, a force field model is used to describe the behavior of the molecules that build up a fluid. The model describes the intermolecular interactions with the Lennard-Jones (LJ) potential for the attractive and repulsive interactions and with Coulomb's law for the electrostatic interactions. In nearly all cases it is cheaper to carry out a simulation than an experiment and with the ever rising computing power of supercomputers, even large and complex systems, where a huge number of computing operations have to be executed, can be simulated on a satisfying time scale. Further advantages of molecular simulation are:

- Explosive, flammable or toxic substances can be studied without any extra effort.
- The application to mixtures is straightforward, if force field models for the pure substances are available.
- The extra- and interpolation capability is good.
- All model parameters have a physical meaning.
- Only few experimental data are necessary to adjust the model parameters.

Because of the discussed advantages, molecular simulation is very suitable to obtain thermodynamic properties. However, experiments are still necessary, e.g. to adjust and validate force field models.

New experiments were carried out to study the VLE behavior of the binary mixtures nitrogen + acetone, oxygen + acetone and carbon dioxide + 2,2-dimethyl-1-propanol over a wide temperature and pressure range. For this task, two new experimental apparatuses were constructed and built up. These setups were designed to investigate the saturated liquid line of mixtures in a temperature range from 203.15 to 600 K up to a pressure of 70 MPa (cf. Sections 2.1 and 2.2). To measure the saturated vapor line, an existing experimental setup was used. Here, the challenge was to extract a gaseous sample and analyze it with a mass spectrometer (cf. Section 2.3).
An introduction to molecular simulation is given in Section 3. There, the present modelling strategy is explained. Furthermore, the modelling of mixtures is discussed.
The Peng-Robinson equation of state (EOS) [5] was used to aggregate simulation and experimental data for further applications. This type of cubic EOS is frequently used in the chemical industry. In Section 4, a short summary of the Peng-Robinson EOS, regarding two alpha functions and two mixing rules, is given. In addition, the calculation of the enthalpy for pure fluids and mixtures based on the Peng-Robinson EOS is explained. The enthalpy is important for many applications, such as the examination of droplets which are surrounded with air by means of computational fluid dynamics calculations within the framework of the above introduced TRR75 project.
To calculate thermodynamic properties with molecular simulation, a multitude of computer operations have to be executed in a short time and thus an efficient computer code in the form of a simulation tool is needed. In this work, the simulation tool *ms*2 [6] was used to carry out molecular simulations. In addition, the functionality of *ms*2 was extended by integrating the radial distribution function (RDF) (cf. Section 5). This implementation of the RDF was carried out to offer the possibility to study the structure of fluids, especially of mixtures. A concrete example is the study of alkali and halide ions in aqueous solutions [7].
As described above, molecular simulation and experiment as well as the Peng-Robinson EOS were applied in the present work in order to make a major contribution to various research projects. An example for this is the SFB-TRR75. In this project, VLE data of the binary mixtures nitrogen + acetone and oxygen + acetone were needed. The main part of the present work deals with the study of these two systems by molecular simulation and experiment as well as with the subsequent aggregation of the obtained data, which were provided to the other SFB-TRR75 members in form of the Peng-Robinson EOS. For this purpose, a new force field model for pure acetone was developed and validated. The unlike dispersive inter-

action between nitrogen + acetone as well as oxygen + acetone was adjusted. Furthermore, VLE data were obtained in a wide temperature and pressure range for nitrogen + acetone and, due to safety issues, at low temperatures and pressures for oxygen + acetone by experiment and molecular simulation. The Peng-Robinson EOS was adjusted to these data. Detailed information on this work are given in Section 6.
Another example is the project "Equation of state based on hybrid data sets – a combined approach for the development of fundamental equations of state and of accurate molecular models" which is funded by Deutsche Forschungsgemeinschaft (DFG). In this project, EOS based on the Helmholtz energy are adjusted to experimental data and simulation data in combination. One of the first so called "hybrid EOS" is being developed for the two siloxanes hexamethyldisiloxane (MM) and octamethylcyclotetrasiloxane (D4). For this task, pure fluid force field models of these substances are necessary. Hence, in the present work new force field models for MM and D4 were developed and validated (Section 7). The accomplished work provides advantages for another project of our group, in which the Organic Rankine Cycle (ORC) is investigated as well. On the one hand, the new hybrid EOS can be used here to calculate thermodynamic properties, if MM or D4 are applied as working fluids in the cycle. On the other hand, the force field models can be used to predict properties of mixtures, which may be used as a working fluid as well.
Within the project "Development of a database and predictive models for new alternative refrigerants", diverse alternative refrigerants are examined in collaboration with groups from Oldenburg, Germany and Durban, South Africa. Due to the fact that pure fluids and various mixtures are considered, molecular simulation is ideal for this purpose. Numerous simulations can be carried out in a short amount of time without the need of much experimental effort. As an example, a new force field model for the potential refrigerant decafluorobutane was developed and verified in the present work (cf. Section 8). With this model, the basis for further examinations of mixtures containing decafluorobutane with molecular simulation was established.

The present work points out the advantage of having the opportunity to use two independent methods to obtain thermodynamic properties. The choice which of these methods is used for the respective study depends on the challenges that are determined by the substances. An example for this is the contribution made to the project "Understanding the role of electrostatic and dispersive interactions in fluid phase equilibria: A step towards fast and accurate first-principles predictions" which was funded by the Alexander von Humboldt Stiftung. In this project, a new COSMO-SAC model [8] was developed and had to be validated. Among others, VLE data of the mixture carbon dioxide + 2,2-dimethyl-1-propanol were needed for this task. Due to the fact that the 2,2-dimethyl-1-propanolare molecule is complex and its

internal degrees of freedom must be considered in the force field model, the molecule could not be simulated with the simulation tool *ms*2 in this work. Thus, exclusively the experimental approach was chosen for this mixture. In the present work, an existing experimental setup was extended to be adequate for these measurements. Experimental work was carried out for the saturated liquid line of CO_2 + 2,2-dimethyl-1-propanol for three isotherms (cf. Section 9).

The study of the substances hydrazine and its two derivatives monomethylhydrazine and 1,1-dimethylhydrazine is an example of the opposite situation, where molecular simulation was chosen instead of experiment. This choice was made, because hydrazine and its derivatives are toxic, cancerogenic, explosive and flammable. Obviously, experiments would be very tedious here. In the present work, new molecular models for hydrazine, monomethylhydrazine and 1,1-dimethylhydrazine were developed and validated on the basis of existing experimental data. The simplicity of molecular modeling and simulation of mixtures is pointed out in this work, too. Thus, various mixtures containing the three hydrazines were studied (cf. Section 10).

2 Experimental setups for vapor-liquid equilibrium measurements

In this work the VLE behavior of the binary mixtures nitrogen + acetone, oxygen + acetone and carbon dioxide + 2,2-dimethyl-1-propanol was determined by experiment. The saturated liquid lines of nitrogen + acetone at isotherms between 223 and 283 K, of oxygen + acetone at 253 and 283 K and of carbon dioxide + 2,2-dimethyl-1-propanol at 333 and 353 K were measured with a newly built apparatus which works on the basis of the synthetic measurement method. The synthetic method is characterized by the knowledge of the composition of the observed mixture in the measurement cell and the boiling point is reached by varying the pressure or the temperature. Hence no sample removal from the cell is necessary to determine the composition. As a result, the synthetic method is particularly suitable for measurements in the transcritical region and for measurements with a small amount of gas in the saturated liquid phase (gas solubility measurement) [9]. The experimental setup and the measurement procedure are described in detail in Section 2.1.

Due to the fact that the discussed experimental setup is suitable for temperatures between 213 and 403 K and a maximum pressure of 20 MPa, a new synthetic apparatus for measurements at high temperatures and high pressures was constructed and built up (cf. Section 2.2 for details). It was used for measurements of the saturated liquid line of nitrogen + acetone in the transcritical region at isotherms above 400 K and maximum pressures of about 40 MPa.

Since the two newly built apparatuses were only suitable to measure the saturated liquid line, the saturated vapor line of the system nitrogen + acetone at 303, 323 and 343 K was determined with an experimental setup which was available in our group. It operates on the basis of the analytic measurement method. In the case of the analytic method, the studied mixture is in the measurement cell in the state of vapor-liquid equilibrium, where both phases have a finite volume. To determine the composition of a phase, a small sample has to be taken from the cell and analyzed, for example with a mass spectrometer. Details for this apparatus are given in Section 2.3.

2.1 Synthetic apparatus for measurements at low temperatures

2.1.1 Experimental setup

Figure 1 shows the apparatus for the measurement of the VLE at temperatures below 400 K, which is based on equipment by Rumpf and Maurer [10, 11]. Its main part is a thermostated high pressure equilibrium cell with two gauge glasses mounted on the front walls. The cell has an internal volume of about 28.8 cm^3 and was tested for leak tightness at temperatures from 203.15 to 403.15 K and a maximum pressure of 20 MPa. A magnetic stirrer was placed inside the cell to speed up the equilibration process during the experimental procedure. The cell can be loaded with fluids in the gaseous and liquid state via the tree-way valve TW-V2 at the upper side, cf. Figure 1. For this purpose, a gas bottle and a high pressure spindle press were connected to TW-V2. The spindle press is linked to a liquid reservoir. To achieve a constant temperature in all functional units, the apparatus was surrounded by an insulated chamber with an additional thermostat cycle.

The temperature in the cell was measured by two calibrated platinum resistance thermometers with a basic resistance of 100 Ω (Pt100). Furthermore, one additional Pt100 thermometer was attached to the spindle press. To calibrate these thermometers, a more precise platinum resistance thermometer with a basic resistance of 25 Ω was used. The temperature measuring error was about ± 0.04 K.

Two calibrated pressure transducers (model Super TJE, Honeywell test & measurement, measuring ranges: 6.8 and 20 MPa for the measurements of nitrogen + acetone and 0.2 and 1.2 MPa for the measurements of oxygen + acetone) were used to determine the pressure of the pure gaseous solute and the pressure of the liquid mixture. A deadweight tester (series 5201, Desgranges & Huot) was employed to calibrate the transducers. The accuracy of these transducers is specified to be 0.05 % of their respective full measuring scale.

2.1.2 Measurement procedure

The measurement procedure that is described in the following was adopted from Rumpf and Maurer [10, 11]. In the first step, the high pressure equilibrium cell was filled with the gaseous component (e.g. nitrogen) from the gas bottle. The mass of the gaseous component was calculated volumetrically from the known cell volume and the density of the gaseous component in the cell. Therefore, the temperature and pressure were measured and the density was determined via an EOS by Span *et al.* [12] for nitrogen or an EOS by Schmidt and

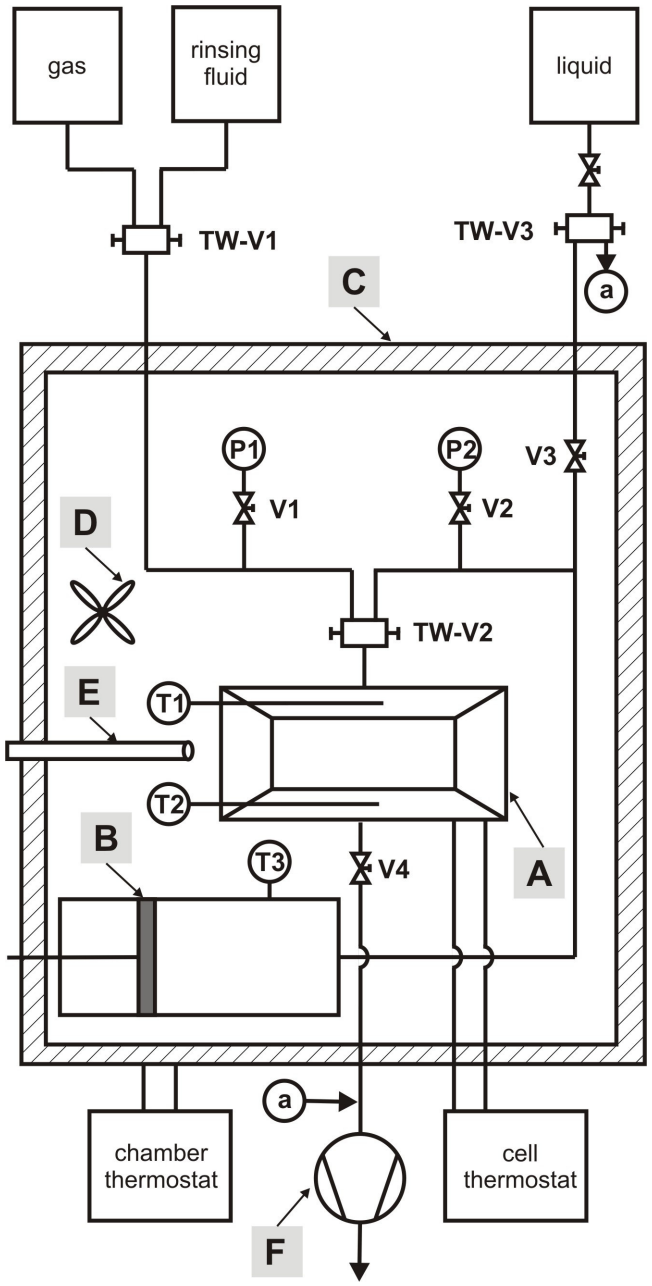

Figure 1: Schematic of the synthetic apparatus for measurements of the saturated liquid line at low temperatures. VX indicates a valve, TW-VX a three-way valve, TX a thermometer and PX a pressure transducer. A: high pressure equilibrium cell, B: high pressure spindle press, C: insulated chamber, D: fan, E: endoscope, F: vacuum pump.

Wagner [13] for oxygen. In the second step, the liquid solvent (acetone) was added into the cell with the high pressure spindle press until the gas was completely dissolved. The associated equilibration process was observed through the gauge glass with an endoscope. Subsequently, small amounts of the liquid mixture were withdrawn from the cell to reduce the pressure until the formation of small gas bubbles in the mixture indicated the saturated liquid state point. By comparing the positions of the spindle press before and after the experiment, the volume of the injected solvent was determined and its mass m_{ace} in the cell was calculated as follows

$$m_{\mathrm{ace}} = \rho_1(T_1, p_1) \cdot V_1(z_1) - \rho_2(T_2, p_2) \cdot V_2(z_2), \tag{1}$$

wherein p is the pressure (measured with P2), T the temperature (measured with T1 and T2), ρ the pure acetone density calculated with an EOS for acetone by Lemmon and Span [14] and V the volume of the spindle press which depends on its axial position z. The indices 1 and 2 represent the state before and after the filling process, respectively. Note that the three EOS [12–14] are highly accurate multiparameter models that can be regarded as best practice for these pure fluids.

2.2 Synthetic apparatus for measurements at high temperatures and high pressures

2.2.1 Experimental setup

The experimental setup for the VLE measurements of nitrogen + acetone at temperatures above 400 K and a maximum pressure of about 40 MPa is shown in Figure 2. It is a further development of the apparatus described in Section 2.1.1. Its main part again is a cylindrical high pressure equilibrium cell made of V4a stainless steel, which has an internal volume of approximately 14 ml. A magnetic stirrer was placed into the cell. To visually observe phase separation inside, two sapphire gauge-glasses were mounted at the front and the back of the cylinder. The cell was constructed for temperatures of up to 600 K and pressures of up to 70 MPa. For this purpose, it was screwed together with eight expansion bolts and seven cup springs placed on each bolt, respectively. The cell was embedded in a copper cylinder electrical heating. In this way, the temperature can be controlled effectively and automatically. To avoid heat loss due to radiation, the cell was surrounded by an aluminum cylinder with its own electrical heating. The whole setup was placed in a vacuum chamber to reduce heat loss due to convection. Moreover, the vacuum atmosphere was useful to prohibit

corrosion or ice formation at low temperatures.
The cell was loaded via a three-way valve mounted at the top, cf. Figure 2. A gas bottle was connected to the left access (V1a) to load the gaseous component. The liquid component was loaded via a high pressure spindle press which was linked to the right access (V1b). The high pressure pump was connected to a liquid reservoir via valve V3. Valve V5 was used to purge the cell or to connect it to a vacuum pump.
The pressure transducers P1 and P2 were used to measure the pressure of the gaseous and the liquid component in the supply pipes during the loading process. The pressure in the cell was determined with the pressure transducer P3, which was possible even if valve V4 was closed. The accuracy of all employed pressure transducers (model Super TJE, Honeywell test & measurement) was given as 0.1 % of their respective full measuring scales. The measuring scales were 20, 100 and 70 MPa for P1, P2 and P3, respectively.
For the temperature measurement, five calibrated platinum resistance thermometers with a basic resistance of 100 Ω (Pt100) were installed in the apparatus. The temperature of the fluid in the cell and in the high pressure pump was measured with the Pt100 thermometers T1 and T2, respectively. The temperature of the aluminum cylinder was determined with T4. The thermometers T3 and T5 were exclusively used to control the temperature of the cell and of the aluminum cylinder, respectively. To calibrate the employed thermometers, a more precise platinum resistance thermometer with a basic resistance of 25 Ω was employed. The temperature measuring error was about ± 0.04 K.

2.2.2 Measurement procedure

The measurement procedure for the high temperature and high pressure apparatus was based on the procedure at low temperatures (cf. Section 2.1.2). However, it was changed such that no liquid mixture was withdrawn from the cell to achieve the saturated state due to the resulting pressure decrease. Instead, the saturated state was achieved by decreasing the temperature.
Before loading the components of the studied mixture into the cell, the whole setup, including the supply pipes, was evacuated and thermostated close to the ambient temperature. Then, the gaseous component (nitrogen) was filled into the cell from the gas bottle. The density of nitrogen was calculated with the EOS by Span *et al.* [12] on the basis of the measured temperature and pressure. With the density from the EOS and the known cell volume, the mass of nitrogen m_{N2} in the cell was calculated. Next, the liquid component (acetone) was added into the cell with the calibrated spindle press. To achieve a homogeneous mixture, a magnetic stirrer was operated and the cell was heated up to a temperature which was

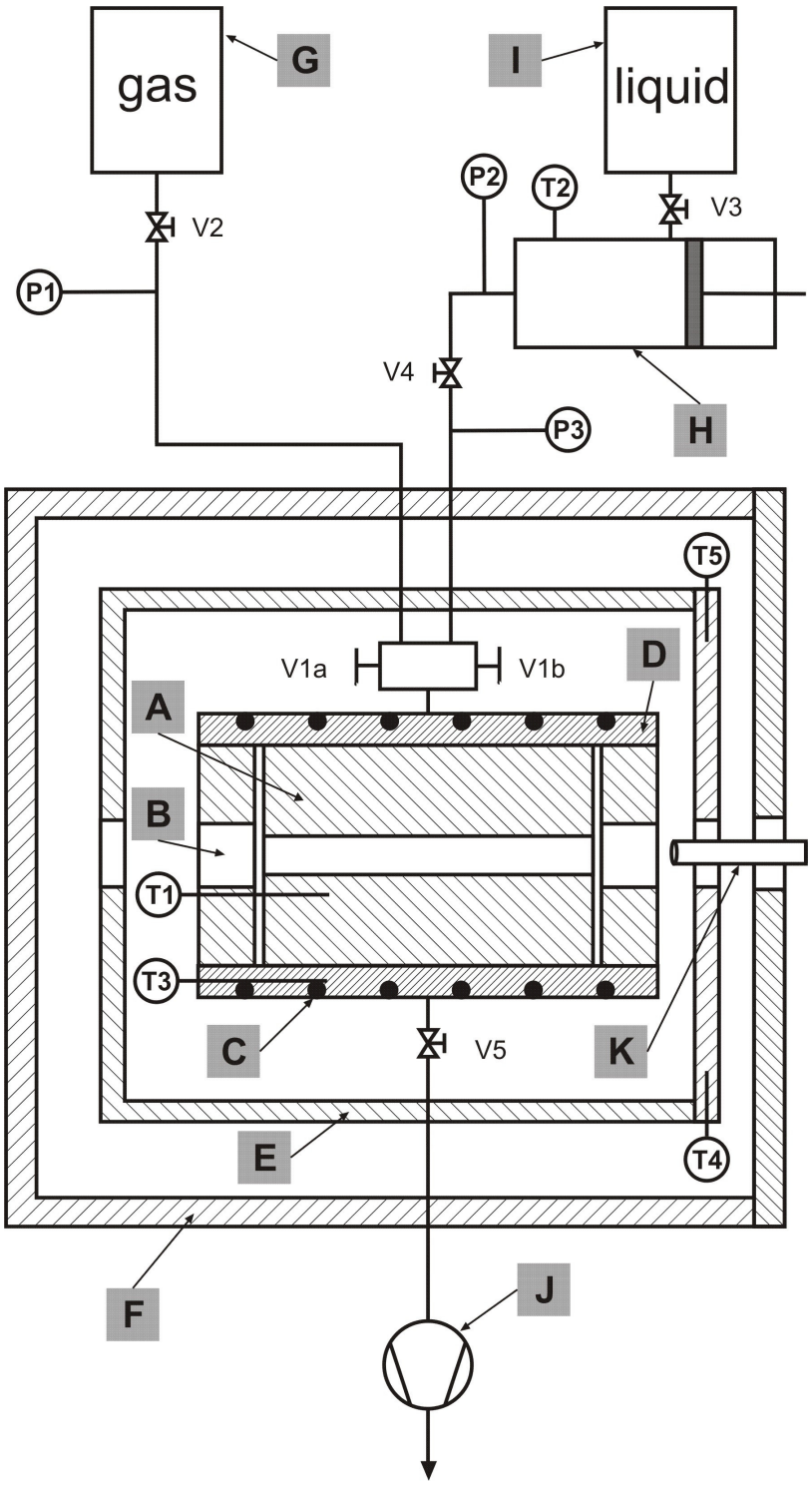

Figure 2: Schematic of the synthetic apparatus for measurements of the saturated liquid line at high temperatures and high pressures. VX indicates a valve, TX a thermometer and PX a pressure transducer. A: high pressure equilibrium cell, B: gauge-glass, C: heating wire, D: copper cylinder, E: aluminum cylinder, F: vacuum chamber, G: gas bottle, H: high pressure spindle press, I: liquid reservoir, J: vacuum pump, K: endoscope.

about 20 K above the desired measuring temperature T_d. The mixing process was visually inspected with an endoscope and it was completed when all gas bubbles disappeared. At this point, the mixture was in a homogeneous state.
In a next step, the cell was slowly cooled down towards T_d, with the aim to reach the saturated liquid state in the vicinity of the temperature T_d. In this case, the measured pressure is the saturated vapor pressure of the mixture with a specified liquid composition at T_d. However, usually saturation precisely at T_d could not be reached with the present procedure. Therefore, several iterations were typically necessary, which are described in the following.
From a homogeneous fluid state, the cell was slowly cooled down towards the desired measuring temperature T_d. During this cooling process, the pressure of the mixture was measured with the pressure transducer P3 and plotted over time with the measurement program. At a certain temperature, the first small bubbles appeared and the slope of the pressure-time plot changed significantly. At this temperature, the mixture in the cell had reached the saturated liquid state. If the cell temperature was near T_d, the measured pressure was noted as the saturated vapor pressure of the mixture. Otherwise, if the cell temperature was significantly above T_d when the bubbles appeared, the amount of acetone in the cell was too small. In this case, more acetone was added into the cell with the spindle press. This procedure, namely adding more acetone into the cell, raising the cell temperature by about 20 K, waiting for equilibration and then cooling it down until bubbles appeared, was repeated until the cell temperature was near the desired measuring temperature T_d when the mixture reached saturation.
In the last step, the mass of acetone m_{ace}, which was filled into the cell, was determined with Equation (1). Knowing the masses of nitrogen m_{N2} and acetone m_{ace}, the mole fraction x_{N2} of the mixture can be determined straightforwardly.

2.3 Analytic apparatus for the saturated vapor line measurements

2.3.1 Experimental setup

The saturated vapor line of nitrogen + acetone was determined analytically with an experimental setup which was built in prior work of our group [15], cf. Figure 3. The applied cylindrical measurement cell had two gauge-glasses at its two ends and was constructed for pressures up to 5 MPa. During the experiment, the observed mixture in the cell is in the VLE state, where both phases are present in a finite quantity. The gas and the liquid phase were

recirculated with two micro membrane pumps, respectively. Hereby, a small amount of the gas phase can be bypassed via a manifold valve into a heated sample container. Due to this procedure, it is possible to take a sample from the gas phase at the measurement temperature T_m. The whole experimental setup was placed in a climate chamber, which was divided into three temperature zones. In the middle zone, the temperature was controlled to T_m. To prevent condensation or vaporization, the left zone was overheated and the right zone was sub-cooled with respect to T_m. The vapor pressure of the observed mixture was measured with a differential pressure transducer combined with a hydraulic system and a pressure transducer to measure the absolute pressure. Two calibrated Pt100 thermometers were used to determine the temperature of the vapor and liquid phase. Details of the temperature and pressure measurement were described by Gremer [15].

2.3.2 Measurement procedure

The measurement process was based on the procedure described by Gremer [15]. After purging and evacuating the whole experimental setup, the two components of the mixture nitrogen + acetone were filled into the measurement cell via a filling pipe. First, the measurement cell was loaded with liquid acetone, then gaseous nitrogen was added directly from a gas bottle. To reach the desired measurement temperature T_m in the cell, the air temperature in the climate chamber was controlled by an electrical heater and heat exchanger which was connected to an external cooling unit. By turning on the magnetic stirrer and the membrane pumps, the equilibration process in the cell was speeded up. Phase equilibrium was assumed when the measured temperatures of the liquid and of the gas phase deviated by less than 0.01 K from the desired measurement temperature T_m for more than ten minutes and when the vapor pressure was constant. In the equilibrium state, the vapor pressure was measured with the differential pressure transducer and the gas phase composition was determined by using a mass spectrometer. For this purpose, an amount of about 0.2 g of the gas phase was routed into a sample container via the manifold valve.

2.4 Error analysis

The absolute errors of the respective measured variables were estimated by an error analysis. If necessary, the error propagation law was applied so that die absolute error of the measured variable $Z = Z(X_1, X_2, \ldots, X_N)$, which is a function of N other measured variables X_i, can be written as [16]

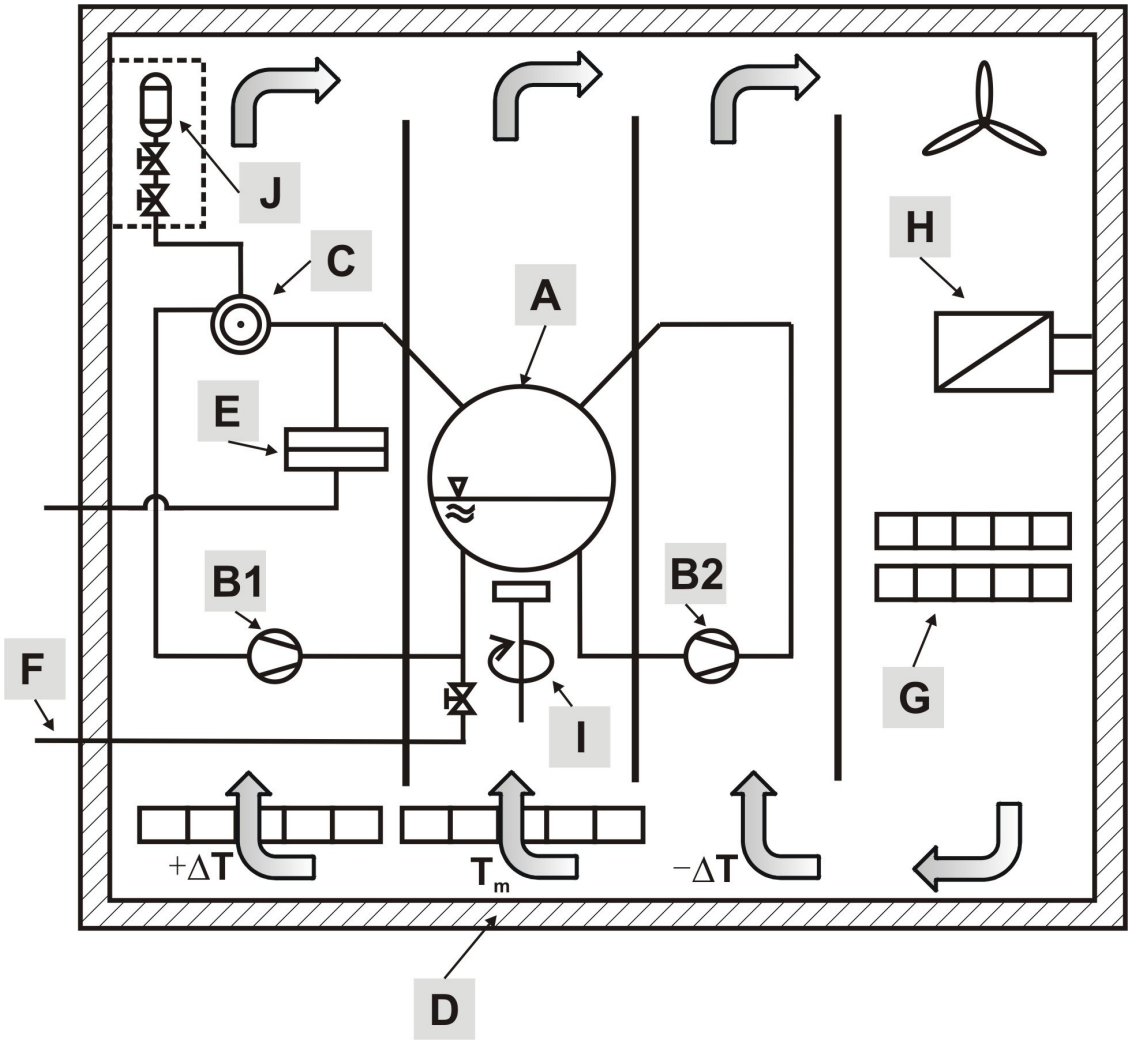

Figure 3: Schematic of the analytic apparatus for measurements of the saturated vapor line. A: measurement cell, B1, B2: micro membrane pumps, C: manifold valve, D: climate chamber, E: differential pressure transducer, F: filling pipe, G: electrical heater, H: heat exchanger, I: magnetic stirrer, J: sample container.

$$\Delta Z = \sqrt{\sum_{i=1}^{N} \left(\frac{\partial Z}{\partial X_i} \right)^2 \Delta X_i^2}. \tag{2}$$

Herein, ΔX_i is the absolute error of X_i.

In the following, the particular errors for the synthetic (cf. Sections 2.1 and 2.2) and analytic (cf. Section 2.3) measurement methods are described in detail.

2.4.1 Synthetic method

Pressure

In this work, the pressure transducers Super TJE from Honeywell test & measurement were used throughout. For these models the maximum pressure error is stated by the manufacturer to be

$$\Delta p = \beta \cdot p_{max}, \tag{3}$$

where p_{max} is the full measurement range of the pressure transducer. β depends on the measurement range p_{max} and on the temperature T_p of the pressure transducer during the measurement process. For pressure transducers with $p_{max} \leq 20$ MPa and 283 K < T_p < 303 K, β = 0.05 %, elsewhere β = 0.1 % (according to the manufacturer).

Temperature

The temperature was measured with platinum resistance thermometers with a basic resistance of 100 Ω at 0°C (Pt100) delivered by Merz Messfühlertechnik. Due to the fact that the measurement error stated by the manufacturer is only valid for the delivery condition, the error has to be determined from a calibration process. Therefrom, the absolute temperature error was estimated to be

$$\Delta T = 0.04 \text{ K}. \tag{4}$$

Density

The density of the gaseous and liquid fluid in the measurement cell at the temperature T and the pressure p was calculated with high accuracy EOS on basis of the measured values for T and p. Thus the absolute density error was

$$\Delta\rho = \sqrt{(\Delta\rho^{eos})^2 + (\Delta\rho^{p,T})^2} = \sqrt{(\Delta\rho^{eos})^2 + \left(\frac{\partial\rho}{\partial p}\right)_T^2 \Delta p^2 + \left(\frac{\partial\rho}{\partial T}\right)_\rho^2 \Delta T^2}. \tag{5}$$

Hereby $\Delta\rho^{eos}$ is the stated absolute error of the used EOS in terms of the density, $\Delta\rho^{T,p}$ is the absolute density error caused by the pressure error Δp and the temperature error ΔT (cf. Equations (3) and (4)) and can be written with the use of Equation (2) and following the error propagation law. The two derivations $\left(\frac{\partial\rho}{\partial p}\right)_T$ and $\left(\frac{\partial\rho}{\partial T}\right)_\rho$ were calculated from the respective EOS.

Cell volume

Based on the calibration process, the relative error of the cell volume V_{cell} was estimated to be 0.4 % of V_{cell}. Thus, the absolute error of the cell volume was

$$\Delta V_{cell} = 0.004 \cdot V_{cell}. \tag{6}$$

Mass of the gaseous component

The mass of the gaseous component in the measurement cell in saturated state was determined from the gas density ρ_{gas} and the cell volume V_{cell} as

$$m_{gas} = \rho_{gas} \cdot V_{cell}. \tag{7}$$

Thus the absolute error of m_{gas} was calculated with Equation (2) considering the density and cell volume error

$$\begin{aligned}\Delta m_{gas} &= \sqrt{\left(\frac{\partial m_{gas}}{\partial V_{cell}}\right)^2 \Delta V_{cell}^2 + \left(\frac{\partial m_{gas}}{\partial \rho_{gas}}\right)^2 \Delta\rho_{gas}^2} \\ &= \sqrt{\rho_{gas}^2 \cdot \Delta V_{cell}^2 + V_{cell}^2 \cdot \Delta\rho_{gas}^2} = m_{gas} \cdot \sqrt{\left(\frac{\Delta V_{cell}}{V_{cell}}\right)^2 + \left(\frac{\Delta\rho_{gas}}{\rho_{gas}}\right)^2},\end{aligned} \tag{8}$$

wherein ΔV_{cell} and $\Delta\rho_{gas}$ were obtained by Equations (5) and (6), respectively.

Mass of the liquid component

The mass of the liquid component in the measurement cell in the saturated state m_{liq} was calculated by Equation (1) from the density of the liquid component in the spindle press ρ_1 before the filling process and ρ_2 after the filling process and the volume of the spindle press before V_1 and after V_2. Using Equations (1) and (2), the absolute error of m_{liq} due to the density error $\Delta\rho_i$ and the error of the spindle press volume ΔV_{sp} was calculated as

$$\Delta m_{liq} = \sqrt{V_1^2\Delta\rho_1^2 - V_2^2\Delta\rho_2^2 + \rho_1^2\Delta V_{sp}^2 - \rho_2^2\Delta V_{sp}^2}. \tag{9}$$

Due to the fact that it was sought to employ the same state of the liquid in the pump before and after the filling process, $\rho = \rho_1 = \rho_2$ was assumed. Hence, Equation (9) simplifies to

$$\Delta m_{liq} = \sqrt{\left(V_1^2 - V_2^2\right)\Delta\rho^2}. \tag{10}$$

The error of the spindle press volume was not considered here. $\Delta\rho$ was calculated with Equation (5).

Mole fraction of the gaseous component in the liquid saturated phase

The mole fraction of the gaseous component in the measurement cell in the saturated liquid state was calculated as

$$x_{gas} = \frac{n_{gas}}{n_{gas} + n_{liq}} = \frac{m_{gas}/M_{gas}}{m_{liq}/M_{liq}}, \tag{11}$$

where n is the amount of substance, m the mass and M the molar mass.

The absolute error of x_{gas} was calculated with Equation (2)

$$\sqrt{\left(\frac{\partial x_{gas}}{\partial m_{gas}}\Delta m_{gas}\right)^2 + \left(\frac{\partial x_{gas}}{\partial m_{liq}}\Delta m_{liq}\right)^2}, \tag{12}$$

with

$$\frac{\partial x_{gas}}{\partial m_{gas}} = \frac{\frac{m_{liq}}{M_{gas}M_{liq}}}{\left(\frac{m_{gas}}{M_{gas}} + \frac{m_{liq}}{M_{liq}}\right)^2}, \tag{13}$$

and analogously the other derivative. Δm_{gas} and Δm_{liq} were taken from Equations (8) and (10).

2.4.2 Analytic method

Pressure

The absolute pressure error was calculated from the absolute error of the pressure transducer to measure the absolute pressure Δp_{abs} and the absolute error of the differential pressure transducer Δp_{dif} as follows

$$\Delta p = \sqrt{(\Delta p_{abs})^2 + (\Delta p_{dif})^2}. \tag{14}$$

Hereby Δp_{abs} was calculated from Equation (3) and Δp_{dif} was specified to be 10 Pa, cf. [15].

Temperature

As described in Section 2.4.1, the absolute temperature error was 0.04 K for all Pt100 thermometers used in this work.

Mole fraction of the gaseous component in the saturated vapor phase

On basis of the results obtained from the gas chromatograph calibration, the absolute error of the mole fraction of the gaseous component in the saturated vapor phase y_{gas} was estimated to be

$$\Delta y_{gas} = 0.01 \cdot (-1.244 \cdot y_{gas} + 1.193) \text{ mol/mol}. \tag{15}$$

3 Molecular simulation

An important concept of molecular simulation is to calculate thermodynamic properties (macroscopic level) of a substance from a multitude of configurations of the molecules that constitute the substance (microscopic level). Hereby, the connection between macroscopic and microscopic level is established by statistical mechanics. To improve statistical accuracy, as much configurations as possible have to be generated using one of the common simulation techniques MD or MC. MD is a deterministic approach where Newton's equations of motion are solved for all molecules in a time-discretized manner, whereas the idea of the MC technique is to generate the microscopic molecular configurations stochastically. For both MD and MC it is crucial to have knowledge about the molecular interaction potentials. These interactions between the molecules are described by a force field model. It is common to describe the dispersive and repulsive interactions with the LJ potential and the electrostatic interactions with point charges which can be condensed to point dipoles or quadrupoles in some cases. Within the scope of the present work, force field models for various substances were developed. The applied modelling strategy is discussed in detail in Section 3.1.
Typically 500 to 4000 molecules are sufficient to obtain reliable thermodynamic properties from molecular simulation. At the beginning of a simulation run, these molecules are positioned in the simulation volume in a specified inertial configuration. The employed ensemble determines which properties are independent. Generic is the NVE ensemble, where the number of molecules, the volume and the energy is held constant. However, for practical applications, the NpT and the NVT ensembles are often a better choice, because temperature and pressure are easier to attain. To minimize boundary effects and computing resources, concepts like the periodical boundary condition, the minimum-image-convention and the cutoff radius are widely used.
In general, any thermodynamic property, like thermal properties, caloric properties, transport properties and the Henry's law constant can be calculated by molecular simulation. Especially the possibility to carry out molecular simulations for the VLE should be emphasized here. VLE data are very important to adjust pure fluid force field models and binary mixture parameters (cf. Section 3.2). Here, the Grand Equilibrium method [17] and the $NpT+$ test particle method [18] in an extended version were used for VLE simulations.

3.1 Force field models for pure fluids

In this work, solely rigid and non-polarizable force field models were developed, which consider the dispersive, repulsive and electrostatic interactions between the molecules. The dispersive and repulsive interactions were described by the LJ 12-6 potential and the electrostatic interactions by a combination of point charges, point dipoles and point quadrupoles. The total intermolecular interaction energy thus writes as [19]

$$
\begin{aligned}
U = \sum_{i=1}^{N-1} \sum_{j=i+1}^{N} \left\{ \sum_{a=1}^{S_i^{LJ}} \sum_{b=1}^{S_j^{LJ}} 4\varepsilon_{ijab} \left[\left(\frac{\sigma_{ijab}}{r_{ijab}} \right)^{12} - \left(\frac{\sigma_{ijab}}{r_{ijab}} \right)^{6} \right] + \right. \\
\sum_{c=1}^{S_i^e} \sum_{d=1}^{S_j^e} \frac{1}{4\pi\varepsilon_0} \left[\frac{q_{ic} q_{jd}}{r_{ijcd}} + \frac{q_{ic}\mu_{jd} + \mu_{ic} q_{jd}}{r_{ijcd}^2} \cdot f_1\left(\boldsymbol{\omega}_i, \boldsymbol{\omega}_j\right) + \frac{q_{ic} Q_{jd} + Q_{ic} q_{jd}}{r_{ijcd}^3} \cdot f_2\left(\boldsymbol{\omega}_i, \boldsymbol{\omega}_j\right) + \right. \\
\left. \left. \frac{\mu_{ic}\mu_{jd}}{r_{ijcd}^3} \cdot f_3\left(\boldsymbol{\omega}_i, \boldsymbol{\omega}_j\right) + \frac{\mu_{ic} Q_{jd} + Q_{ic}\mu_{jd}}{r_{ijcd}^4} \cdot f_4\left(\boldsymbol{\omega}_i, \boldsymbol{\omega}_j\right) + \frac{Q_{ic} Q_{jd}}{r_{ijcd}^5} \cdot f_5\left(\boldsymbol{\omega}_i, \boldsymbol{\omega}_j\right) \right] ,
\end{aligned}
\tag{16}
$$

where r_{ijab}, ε_{ijab} and σ_{ijab} are the distance, the LJ energy parameter and the LJ size parameter, respectively, for the pair-wise interaction between LJ site a on molecule i and LJ site b on molecule j. The permittivity of the vacuum is ε_0, whereas q_{ic}, μ_{ic} and Q_{ic} denote the point charge magnitude, the dipole moment and the quadrupole moment of the electrostatic interaction site c on molecule i and so forth. The expressions $f_x(\boldsymbol{\omega}_i, \boldsymbol{\omega}_j)$ stand for the dependence of the electrostatic interactions on the orientations $\boldsymbol{\omega}_i$ and $\boldsymbol{\omega}_j$ of the molecules i and j, cf. Refs. [20, 21]. Finally, the summation limits N, S_x^{LJ} and S_x^e denote the number of molecules, the number of LJ sites and the number of electrostatic sites, respectively.

3.2 Molecular simulation of mixtures

To describe binary mixtures on the basis of pairwise additive potential models, two types of interactions between the molecules have to be specified. These are the interactions between like and between unlike molecules, where the like interactions are fully known from the pure substance models.

The unlike interactions can be separated into the electrostatic contribution and the dispersive/repulsive contribution. Unlike electrostatic interactions are straightforwardly known from the laws of electrostatics. However, for the dispersive and repulsive interactions between the unlike molecules A and B, the LJ parameters σ_{AB} and ε_{AB} have to be determined.

This procedure was discussed by Schnabel *et al.* [22] in detail. The unlike LJ parameters can be written as

$$\sigma_{AB} = (\sigma_A + \sigma_B)/2, \tag{17}$$

and

$$\varepsilon_{AB} = \xi \sqrt{\varepsilon_A \cdot \varepsilon_B}, \tag{18}$$

wherein ξ is a binary interaction parameter that can be adjusted to one experimental data point of the binary mixture. The vapor pressure of the mixture or the Henry's law constant are good choices for this adjustment [23]. Table 1 summarizes the binary interaction parameters of all binary mixtures adjusted in the present work.

Table 1: Binary interaction parameter ξ of the developed molecular models as adjusted in the present work.

mixture	ξ
nitrogen + acetone	0.96
oxygen + acetone	0.905
water + hydrazine	1.3
monomethylhydrazine + water	1.3
dimethylhydrazine + water	1.3
dimethylhydrazine + hydrazine	1.01
ammonia + hydrazine	1.084
ammonia + monomethylhydrazine	1.016
ammonia + dimethylhydrazine	0.94
argon + hydrazine	1.02
nitrogen + hydrazine	1.11
argon + monomethylhydrazine	0.933
nitrogen + monomethylhydrazine	0.976
argon + dimethylhydrazine	0.945
nitrogen + dimethylhydrazine	0.955
carbone monoxide + dimethylhydrazine	1.005

4 Peng-Robinson equation of state

To correlate the experimental and simulation data generated in the present work, the Peng-Robinson equation of state (EOS) [5] was used

$$p = \frac{RT}{v-b} - \frac{a(T)}{v\cdot(v+b)+b\cdot(v-b)}. \tag{19}$$

The substance specific parameters a and b were specified as

$$a(T) = (0.45724\cdot\frac{R^2{T_c}^2}{p_c})\cdot\alpha(T), \tag{20}$$

and

$$b = 0.07780\cdot\frac{RT_c}{p_c}. \tag{21}$$

Therein, R is the ideal gas constant, v the molar volume, T_c the critical temperature and p_c the critical pressure. For the alpha function $\alpha(T)$ numerous approaches can be found in the literature. In this work, the alpha function based on the acentric factor and the Mathias-Copeman alpha function were used.

Alpha function with the acentric factor

In the original approach by Peng and Robinson [5], the alpha function is described as follows

$$\alpha(T) = [1+(0.37464+1.54226\cdot\omega-0.26992\cdot\omega^2)\cdot(1-\sqrt{\frac{T}{T_c}})]^2, \tag{22}$$

where ω is the acentric factor of the respective pure fluid.

Mathias-Copeman alpha function

The alpha function by Mathias and Copeman [24] contains the three adjustable parameters c_1, c_2 and c_3. Common is the adjustment to three data points for the vapor pressure of the

pure fluid. $\alpha(T)$ is then calculated as

$$\alpha(T) = \left[1 + c_1 \cdot \left(1 - \sqrt{\frac{T}{T_c}}\right) + c_2 \cdot \left(1 - \sqrt{\frac{T}{T_c}}\right)^2 + c_3 \cdot \left(1 - \sqrt{\frac{T}{T_c}}\right)^3\right]^2, \tag{23}$$

for $T < T_c$, and as

$$\alpha(T) = \left[1 + c_1 \cdot \left(1 - \sqrt{\frac{T}{T_c}}\right)\right]^2, \tag{24}$$

for $T > T_c$.

The pure fluid parameters for all substances considered in this work are listed in Table 2.

4.1 Mixing rules

Quadratic mixing rule

In order to describe mixtures with the Peng-Robinson EOS, the quadratic Van der Waals one-fluid mixing rule [25] was assumed. It states that the pure substance parameters a and b have to be replaced in case of a mixture by

$$a_m = \sum_i \sum_j x_i x_j a_{ij}, \tag{25}$$

and

$$b_m = \sum_i x_i b_i. \tag{26}$$

Therein, a_{ij} is defined by

$$a_{ij} = \sqrt{a_i a_j} \cdot (1 - k_{ij}), \tag{27}$$

where k_{ij} is an adjustable binary parameter to correlate experimental data.

Huron-Vidal mixing rule

Another option is the g^E mixing rule by Huron and Vidal [26]. Here, the parameter b_m can be described with Equation (26) and the parameter a_m is written as

$$a_m = b_m \left(\sum_i \frac{a_i}{b_i} x_i - \frac{g^E_\infty}{\Lambda}\right), \tag{28}$$

where Λ is

$$\Lambda = \frac{1}{2\sqrt{2}} \cdot \ln\left(\frac{2+\sqrt{2}}{2-\sqrt{2}}\right), \tag{29}$$

if the Peng-Robinson EOS is used. The excess Gibbs free energy at infinite pressure g^E_∞ can be calculated with an appropriate g^E model. In the present work, the UNIQUAC model [27] was used for this task, which requires the two binary interaction parameters l_{ij} and l_{ji}.

The binary interaction parameters for all mixtures considered in this work are listed in Table 3.

4.2 Calculation of the enthalpy

4.2.1 Pure fluids

The enthalpy h at the temperature T and the molar volume v can be calculated as [28]

$$h(T,v) = h^{id}(T) + h^{res}(T,v) + h_0, \tag{30}$$

where h_0 is the enthalpy of a reference state. The ideal part of the enthalpy is

$$h^{id}(T) = \int_{T_0}^{T} c_p^0 dT, \tag{31}$$

where c_p^0 is the isobaric heat capacity of the ideal gas. The residual part of the enthalpy can be written as

$$h^{res}(T,v) = \int_\infty^v \left\{ T\left(\frac{\partial p}{\partial T}\right)_v + v\left(\frac{\partial p}{\partial v}\right)_T \right\} dv. \tag{32}$$

Using the Peng-Robinson EOS (Equation (19)) to determine the two pressure derivatives $(\partial p/\partial T)_v$ and $(\partial p/\partial v)_T$, leads to

$$h^{res}(T,v) = \frac{RTb}{v-b} + \frac{va}{v^2+2bv-b^2} + \frac{1}{4}\frac{\sqrt{2}\cdot\left\{T\cdot\left[\frac{\partial}{\partial T}a(T)\right] - a(T)\right\}\cdot\ln\left(\frac{v+b-\sqrt{2}\cdot b}{v+b+\sqrt{2}\cdot b}\right)}{b}. \tag{33}$$

With Equations (20) and (22), the derivative of $a(T)$ with respect to the temperature is

$$\frac{\partial}{\partial T}a(T) = \frac{0.45724 \cdot R^2 T_c \cdot \left\{1 + m \cdot \left[1 - \sqrt{\frac{T}{T_c}}\right]\right\}^2}{p_c \cdot \sqrt{\frac{T}{T_c}}}, \tag{34}$$

where

$$m = (0.37464 + 1.54226 \cdot \omega - 0.26992 \cdot \omega^2). \tag{35}$$

The enthalpy of vaporization $\Delta h_v(T)$ at the temperature T can be calculated with Equation (30) as the difference of the saturated vapor enthalpy and saturated liquid enthalpy

$$\Delta h_v(T) = h(T, v'') - h(T, v'). \tag{36}$$

For this purpose the molar volumes of the saturated vapor phase v'' and of the saturated liquid phase v' have to be determined with Equation (19) in combination with an equation which considers the phase equilibrium condition, such as the Maxwell criterion [29].

4.2.2 Mixtures

To calculate the enthalpy h of a mixture at a given temperature T, molar volume v and mole fraction x, Equation (30) turns into

$$h(T, v, x) = h^{id}(T, x) + h^{res}(T, v, x) + h_0. \tag{37}$$

The ideal part of the enthalpy is written as

$$h^{id}(T, x) = \int_{T_0}^{T} \sum_{i=1}^{N} x_i c_{p,i}^0 \, dT, \tag{38}$$

where $c_{p,i}^0$ is the isobaric heat capacity of component i in its ideal gas state. The residual part of the enthalpy can be calculated with Equation (32). Here, the result is the same as for pure fluids (cf. Equation (33)). Only the temperature dependent parameter $a(T)$ has to be replaced by the temperature and composition dependent parameter a_m from Equation (25) and the parameter b has to be replaced by the composition dependent parameter b_m from

Equation (26)

$$h^{res}(T,v,x) = \frac{RTb_m(x)}{v-b_m(x)} + \frac{va_m(T,x)}{v^2+2b_m(x)v-b_m^2(x)} + \frac{1}{4}\frac{\sqrt{2}\cdot\left\{T\cdot\left[\frac{d}{dT}a_m(T,x)\right]-a_m(T,x)\right\}\cdot\ln\left(\frac{v+b_m(x)-\sqrt{2}\cdot b_m(x)}{v+b_m(x)+\sqrt{2}\cdot b_m(x)}\right)}{b_m(x)}, \quad (39)$$

with

$$\frac{\partial}{\partial T}a_m(T,x) = \sum_i^N \left(\sum_j^N \frac{1}{2}\frac{x_i x_j\cdot(1-k_{ij})\left\{\left(\frac{d}{dT}a_i(T)\right)\cdot a_j(T)+\left(\frac{d}{dT}a_j(T)\right)\cdot a_i(T)\right\}}{\sqrt{a_i(T)\cdot a_j(T)}} \right). \quad (40)$$

The enthalpy of vaporization $\Delta h_v(T)$ at a given temperature T and mole fraction x can be calculated with Equation (37) and the knowledge of the molar volumes of the saturated vapor phase v'' and the saturated liquid phase v' as

$$\Delta h_v(T,x) = h(T,x,v'') - h(T,x,v'). \quad (41)$$

The saturated volumes v' and v'' can be obtained iteratively from Equation (19). The procedure was described by Dohrn [29] in detail.

Table 2: Critical temperature T_c, critical pressure p_c, acentric factor ω and Mathias-Copeman Parameters c_1, c_2, c_3 for the investigated substances as taken from the literature.

component	T_c K	p_c MPa	ω	c_1	c_2	c_3	Ref.
nitrogen	126.2	3.394	0.040				[30]
oxygen	154.6	5.046	0.021				[30]
acetone	154.6	4.701	0.309				[30]
hydrazine	653.0	14.69	0.3280				[112]
monomethylhydrazine	567.0	8.04	0.3901				[112]
dimethylhydrazine[a]	523.0	5.00	0.2861				
ammonia	405.4	11.33	0.2560				[35]
water	647.3	22.05	0.3440				[30]
decafluorobutane	385.84	2.290	0.372	0.93487	-0.48485	2.09290	[31]
carbon dioxide	304.2	7.382	0.225				[32, 33]
2,2-dimethyl-1-propanol	552.7	4.078	0.595				[34]

[a] The values for T_c, p_c and ω were derived from the present dimethylhydrazine force field model.

Table 3: Binary parameters of the Peng-Robinson EOS for the quadratic (k_{ij}) and the Huron-Vidal (l_{ij}, l_{ji}) mixing rule (MR).

mixture	region	MR[a]	k_{ij}	l_{ij}	l_{ji}
nitrogen + acetone	223 - 400 K	quad.	0.2086		
nitrogen + acetone	400 - 480 K	quad.	$-0.0026 \cdot T/\mathrm{K} + 1.237$		
nitrogen + acetone	223 - 400 K	HV		241.91	926.52
nitrogen + acetone	400 - 480 K	HV		$-12.24 \cdot T/\mathrm{K} + 5136$	$25.47 \cdot T/\mathrm{K} - 9261$
oxygen + acetone		quad.	0.2908		
oxygen + acetone		HV		488.96	889.29
water + hydrazine		quad.	-0.1325		
monomethylhydrazine + water		quad.	-0.197		
dimethylhydrazine + water		quad.	-0.285		
dimethylhydrazine + hydrazine		quad.	-0.1		
ammonia + hydrazine		quad.	0.055		
ammonia + monomethylhydrazine		quad.	0		
ammonia + dimethylhydrazine		quad.	0.07		
carbon dioxide + 2,2-dimethyl-1-propanol		quad.		0.1	

[a] quad: Quadratic mixing rule (alpha function from acentric factor), HV: Huron-Vidal mixing rule (alpha function from acentric factor and UNIQUAC g^E model)

5 Extension of *ms*2 with the radial distribution function

*ms*2 is a software tool for the calculation of thermodynamic properties of bulk phases on basis of intramolecular interactions. Since the year 2001 it has been developed by various engineering scientists in permanent cooperation with research groups from computer science. The first release appeared in the year 2011 [6] and the development still continues in the form of numerous research projects. *ms*2 features the two main simulation techniques MD and MC and features different types of ensembles, namely NVE, NVT, NpT and μVT. Pure fluids can be considered as well as multi-component mixtures. The sampled thermodynamic properties vary from thermal properties, caloric properties, the Henry's law constant, the second virial coefficient to transport properties. In addition, properties of the VLE can be sampled with the Grand Equilibrium method [17]. For this purpose, *ms*2 provides the opportunity to calculate the chemical potential with Widom's test molecule method or the gradual insertion method. *ms*2 operates with rigid and permanently polar molecules. The dispersive and repulsive interactions can be considered by the LJ 12-6 potential, the electrostatic interactions by point charges, point dipoles or point quadrupoles.
In this work, *ms*2 was extended with the radial distribution function (RDF) as described in the following.

5.1 Radial distribution function in *ms*2

The RDF $g(r)$ is a measure for the structure of matter. It is defined by the local number density around a given position within a molecule $\rho^L(r)$ in relation to the overall number density $\rho = N/V$

$$g(r) = \frac{\rho^L(r)}{\rho} = \frac{1}{\rho}\frac{dN(r)}{dV} = \frac{1}{4\pi r^2 \rho}\frac{dN(r)}{dr}. \tag{42}$$

Therein, $dN(r)$ is the differential number of molecules or sites in a spherical shell volume element dV, which has the width dr and is located at the distance r from the regarded position

within a molecule.

In the second release of *ms*2, the RDF can be calculated during a MD or MC simulation run for pure components or mixtures. If this option is chosen, RDFs are calculated on the fly between all LJ sites, which are defined by the pure substance potential models (*.pm files in *ms*2). Thereby, it does not play a role, whether the LJ sites belong to the same molecular species or not. If a position within a molecule is to be considered, which is not defined by a LJ site of the potential model, but e.g. by a point charge that represents a hydrogen atom, a dummy LJ site has to be added to the potential model by the user. This dummy LJ site has to be defined with the parameters for its position, but with the LJ parameters $\sigma = \varepsilon = 0$ so that it does not alter the force field. Note that arbitrary positions within the molecule, which do not have to be occupied by other interaction sites, can be chosen in this way. The outcome of the RDF calculation is written (to a *.rdf file) with a frequency which can be defined (with the parameter "ErrorsFreq" in the simulation parameter *.par file). The parameter "RDFFreq" determines the frequency, with which the RDF is calculated. $g(r)$ is evaluated up to the cutoff radius r_c. The number of shells with the volume dV can be varied with the parameter "NumShell". The default value is 200.

Figure 4 shows six RDF of the mixture hydrogen chloride + phosgene + chlorobenzene + 2,4-diaminotoluene in a liquid state that was calculated simultaneously with *ms*2 on the fly.

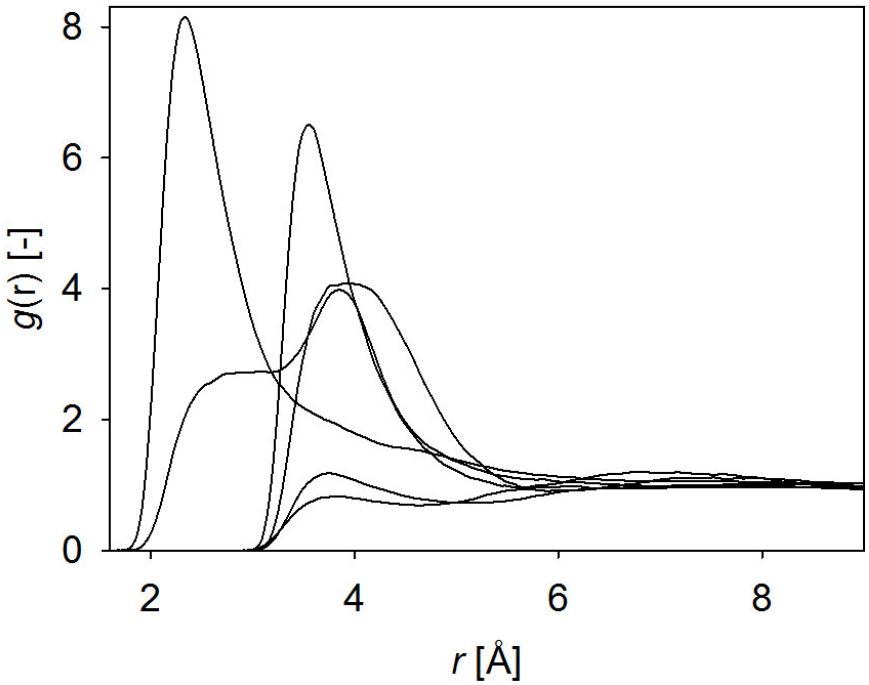

Figure 4: Radial distribution function $g(r)$ of the mixture hydrogen chloride + phosgene + chlorobenzene + 2,4-diaminotoluene in a liquid state calculated with the molecular simulation tool *ms*2 on the fly.

6 Systems containing acetone

Liquids, which are injected into a gaseous environment that has a supercritical state with respect to them, play an important role in energy conversion processes like Diesel and rocket engines or gas turbines. The challenge is to understand and model phenomena in trans-critical jets, where liquids change their state after injection to a supercritical fluid. The Collaborative Research Center Transregio 75 "Droplet Dynamics Under Extreme Ambient Conditions" (SFB-TRR75) [1, 2], which is funded by the Deutsche Forschungsgemeinschaft (DFG), investigates the injection of acetone droplets into a nitrogen/oxygen environment by experiment and computational fluid dynamics simulation [3, 4]. Knowledge on the phase behavior and other thermodynamic properties for these systems is crucial to undertake this task.

The aim of this work was to investigate the VLE behavior of the binary mixtures nitrogen + acetone and oxygen + acetone by experiment and molecular simulation in a large temperature, pressure and composition range. In order to obtain knowledge about the above discussed "extreme ambient conditions", the near critical region of the mixture nitrogen + acetone was of great interest. For further applications in the SFB-TRR75, the obtained data were aggregated with the Peng-Robinson EOS.

For the system nitrogen + acetone, the first step was to measure the saturated liquid line using a newly constructed apparatus at low temperatures at the eight isotherms 223, 243, 273, 303, 323, 343, 363 and 400 K up to a pressure of 12 MPa. The measurement results were compared with experimental data at 303 and 363 K by Jabloniec *et al.* [36], which are the only available data on fluid phase coexistence in the literature. On the basis of the present experimental data, the Henry's law constant for nitrogen in acetone was calculated at 223, 243, 273, 303, 323, 343, 363 and 400 K and compared to Henry's law constant data published by Just [37], Horiuti [38], Kretschmer *et al.* [39], Nitta *et al.* [40], Vosmansky and Dohnal [41], Tsuji *et al.* [42] and Jabloniec *et al.* [36]. Furthermore, the saturated vapor line was measured at the three isotherms 303, 223 and 343 K up to a pressure of 2.5 MPa. In order to aggregate the present experimental results, the Peng-Robinson EOS [5] was parameterized accordingly, considering two mixing rules that are based on one-fluid theory, i.e. the quadratic mixing rule [25] and the Huron-Vidal mixing rule [26].

To study the system nitrogen + acetone by molecular simulation, a force field model for

acetone (CH_3-(C=O)-CH_3), parameterized on the basis of QC calculations and experimental data for the saturated liquid density as well as the vapor pressure, was developed and compared with molecular models from the literature, i.e. the TraPPE model [43], a modified version thereof [44], the AUA4 model [45] and the OPLS model [46]. The present molecular acetone model was validated with the fundamental EOS by Lemmon and Span [14] and with experimental pure fluid data from the literature with respect to the Enthalpy of vaporization, various properties in the homogeneous fluid region (density, isobaric heat capacity, enthalpy, speed of sound), second virial coefficient, self-diffusion coefficient, shear viscosity and thermal conductivity. Combining this acetone model with molecular models for nitrogen from prior work [47], the unlike dispersive interaction between nitrogen and acetone was adjusted to one experimental Henry's law constant from the literature. Based on these mixture models, the VLE of nitrogen + acetone at low temperatures was determined by molecular simulation and assessed with the present experimental data and the adjusted Peng-Robinson EOS.
To investigate the saturated liquid line of nitrogen + acetone in the near critical region of the mixture, molecular simulations and experiments with a newly constructed apparatus were carried out at the tree isotherms 400, 450 and 480 K up to a maximum pressure of 41 MPa. In addition, the saturated vapor line was predicted by molecular simulation at these temperatures. Finally, for nitrogen + acetone the Peng-Robinson EOS was parameterized. The aim was to provide an EOS which yields reasonable results also near the critical line of the mixture for applications in the SFB-TRR75 as mentioned above. Parameters for the Huron-Vidal mixing rule [26] were determined.
For the system oxygen + acetone only a few measurements at low temperatures, pressures and therefore at low mole fractions of oxygen were carried out due to safety aspects. Thus, the saturated liquid line at the two isotherms 253 and 283 K up to a maximum pressure of 0.75 MPa were measured and then aggregated with the Peng-Robinson EOS using the quadratic and Huron-Vidal mixing rules. In addition, the Henry's law constant was calculated on the basis of the present experimental data and compared to Henry's law constant data published by Levi [48], Fischer and Pfleiderer [49], Finlayson [50], Horiuti [38], Kretschmer *et al.* [39], Schlaepfer *et al.* [51], Sinn *et al.* [52], Naumenko [53], Bub and Hillebrand [54], Tsuji *et al.* [42] and Luehring and Schumpe [55]. To investigate a more extensive temperature and pressure range by molecular simulation, the interaction parameter for oxygen and acetone was adjusted to the experimentally measured VLE data.

6.1 Apparatus and materials

The saturated liquid line of nitrogen + acetone was studied with the synthetic method. For the measurements at isotherms between 223 and 400 K the experimental setup described in Section 2.1 was used. The 400, 450 and 480 K isotherms were measured with the apparatus introduced in Section 2.2. The saturated vapor line of nitrogen + acetone was determined analytically with the experimental setup discussed in Section 2.3. For oxygen + acetone the saturated liquid line was measured with the apparatus from Section 2.1.
Nitrogen 5.0 (volume fraction 0.99999) and oxygen 4.8 (volume fraction 0.99998) were obtained from Air Liquide. Acetone with a purity > 99.9 % was purchased from Merck and degassed under vacuum.

6.2 Molecular models

6.2.1 Acetone

The present acetone model consists of four LJ sites, cf. Figure 5. Two of these sites were located at the oxygen (O) and carbon (C) atom positions, respectively. The others represent the two methyl (CH_3) groups. Therein, the hydrogen atoms were only implicitly considered, following the united atom approach. The dipole was placed in the geometric center of the molecule and the quadrupole was located between the two CH_3 groups. The geometric struc-

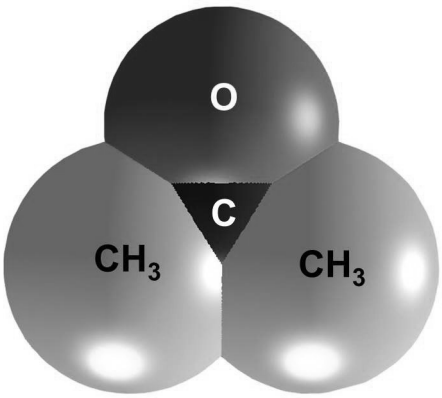

Figure 5: Present molecular force field model for acetone. C: carbon Lennard-Jones site, CH_3: methyl Lennard-Jones site, O: oxygen Lennard-Jones site. Note that the sphere diameters correspond to the Lennard-Jones size parameters, which are depicted according the molecular geometry scale.

ture of the molecule was determined by quantum chemical calculations using the software package GAMESS(US) [56] with the Hartree-Fock method and the 6-31G basis set. The magnitude and orientation of the dipole and quadrupole were subsequently specified according to the electron density distribution as obtained with the Møller-Plesset 2 method and the 6-311G(d,p) basis set. The positions of the atoms were taken from the preceding step for these calculations. The dipole and quadrupole magnitudes were estimated with the Mulliken approach [57]. The LJ parameters σ and ε were initially adopted from other similar models by Huang *et al.* [58]. The model was optimized to experimental VLE data (saturated liquid density and vapor pressure) of pure acetone by varying the LJ parameters. In the last step, all model parameters, including those for geometry and polarity, were fine-tuned with the reduced unit method [59]. The parameters of the molecular acetone model are listed in Table 4.

6.2.2 Nitrogen and oxygen

Molecular models for the pure fluids nitrogen and oxygen were needed for the studied binary mixtures nitrogen + acetone and oxygen + acetone. Models consisting of two LJ sites and one point quadrupole were developed for these components in prior work of our group [47] and were adopted here.

6.2.3 Mixtures of nitrogen + acetone and oxygen + acetone

For the system nitrogen + acetone, the Henry's law constant at 314.25 K as reported by Horiuti [38] and for oxygen + acetone the vapor pressure at 283.15 K and x_{O2} = 0.005 mol/mol, which was measured in present work, were used for the adjustment. The optimized values are ξ = 0.96 for nitrogen + acetone and ξ = 0.905 for oxygen + acetone.

Table 4: Parameters of the present molecular model for acetone. Lennard-Jones interaction sites are denoted by the modeled atoms or atomic groups. Electrostatic interaction sites are denoted by dipole or quadrupole, respectively. Coordinates are given with respect to the center of mass in a principal axes system. Orientations of the electrostatic sites are defined in standard Euler angles, where φ is the azimuthal angle with respect to the $x-z$ plane and θ is the inclination angle with respect to the z axis.

interaction site	x Å	y Å	z Å	σ Å	ε/k_B K	θ deg	φ deg	μ D	Q DÅ
C	0	0	0	2.9307	9.8216				
O	0	1.2095	0	3.3704	106.9873				
CH_3	0	-0.8031	1.2853	3.6225	111.9795				
CH_3	0	-0.8031	-1.2853	3.6225	111.9795				
dipole	0	0	0			90	90	3.4448	
quadrupole	0	-0.8031	0			90	90		0.7308

6.3 Simulation results for pure acetone

In the following Sections, the simulation results for the VLE behavior, different thermodynamic properties in the homogeneous region, the second virial coefficient and transport properties on the basis of the present acetone model are compared with available experimental data and with the EOS by Lemmon and Span [14], that is recommended by the National Institute for Standards and Technology (NIST), or with correlations from the DIPPR database [60]. In case of the VLE, the acetone model was also compared with the TraPPE model by Stubbs *et al.* [43] and the AUA4 model by Ferrando *et al.* [45]. All present data from experiment and simulation are available in numerical form in the appendix. Simulation details are given in the appendix as well.

6.3.1 Vapor-liquid equilibrium data

With respect to the VLE behavior and the properties in the homogeneous fluid region, the EOS by Lemmon and Span [14] was used as a reference. The stated uncertainties of the EOS are 0.1 % for the saturated liquid density between 280 and 310 K, 0.5 % for the density of the liquid phase below 380 K and 1 % elsewhere. The uncertainties for the vapor pressure are 0.5 % above 270 K and 0.25 % between 290 and 390 K. In addition, experimental data compiled in the Dortmunder Datenbank [30] and the DIPPR database [60] are shown as well. Figures 6 to 8 illustrate the saturated densities, the vapor pressure and the enthalpy of vaporization of acetone which were obtained with the present molecular model, the TraPPE model [43], its modification [44], the AUA4 model [45] and the OPLS model [46]. The relative deviations of all five models from the reference EOS [14] are plotted in Figure 9. As can be seen, the present molecular model yields the best agreement with the reference EOS for all shown properties. Only for the saturated liquid density at temperatures above about 400 K, the modified TraPPE model [44] exhibits smaller deviations.

The critical values for temperature, density and pressure were calculated on the basis of the present simulation data with a method suggested by Lotfi *et al.* [61]. The critical values for the present model T_c = 509 (508.1) K, ρ_c = 4.8 (4.7) mol/l and p_c = 4.7 (4.7) MPa agree well with the results of the reference EOS [14] (values in parentheses). It should be noted that the agreement is within the estimated uncertainties of the present simulation data, being 0.5 % for T_c, 2 % for ρ_c and 4 % for p_c. The critical properties from the reference EOS, the present molecular model and the four models from the literature are summarized in Table 5.

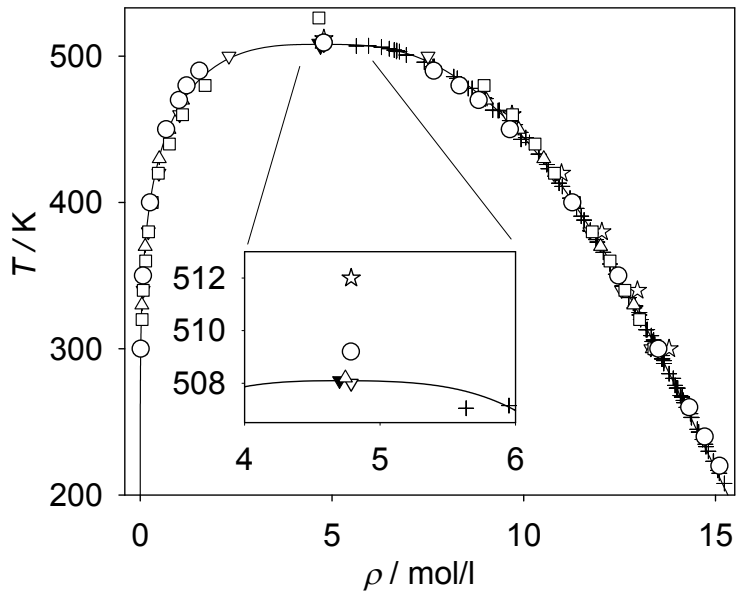

Figure 6: Saturated densities of acetone. Simulation data: (○) this work, (▽) TraPPE model [43], (△) modified TraPPE model [44], (⋆) AUA4 model [45], (□) OPLS model [46]; (+) experimental data [30, 60]; (—) EOS by Lemmon and Span [14]; (▼) critical point of the EOS [14].

Table 5: Critical data of pure acetone from the reference EOS, the present molecular model and the molecular models from the literature. The number in parentheses indicates the statistical uncertainty in the last digit.

	T_c K	ρ_c mol/l	p_c MPa
EOS by Lemmon and Span [14]	508	4.7	4.7
molecular model, this work	509 (3)	4.8 (1)	4.7 (2)
TraPPE model [43]	508	4.8	5.5
modified TraPPE model [44]	508.2 (2)	4.74 (2)	4.85 (3)
AUA4 model [45]	512	4.8	
OPLS model [46]	526	4.7	5.6

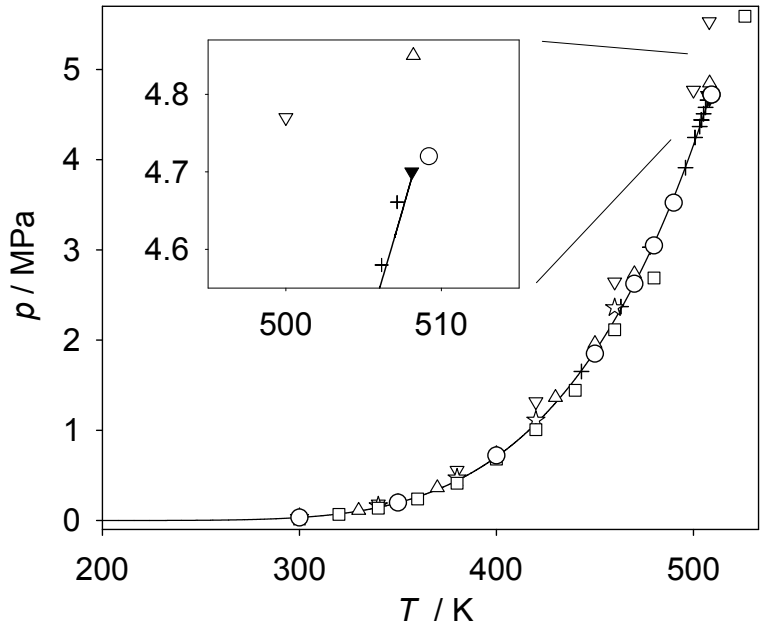

Figure 7: Vapor pressure of acetone. Simulation data: (○) this work, (▽) TraPPE model [43], (△) modified TraPPE model [44], (⋆) AUA4 model [45], (□) OPLS model [46]; (+) experimental data [30, 60]; (—) EOS by Lemmon and Span [14]; (▼) critical point of the EOS [14].

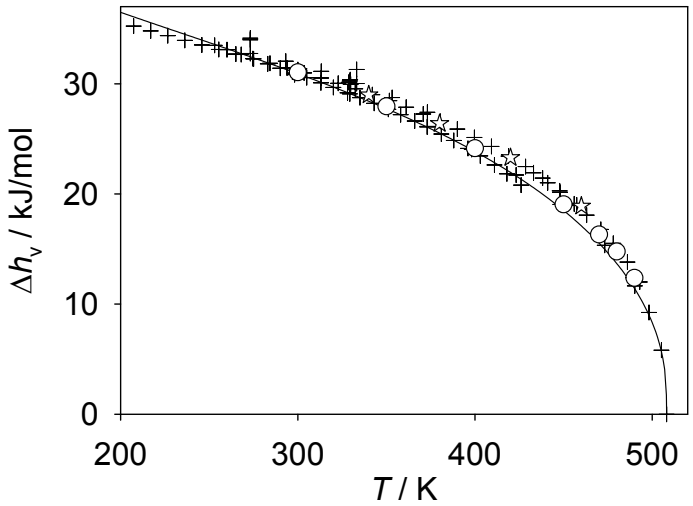

Figure 8: Enthalpy of vaporization of acetone. Simulation data: (○) this work, (⋆) AUA4 model [45]; (+) experimental data [30, 60]; (—) EOS by Lemmon and Span [14].

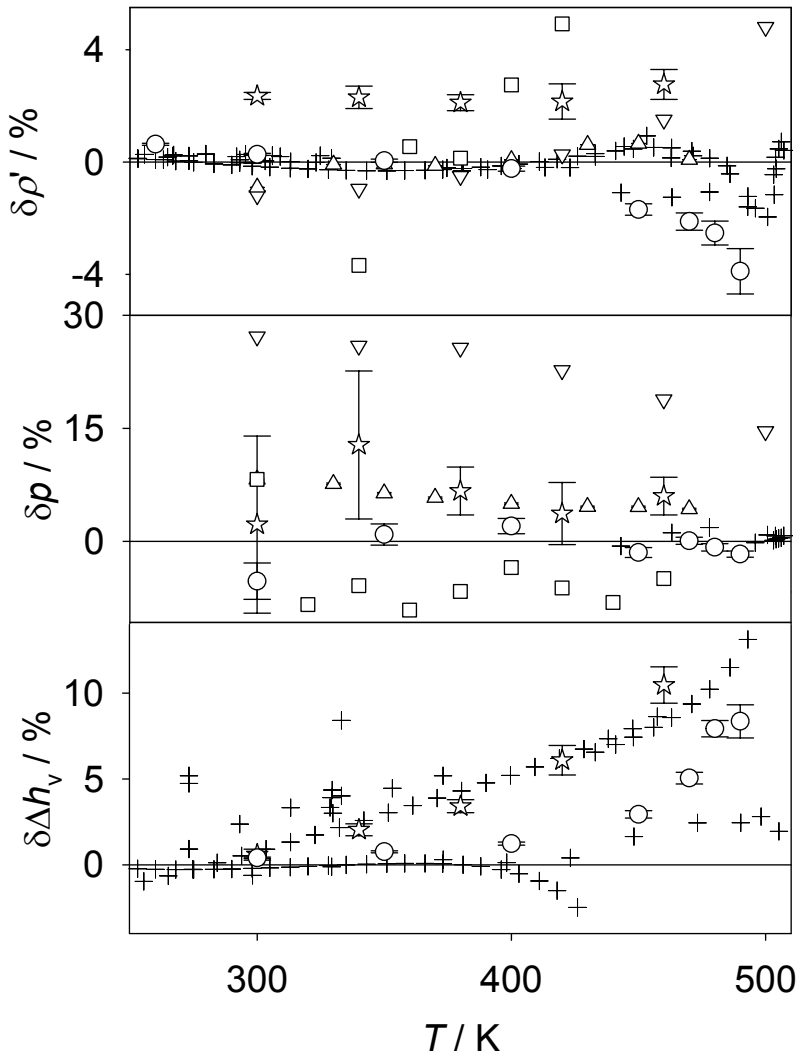

Figure 9: Relative deviations of vapor-liquid equilibrium properties of acetone from the EOS by Lemmon and Span [14] ($\delta z = (z_i - z_{eos})/z_{eos}$). Simulation data: (○) this work, (▽) TraPPE model [43], (△) modified TraPPE model [44], (⋆) AUA4 model [45], (□) OPLS model [46]; (+) experimental data [30, 60].

6.3.2 Homogeneous region

In the homogeneous region, simulations were carried out for density, isobaric heat capacity, speed of sound and residual enthalpy over a temperature range from 200 to 550 K and a pressure range from 5 to 95 MPa. The uncertainties of the reference EOS [14] for the isobaric heat capacity and the speed of sound are 1 %. However, the uncertainties of this EOS for these properties may be higher at pressures above the saturation pressure and at temperatures above 320 K in the liquid phase and under supercritical conditions [14].

The isobaric heat capacity c_p was calculated here as a sum of the residual and the ideal gas contribution

$$c_p = c_p^{res} + c_p^{id}, \tag{43}$$

wherein the residual contribution c_p^{res} was obtained from molecular simulation and the ideal gas contribution was taken from the reference EOS [14]. For the enthalpy, only the residual contribution $h^{res} = h - h^{id}$ was used for comparison.
The speed of sound c can be calculated as

$$c = \frac{1}{\sqrt{M\beta\rho - T\alpha^2/c_p^{id}}}, \tag{44}$$

wherein M is the molar mass, β the isothermal compressibility, ρ the density and α the volume expansivity. Except for c_p^{id}, all data on the right hand side of Equation (44) were sampled directly by molecular simulation. The relative deviations of the simulation data from the reference EOS [14] are mainly below 1 % for the density as well as for the isobaric heat capacity and below 2 % for the speed of sound as well as for the residual enthalpy over the entire temperature and pressure range. Only near the critical point, the deviations may be significantly larger, cf. Figure 10.

6.3.3 Second virial coefficient

The second virial coefficient was predicted over a temperature range from 240 to 2500 K by evaluating Mayer's f-function. This approach was described e.g. by Eckl *et al.* [62]. Figure 11 shows the results in comparison to experimental data and a correlation from the DIPPR database [60]. Over the whole temperature range, the present data are in excellent agreement with the experimental data. The average absolute deviation to the correlation in a temperature range from 400 to 2500 K is only 6.4 ml/mol.

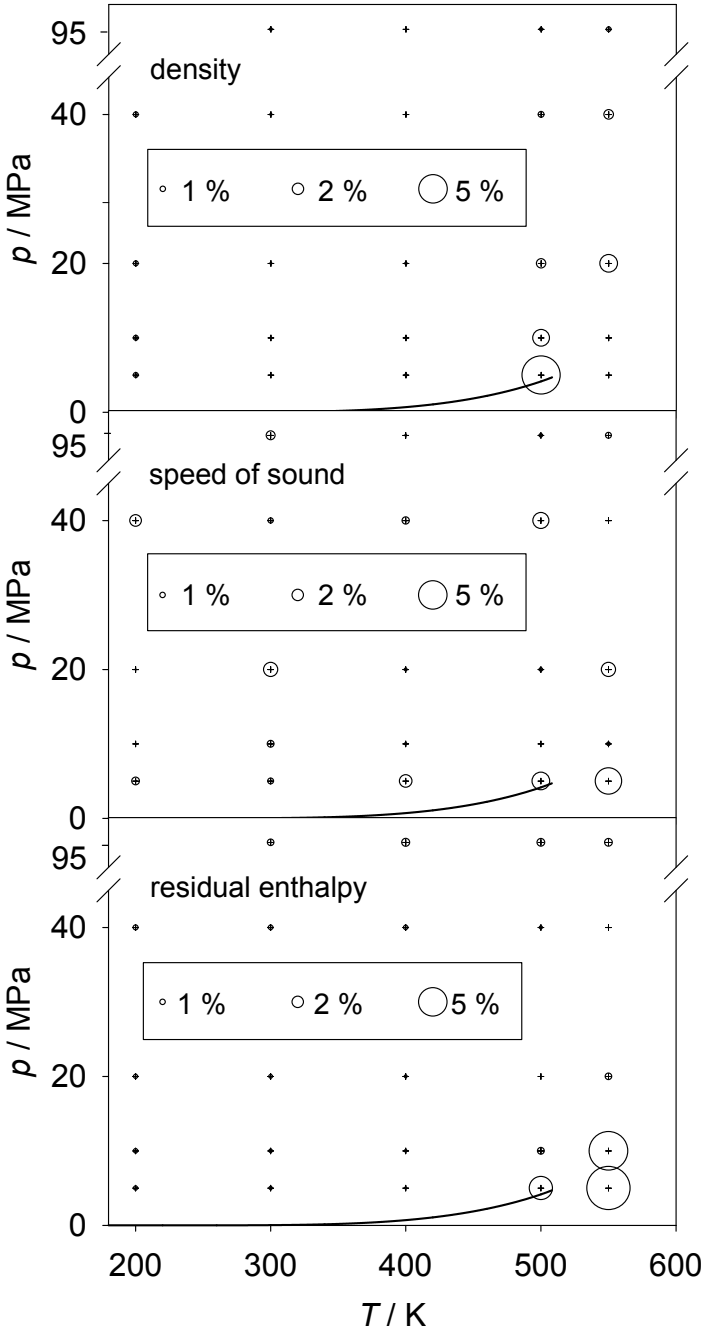

Figure 10: Density, speed of sound and residual enthalpy of acetone in the homogeneous region. Relative deviations between present simulation data and the EOS by Lemmon and Span [14] ($\delta z = (z_{\mathrm{sim}} - z_{\mathrm{eos}})/z_{\mathrm{eos}}$). The size of the bubbles indicates the magnitude of the relative deviation, the solid line is the vapor pressure curve [14].

6.3.4 Transport properties

Transport properties of liquid acetone were obtained by EMD simulations following the Green-Kubo formalism, cf. Guevara-Carrion *et al.* [63]. Figures 12 to 14 illustrate the simulation results for self-diffusion coefficient, shear viscosity and thermal conductivity along the saturated liquid line from 190 to 325 K in comparison with experimental data and correlations. In case of the self-diffusion coefficient, the correlation was published by Ertl and Dullien [64]. Correlations from the DIPPR database [60] were used for the shear viscosity and the thermal conductivity. For all considered transport properties, the simulation data agree very well with the experiment and the correlations over the entire temperature range. The mean deviation between the simulation points and the correlations is 8 %, 7 % and 9 % for self-diffusion coefficient, shear viscosity and thermal conductivity, respectively. It should be noted that transport properties were not considered in the parameterization of the molecular model.

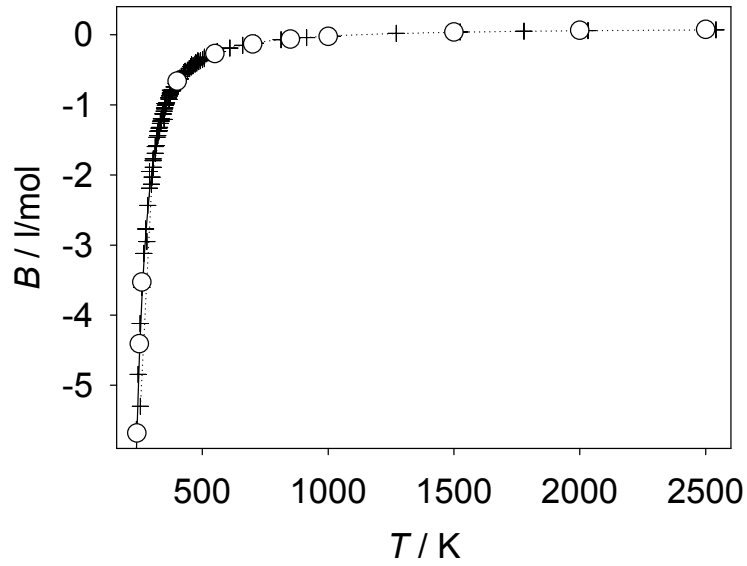

Figure 11: Second virial coefficient of acetone: (○) simulation data, this work; (+) experimental data [30, 60]; (·····) correlation of experimental data from the DIPPR database [60]; (—) EOS by Lemmon and Span [14].

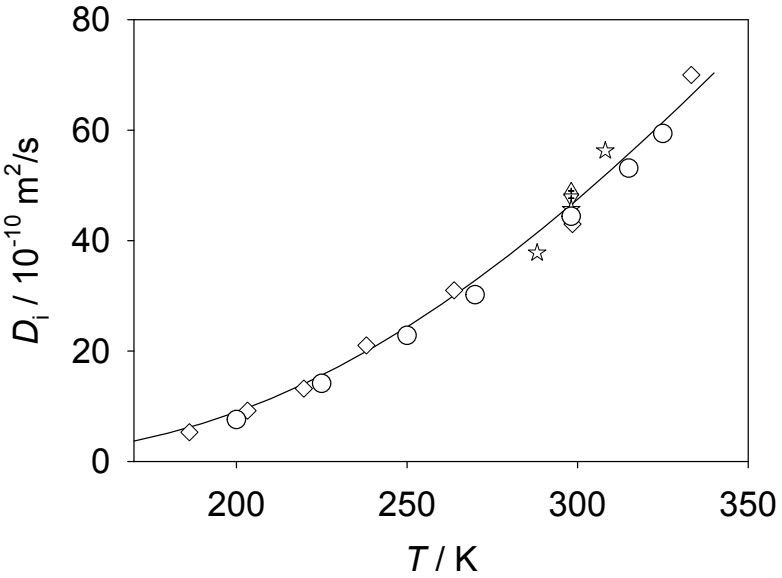

Figure 12: Self-diffusion coefficient of acetone along the saturated liquid line: (○) simulation data, this work; experimental data: (▽) McCall *et al.* [65], (◊) Krüger and Weiss [66], (⋆) Holz *et al.* [67], (△) Wheeler and Rowley [68]; (—) correlation of experimental data by Ertl and Dullien [64].

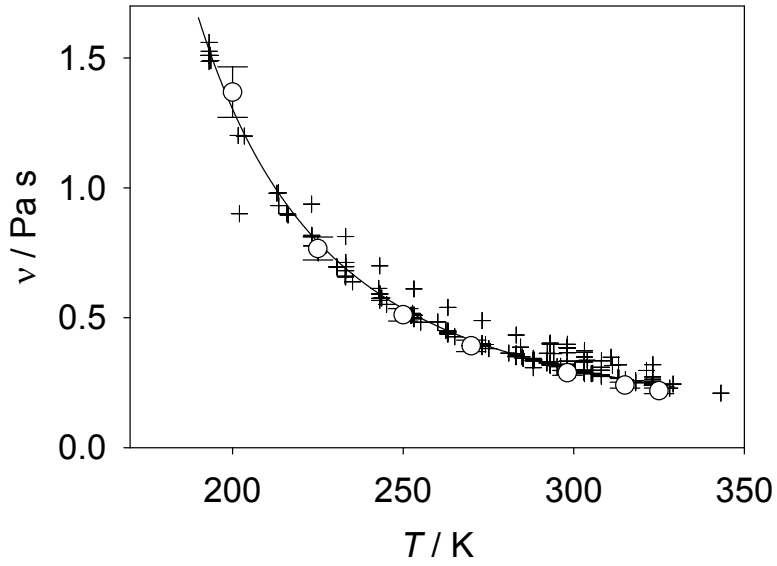

Figure 13: Shear viscosity of acetone along the saturated liquid line: (○) simulation data, this work; (+) experimental data [30, 60, 69]; (—) correlation of experimental data from the DIPPR database [60].

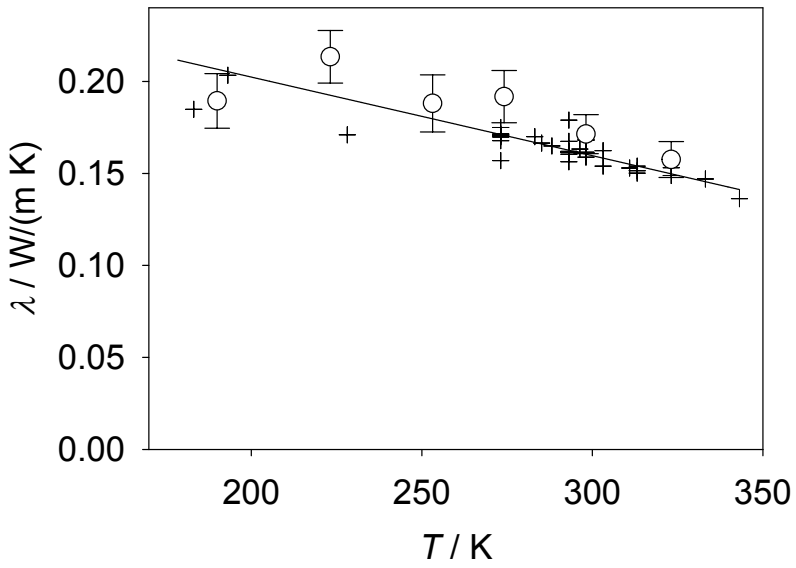

Figure 14: Thermal conductivity of acetone along the saturated liquid line: (○) simulation data, this work; (+) experimental data [30, 60]; (—) correlation of experimental data from the DIPPR database [60].

6.4 Results for nitrogen + acetone

6.4.1 Low temperatures

Experiment and Peng-Robinson EOS

The VLE of the system nitrogen + acetone was measured at temperatures from 223 to 400 K and pressures of up to 12 MPa with respect to the saturated liquid line, cf. Figure 15. The numerical values are listed in Table A.2 in the appendix. The saturated vapor line was measured at temperatures from 303 to 343 K and pressures of up to 1.8 MPa, cf. Figure 16. Experimental VLE data at finite mole fractions and also Henry's law constant data can be found in the literature for this mixture. The present results are discussed first on the basis of isothermal pressure-composition phase diagrams. To correlate the present data, the Peng-Robinson EOS [5] with the quadratic mixing rule [25] and the Huron-Vidal mixing rule [26] was used, cf. Section 4. The Peng-Robinson EOS was fitted to the entire present experimental data set for the saturated liquid line simultaneously. Table 2 summarizes the employed pure component parameters for nitrogen and oxygen. The resulting binary mixing parameters are $k_{ij} = 0.209$ for the quadratic mixing rule and for the Huron-Vidal mixing rule $l_{ij} = 241.9$ and $k_{ji} = 926.5$, cf. Table 3. However, for better visibility, only the results of the Huron-Vidal mixing rule are shown graphically.

The VLE at 303 and 363 K at pressures of up to 3 MPa are presented in Figure 17, where the experimental data of Jabloniec *et al.* [36] are shown for comparison. The mean deviation of the saturation pressure measured in this work with respect to the Peng-Robinson EOS is less than 2 % for both isotherms. The data points measured by Jabloniec et al. [36] are in line with the Peng-Robinson EOS at 363 K. However, at 303 K they exhibit a significantly steeper slope. The mean deviation of the pressure reported by Jabloniec *et al.* [36] with respect to the Peng-Robinson EOS is around 1.5 % at 363 K and 14 % at 303 K.

A larger temperature and pressure range of the saturated liquid line is presented in Figure 15. An almost linear relation between the mole fraction of the solute and the vapor pressure can be identified. Lower temperatures exhibit a slightly convex shape of the saturated liquid line. With rising temperature, the solubility of nitrogen in acetone is increased. It is also noticeable that the Peng-Robinson EOS agrees very well with the present data for all regarded temperatures.

The present results can also be assessed on the basis of the Henry's law constant, cf. Figure 18. To calculate the Henry's law constant on basis of the present experimental data, an

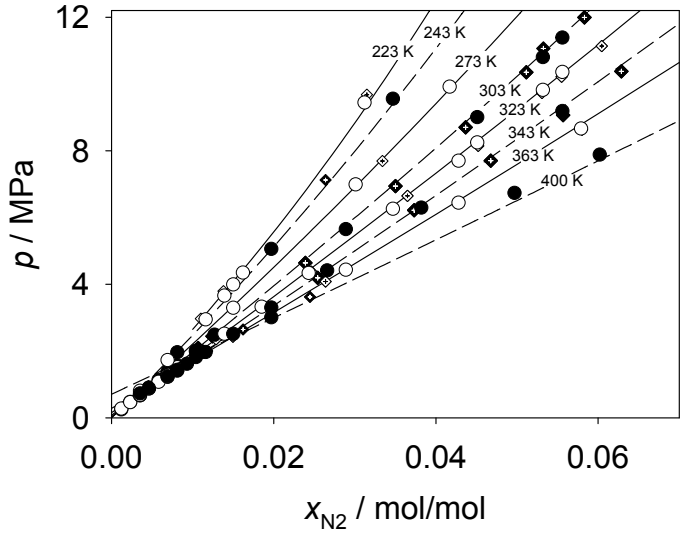

Figure 15: Saturated liquid line of nitrogen + acetone: (○), (●) simulation data, this work; (◊), (♦) experimental data, this work; (—), (- - -) Peng-Robinson EOS (Huron-Vidal mixing rule). The dashed lines represent the same isotherms as the solid symbols.

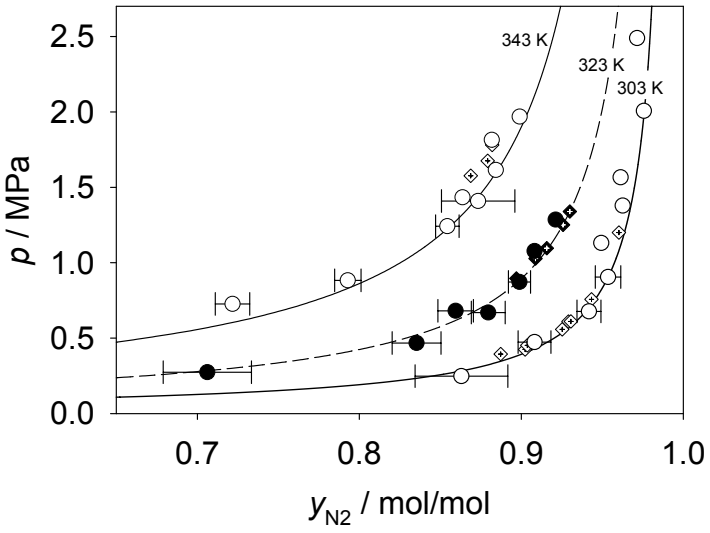

Figure 16: Saturated vapor line of nitrogen + acetone: (○), (●) simulation data, this work; (◊), (♦) experimental data, this work; (—), (- - -) Peng-Robinson EOS (Huron-Vidal mixing rule). The dashed line represents the same isotherm as the solid symbols.

extrapolation procedure at constant temperature as described by Merker *et al.* [70] was used

$$H_i = \lim_{p \to p^s_{Ac}} \frac{f_i}{x_i}, \tag{45}$$

where

$$f_i = p \cdot y_i \cdot \varphi_i. \tag{46}$$

f_i and φ_i are the fugacity and the fugacity coefficient of the solute in the mixture, respectively. x_i and y_i are the mole fractions of the solute in the liquid and the vapor phase, respectively. The calculated Henry's law constant is listed in Table A.1 in the appendix. Henry's law constant data for the mixture nitrogen + acetone were found in several literature sources, cf. Figure 18. The mean deviation of the present Henry's law constant and the data from the literature with respect to the straight line shown in Figure 18 is 2 % and 0.8 %, respectively, which is well within the uncertainty of the present experiments. Only the measurements of Just [37], which were published 110 years ago, and of Jabloniec *et al.* [36] at 303 K differ from the remaining ones. For this temperature, Jabloniec et al. [36] reported a Henry's law constant which is 18 % above the straight line. At 363 K, the data of Jabloniec et al. [36] agree much better with the remaining data. Note that this was also observed for the VLE data at finite mole fractions by Jabloniec *et al.* [36].

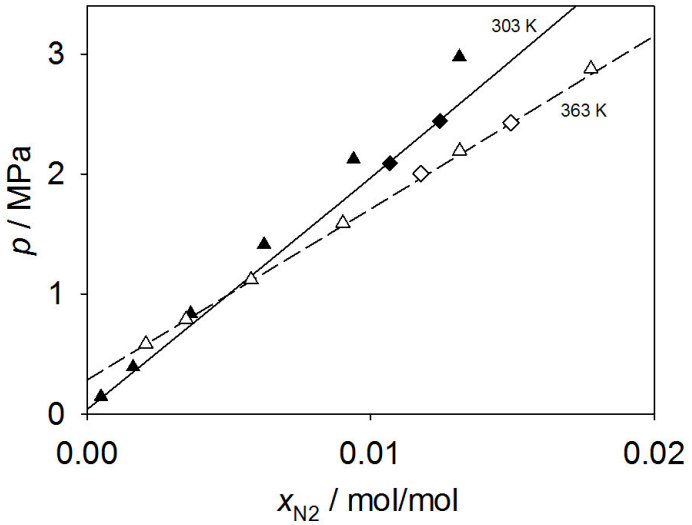

Figure 17: Saturated liquid line of nitrogen + acetone: (♦), (◊) experimental data, this work; (▲), (△) experimental data, Jabloniec *et al.* [36]; (—), (- - -) Peng-Robinson EOS (Huron-Vidal mixing rule).

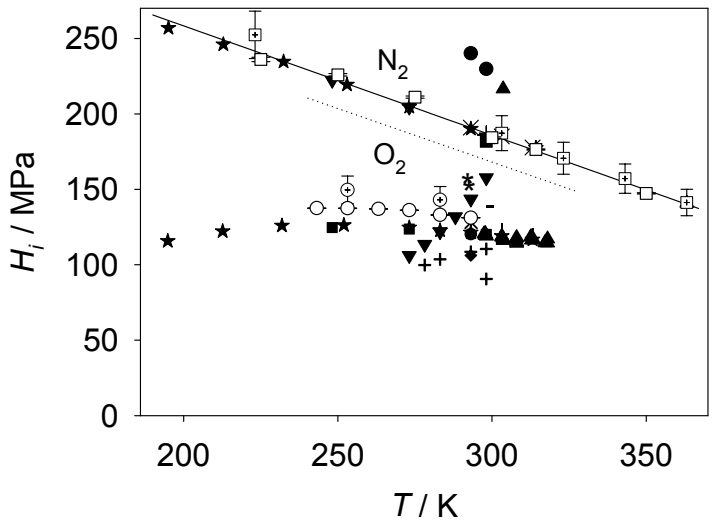

Figure 18: Henry's law constant. Nitrogen in acetone: (□) simulation data, this work; experimental data: (⊞) This work, (▲) Jabloniec *et al.* [36], (●) Just [37], (★) Horiuti [38], (▼) Kretschmer *et al.* [39], (■) Nitta *et al.* [40], (+) Vosmansky and Dohnal [41], (×) Tsuji *et al.* [42]; Oxygen in acetone: (○) simulation data, this work; experimental data: (⊕) This work, (+) Levi [48], (∗) Fischer and Pfleiderer [49], (▼) Finlayson [50], (★) Horiuti [38], (■) Kretschmer *et al.* [39], (●) Schlaepfer *et al.* [51], (⧫) Sinn *et al.* [52], (-) Naumenko [53], (▲) Bub and Hillebrand [54], (|) Tsuji *et al.* [42], (×) Luehring and Schumpe [55]; (—) straight line. All symbols above the dotted line represent nitrogen data, the others represent oxygen data.

The experimental data for the saturated vapor line are presented in Figure 16. These results can only be compared to the Peng-Robinson EOS, because no other experimental data are available in this temperature range. It is noticeable that the agreement between the Peng-Robinson EOS with the Huron-Vidal mixing rule and the present experimental data with a mean deviation of only 0.01 MPa is best at 323 K. At 303 K (mean deviation of 0.16 MPa) and especially at 343 K (mean deviation of 0.20 MPa), the present measurements exhibit a higher vapor pressure than the Peng-Robinson EOS. Nevertheless, the curvature of the saturated vapor line is in good agreement.

Simulation

The simulation results for the saturated liquid line and the saturated vapor line of nitrogen + acetone are shown in Figures 15 and 16 as well. For the saturated liquid line, eight isotherms

between 223.15 and 400 K up to a pressure of 11 MPa were simulated. For the saturated vapor line, simulations were carried out for the three isotherms 303.15, 323.15 and 343.15 K up to a pressure of 2 MPa. For both the saturated liquid line and the saturated vapor line, the simulation results agree well with the present experimental data and the Peng-Robinson EOS. The mean deviation between all simulation points and the Peng-Robinson EOS with respect to the vapor pressure is less than 2 % for the saturated liquid line and less than 0.15 MPa for the saturated vapor line. In terms of the nitrogen mole fraction, nearly all simulation points agree with the Peng-Robinson EOS within their statistical uncertainties.
For the Henry's law constant of nitrogen + acetone, simulations were carried out between 225 and 470 K, cf. Figure 18. Simulation details are given in the appendix. As described in Section 6.2.3, the molecular mixture model was adjusted to the Henry's law constant H = 176.4 MPa [38] at 314.25 K. The Henry's law constant data from present experimental work and other literature data [36–42] as well as the present simulations are in good line with the experimental data. The mean deviation between the simulation points and the straight line in Figure 18 is only 1.3 %.

6.4.2 Transcritical region

Experiment and simulation

Due to the lack of experimental data at high pressures in the literature, measurements with the apparatus introduced in Section 2.2 and simulations with the molecular model discussed in Section 6.2 were carried out for nitrogen + acetone for the three isotherms 400, 450 and 480 K (± 5 K for the experimental measurements). These data points are shown in Figures 19 to 21. It can be seen that the simulation data and the data from experiment agree well in the region of small mole fractions x_{N2} for all three isotherms. However, with rising x_{N2}, particularly in the near critical region, the molecular model overestimates the vapor pressure of the mixture.

Peng-Robinson EOS

The present experimental and simulation results for nitrogen + acetone show that both parameterizations (quadratic and Huron-Vidal mixing rule) of the Peng-Robinson EOS yield poor results for the 400, 450 and 480 K isotherms. To achieve better results in the near-critical region, the Peng-Robinson EOS was readjusted to the present data at 480 K, considering the parameterization from Section 6.4.1.
The binary parameters of the Huron-Vidal mixing rule were assumed to be temperature de-

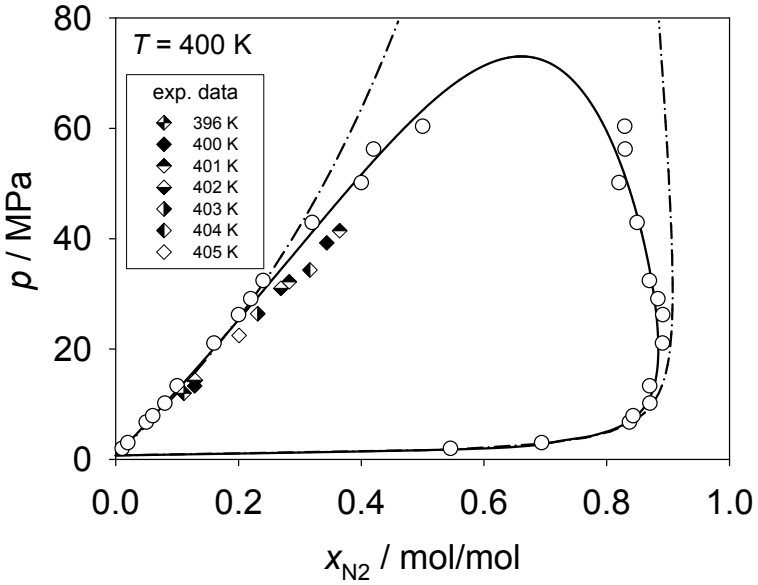

Figure 19: Vapor-liquid equilibrium of nitrogen + acetone around 400 K: (◊) experimental data, this work; (○) simulation data, this work; Peng-Robinson EOS: (—) Huron-Vidal (l_{ij}=241.9, l_{ji}=926.5), ($- \cdot -$) quadratic (k_{ij}=0.1970).

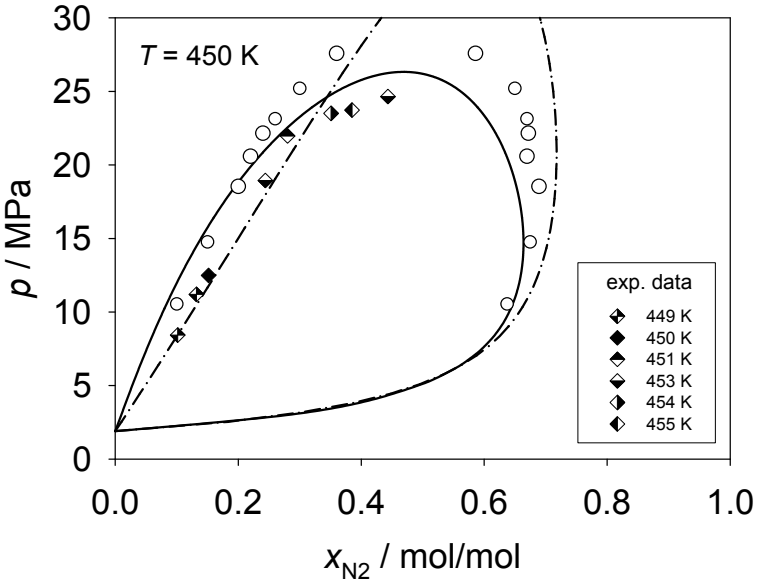

Figure 20: Vapor-liquid equilibrium of nitrogen + acetone around 450 K: (◊) experimental data, this work; (○) simulation data, this work; Peng-Robinson EOS: (—) Huron-Vidal (l_{ij}=-369.9, l_{ji}=2200), ($- \cdot -$) quadratic (k_{ij}=0.0670).

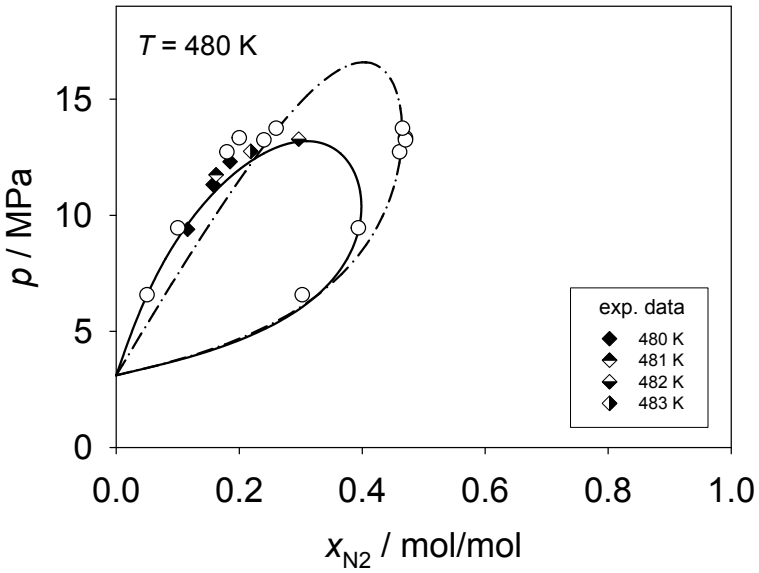

Figure 21: Vapor-liquid equilibrium of nitrogen + acetone around 480 K: (◊) experimental data, this work; (○) simulation data, this work; Peng-Robinson EOS: (—) Huron-Vidal (l_{ij}=-337.0, l_{ji}=2964), ($-\cdot-$) quadratic (k_{ij}=0.0110).

pendent with

$$l_{ij} = \begin{cases} 241.9 & \text{for } 223 \leq T \text{ / K} \leq 400 \\ -12.24 \cdot T/\text{K} + 5136 & \text{for } 400 < T \text{ / K} \leq 480, \end{cases} \tag{47}$$

and

$$l_{ji} = \begin{cases} 926.5 & \text{for } 223 \leq T \text{ / K} \leq 400 \\ 25.47 \cdot T/\text{K} - 9261 & \text{for } 400 < T \text{ / K} \leq 480. \end{cases} \tag{48}$$

Note that the binary parameters are continuous at 400 K.

The Peng-Robinson EOS using the Huron-Vidal mixing rule is shown in Figures 19 to 21 for the isotherms 400, 450 and 480 K. It can be seen that there is a reasonable agreement with experiment and simulation in the extended critical region.

The new parameterization of the Peng-Robinson EOS using the quadratic mixing rule shows that this mixing rule does not yield reasonable results in a wide temperature and composition range, cf. Figures 14 to 16. The correlation of the present data between 400 and 480 K leads to a temperature-dependent binary parameter of the quadratic mixing rule of $k_{ij} = -0.0026 \cdot T/\text{K} + 1.237$.

6.5 Results for oxygen + acetone

Experiment and Peng-Robinson EOS

The measurement of the system oxygen + acetone required various safety precautions. Especially the handling of pure oxygen upon filling of the cell and adding acetone was critical. In atmospheres of pure oxygen, some substances (e.g. lubricants) tend to self-ignite, therefore all tubes and valves were repeatedly cleaned. Protruding burrs at the tubes were removed to avoid pressure surges. For the lubrication of the valves, a dedicated material was selected, which is certified for the use with pure oxygen. To avoid the arcing of an electrostatic charge, every component of the apparatus was grounded. In order to reduce the impact of an explosion, which would lead to a steep pressure rise, only small pressures of up to 0.8 MPa were realized during the measurement. Furthermore, only low temperatures from 253 to 283 K were studied.

The experimental results for the saturated liquid line at 253 and 283 K are presented in an isothermal pressure-composition phase diagram, cf. Figure 22 and Table 18. To correlate the present data, the Peng-Robinson equation of state was used, cf. Section 4, and fitted to the entire present experimental data set for the saturated liquid line simultaneously. Table 2 summarizes the employed pure component parameters for oxygen and acetone. The resulting binary mixing parameters are $k_{ij} = 0.291$ for the quadratic mixing rule and for the Huron-Vidal mixing rule $l_{ij} = 489.0$ and $l_{ji} = 889.3$, cf. Table 3. It is hard to distinguish the differences between the present temperatures because only a small pressure range was examined. At 253 K, the experimental data agree well with the Peng-Robinson EOS using the Huron-Vidal mixing rule, especially for lower pressures. At 283 K, the Peng-Robinson EOS shows a slightly steeper slope than the experimental data.

The Henry's law constant of oxygen in acetone from the literature exhibit a large scatter compared with the predominantly consistent data published for nitrogen. For example at 298.15 K, the deviation between the lowest and the highest reported value is 67 MPa. The Henry's law constant of oxygen calculated on basis of the present experimental data at 253 and 283 K with Equation (45) is located in the upper part of the range of previously reported values, cf. Figure 18.

Simulation

In Figure 22, the present simulation results for the saturated liquid line of oxygen + acetone at 253.15 and 283.15 K are compared with experimental data and the Peng-Robinson EOS. Note that the plotted region for pressure and mole fraction is quite small, the maximum pres-

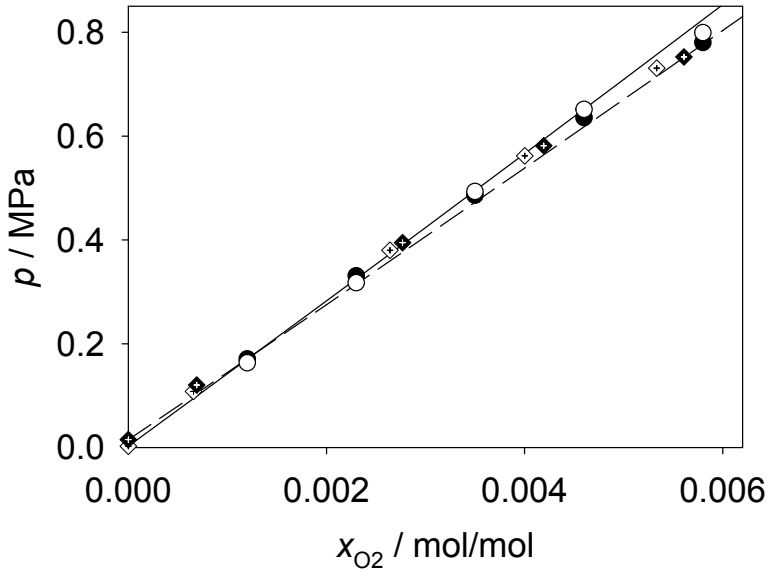

Figure 22: Saturated liquid line of oxygen + acetone: simulation data, this work: (○) 253.15 K, (●) 283.15 K; experimental data, this work: (◊) 253.15 K, (♦) 283.15 K; (—), (- - -) Peng-Robinson EOS with quadratic mixing rule, this work. The dashed line represents the same isotherm as the solid symbols.

sure is 0.8 MPa and the maximum oxygen mole fraction is only about 0.006 mol/mol. It can be seen that the points which belong to the 253.15 K isotherm do not differ much from the points that belong to the 283.15 K isotherm. Obviously, this is due to the intersection of both saturated liquid lines at a mole fraction $\approx$ 0.0015 mol/mol. Figure 22 shows a good agreement between simulation, experiment and the Peng-Robinson EOS. The mean deviation of the simulated vapor pressure and that obtained from the Peng-Robinson EOS is 2.2 %.
Simulations for the Henry's law constant of oxygen in acetone were carried out in a temperature range between 243.15 and 293.15 K, cf. Figure 18. The predicted values agree with the experimental Henry's law constant almost within their statistical simulation uncertainties. Overall, the simulation points lie approximately in the center of the experimental data from the literature and follow the temperature dependence e.g. by Horiuti [38] or by Kretschmer *et al.* [39].

6.6 Conclusion

New experimental data on fluid phase coexistence of the binary mixtures nitrogen + acetone and oxygen + acetone at low temperatures were reported. On the basis of this information,

Henry's law constant data were calculated for both systems. For the system nitrogen + acetone, the present experimental data show a good agreement with most data from the literature. It should be noted that the Henry's law constant at 303 K, as reported recently by Jabloniec *et al.* [36], is significantly higher than the remaining data. The same deviation can be seen in the course of the saturated liquid line by Jabloniec *et al.* [36] at 303 K.
For the system oxygen + acetone, the Henry's law constant was determined with the same method and a similar accuracy as for the system nitrogen + acetone. The present data are in the range of previously reported experimental results. Moreover, the Peng-Robinson EOS with the quadratic mixing rule and the Huron-Vidal mixing rule was adjusted to the new experimental data points of the saturated liquid line for both binary systems.
Furthermore, VLE of the systems nitrogen + acetone and oxygen + acetone were studied by molecular simulation. A new force field model for acetone was developed and validated with the EOS by Lemmon and Span [14] as well as with various experimental data from the literature. It was shown that there is a good agreement between simulation, the EOS and the experimental literature data throughout. For a large part of the homogeneous fluid state, the deviations are mainly below 1 % for the density and isobaric heat capacity and below 2 % for the speed of sound and the residual enthalpy. The average difference between simulation and EOS for the second virial coefficient was found to be only 6.4 ml/mol over a wide temperature range. For the self-diffusion coefficient, the shear viscosity and the thermal conductivity in a range of liquid states, the mean deviation between simulation and correlations of experimental data was smaller than 9 %. In addition, the present model was compared to four molecular models from the literature in terms of saturated liquid density, vapor pressure and Enthalpy of vaporization. Almost throughout, the present model yields the smallest deviations with respect to the reference EOS.
For nitrogen + acetone and oxygen + acetone, the binary parameter ξ for the unlike dispersive interaction was adjusted to one experimental data point of each mixture. These mixture models for both systems were validated with the present experimental data at low temperatures. Subsequently, simulations were carried out to predict the VLE of these two systems. For nitrogen + acetone at 400, 450 and 480 K up to a pressure of 41 MPa, the simulation results were validated with data points for the saturated liquid line measured in this work by means of a newly constructed experimental setup. It was shown that the agreement between simulation and experiment is good for oxygen + acetone and for nitrogen + acetone for temperatures below 400 K. Above 400 K and at high pressures, the simulation points were above the experimentally measured points. Based on the obtained data for nitrogen + acetone, the Peng-Robinson EOS using the Huron-Vidal mixing rule was parameterized.

7 Hexamethyldisiloxane and octamethylcyclotetrasiloxane

Processes for the efficient use of heat at a low temperature level (e.g. industrial waste heat, geothermal heat or solar heat) were increasingly investigated in the last years due to the problems caused by the austerity of fossil energy sources and the rising amount of carbon dioxide in the atmosphere. Typical processes for heat recovery are Organic Rankine cycles (ORC), Kalina cycles or heat pumps. ORC are heat engines on basis of the Rankine process which use organic working fluids instead of water. Here, the siloxanes, in particular hexamethyldisiloxane (MM) and octamethylcyclotetrasiloxane (D4), are an important group of working fluids.

To develop ORC processes it is essential to have extensive knowledge about the thermodynamic properties of the working fluid, for example in the form of an EOS. EOS on basis of the free Helmholtz energy are available for MM and D4 [71]. However, it is supposed that their accuracy is not adequate over a wide temperature and pressure range due to the lack of experimental data. Within the scope of the project "Equation of state based on hybrid data sets – a combined approach for the development of fundamental equations of state and of accurate molecular models", which was funded by the Deutsche Forschungsgemeinschaft (DFG), new improved fundamental EOS for MM and D4 on basis of the existing experimental data and additional data from molecular modelling and simulation are developed. To this aim, simulation data on several derivatives of the Helmholtz energy f over a wide temperature and pressure range were generated directly with molecular simulation [72–74].

As test cases for the development of the discussed hybrid equation of states, two rigid and electroneutral force field models for MM and D4 were developed in the present work. Both models were validated by means of experimental data from the literature and correlations of these experimental data. Hereby, the saturated liquid density, vapor pressure, Enthalpy of vaporization, homogeneous liquid properties (density and speed of sound), second virial coefficient and transport properties (thermal conductivity and shear viscosity) were considered.

7.1 Molecular models

7.1.1 Molecular model for hexamethyldisiloxane

The geometric structure of the present molecular model for MM (cf. Figure 23) was determined by QC calculations using the software package GAMMES(US) [56] with the Hartree-Fock method and the 6-31G basis set. Nine LJ sites and three point charges were used to describe the intermolecular interactions between the molecules.

The LJ sites were placed on the two silica (Si) atoms, on the oxygen (O) atom and on each carbon (C) atom of the six methyl (CH_3) groups. All LJ parameters for the CH_3 site and for the O site were initially adopted from preceding works by Schnabel *et al.* [75] and Vrabec *et al.* [47], respectively. The LJ energy and size parameter for the Si site were adjusted to experimental saturated liquid density and vapor pressure.

Two negative point charges were located at the Si atoms and one positive point charge at the O atom. In total, the molecule is electroneutral. The point charge magnitudes were specified such that the obtained dipole magnitude $2.67 \cdot 10^{-30}$ Cm is the same as the dipole magnitude stated in the DIPPR database [60].

In the last step of the modeling procedure, all model parameters, including those for geometry and polarity, were fine-tuned with the reduced unit method [59]. The resulting model parameters are listed in Table 6.

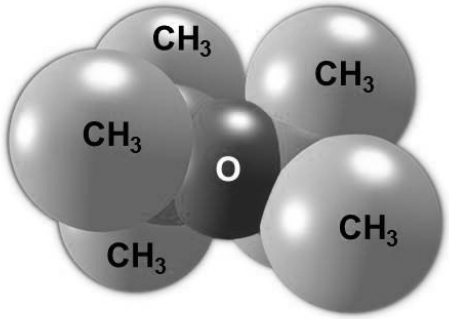

Figure 23: Present molecular force field model for hexamethyldisiloxane. CH_3: methyl Lennard-Jones site, O: oxygen Lennard-Jones site, not labeled: silica Lennard-Jones site. Note that the sphere diameters correspond to the Lennard-Jones size parameters, which are depicted according the molecular geometry scale.

7.1.2 Molecular model for octamethylcyclotetrasiloxane

For the present D4 model (cf. Figure 24), the geometric structure was also obtained by QC calculations using the software package GAMMES(US) [56] with the Hartree-Fock method and the 6-31G basis set.
The model consists of 16 LJ sites which were placed on the Si atoms, the O atoms and the C atoms of the CH_3 groups. All LJ parameters were taken from the initial MM model (before performing the reduced unit method), cf. Section 7.1.1.
Eight point charges with the same absolute magnitude were placed on each of the Si and O atoms. The four point charges on the O atoms are positive, the others are negative. Thus the whole molecular model is electroneutral. The point charge magnitude was adjusted to VLE data, namely the saturated liquid density and the vapor pressure.
In the last modeling step, the reduced unit method [59] were performed to fine-tune all model parameters, cf. Table 6.

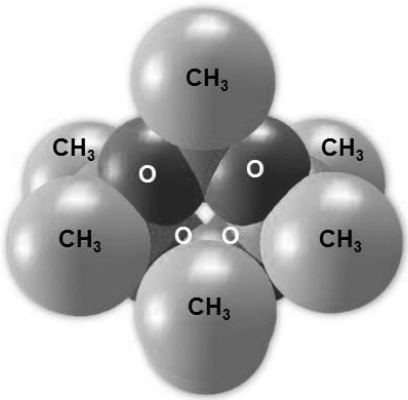

Figure 24: Present molecular force field model for octamethylcyclotetrasiloxane. CH_3: methyl Lennard-Jones site, O: oxygen Lennard-Jones site, not labeled: silica Lennard-Jones site. Note that the sphere diameters correspond to the Lennard-Jones size parameters, which are depicted according the molecular geometry scale.

Table 6: Parameters of the present force field models for hexamethyldisiloxane and octamethylcyclotetrasiloxane. Lennard-Jones interaction sites are denoted by the modeled atoms or atomic groups. Electrostatic interaction sites are denoted by point charges. Coordinates are given with respect to the center of mass in a principal axes system.

interaction site	x Å	y Å	z Å	σ Å	ε/k_B K	q C
hexamethyldisiloxane						
CH_3	-2.2796	-0.8698	-0.3545	3.8144	121.3515	
CH_3	-2.2150	1.2764	1.8825	3.8144	121.3515	
CH_3	0.5674	0.7717	-2.5502	3.8144	121.3515	
Si	-1.2334	-0.0730	1.0059	3.5133	15.1500	0.1458
O	0.1238	0.6680	0.3350	3.1180	43.6148	-0.2916
Si	1.2923	0.3890	-0.8475	3.5133	15.1500	0.1458
CH_3	-0.6830	-1.3930	2.2409	3.8144	121.3515	
CH_3	1.8613	-1.4145	-0.7878	3.8144	121.3515	
CH_3	2.7335	1.5447	-0.4734	3.8144	121.3515	
octamethylcyclotetrasiloxane						
CH_3	4.3198	-0.2718	1.3971	3.8181	122.4689	
CH_3	3.9847	-1.7562	-1.3286	3.8181	122.4689	
Si	3.1365	-0.7701	0.0267	3.5167	15.2895	0.3036
O	1.9213	-1.6816	0.7475	3.1248	44.0134	-0.3036
CH_3	1.6735	3.2187	-1.5120	3.8181	122.4689	
CH_3	1.4331	2.242	1.4613	3.8181	122.4689	
Si	1.3378	1.7784	-0.3619	3.5167	15.2895	0.3036
O	2.4782	0.5925	-0.7067	3.1248	44.0134	-0.3036
CH_3	-2.2590	1.2815	1.3636	3.8181	122.4689	
CH_3	-2.6052	-0.1997	-1.3611	3.8181	122.4689	
Si	-1.4157	0.2953	0.0056	3.5167	15.2895	0.3036
O	-0.2012	1.2041	-0.7199	3.1248	44.0134	-0.3036
CH_3	0.2869	-2.6955	-1.4467	3.8181	122.4689	
CH_3	0.0459	-3.7042	1.5158	3.8181	122.4689	
Si	0.3828	-2.2517	0.3814	3.5167	15.2895	0.3036
O	-0.7576	-1.0687	0.7370	3.1248	44.0134	-0.3036

7.2 Validation of the molecular models

To validate the present force field models for MM and D4, simulation results for the VLE, homogeneous liquid density, speed of sound, second virial coefficient and transport properties were compared with experimental data from the literature and with correlations from the DIPPR database [60]. All simulation data are listed in Tables B.1 to B.8 in the appendix. Simulation details are given in the appendix as well.

7.2.1 Vapor-liquid equilibrium data

The simulation data for the saturated liquid density, saturated vapor density, vapor pressure and Enthalpy of vaporization of MM and D4 are presented in Figures 25 to 27. The relative deviations of these data from the respective DIPPR correlation are shown in Figure 28 for MM and in Figure 29 for D4. Experimental data points taken from the literature were added to all plots as well.

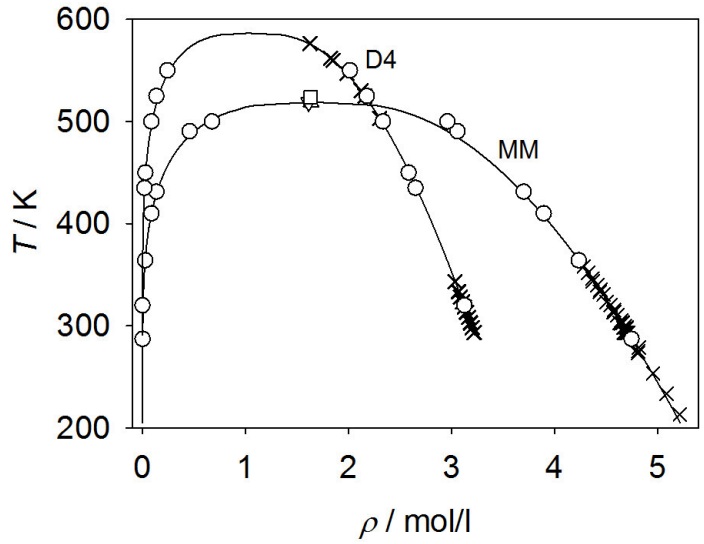

Figure 25: Saturated densities of hexamethyldisiloxane and octamethylcyclotetrasiloxane: (○) simulation data, this work; (×) experimental data [30, 60]; (□) critical point of the present molecular model for hexamethyldisiloxane; (△), (▽) experimental critical point of hexamethyldisiloxane [30, 60] ; (—) correlation of experimental data from the DIPPR database [60].

Saturated density

For the saturated liquid density of MM experimental data are available between 213 and 358 K only. Figure 28 illustrates that the simulation data in this region are well in the range of the experimental data and the DIPPR data. With rising temperature, where no experimental data are available, the deviation between molecular simulation and the DIPPR correlation rises. At 410 and 431 K it is almost 0.5 % and at 490 K, near to the critical temperature, it is 6.4 %.
For the saturated liquid density of D4 the simulation data agree very well with the experimental data over a wide temperature range, cf. Figure 29. At temperatures between 320 and 500 K the relative deviations between molecular simulation and experiment are less than 0.5 %. At 550, near the critical point, the relative deviation rises up to only 3 %.

Vapor pressure

For the vapor pressure of MM the relative deviations between the molecular simulation data and the DIPPR correlation are less than 5 % for all simulation points, even near the critical point. Note that the experimental data between about 280 and 410 K scatter in this 5 % range, too.
From Figure 29 it can be seen that the mean relative deviation between the simulation data for the vapor pressure of D4 and the DIPPR correlation is around 6 % for data points above 435 K. However, the simulation point at 320 K provides a worse result. Due to its large error bar it can be assumed that this outcome is a consequence of sampling difficulties at low temperatures.

Enthalpy of vaporization

The simulation data for the Enthalpy of vaporization of MM agree well with the experimental results and the data from the DIPPR correlation over the whole temperature range from 287 to 500 K. The relative deviations are throughout less than about 3 %, with the exception of the point at 490 K.
For the Enthalpy of vaporization of D4, the relative deviation rises steadily from -2 % at 320 K up to 8 % near the critical point at 550 K.

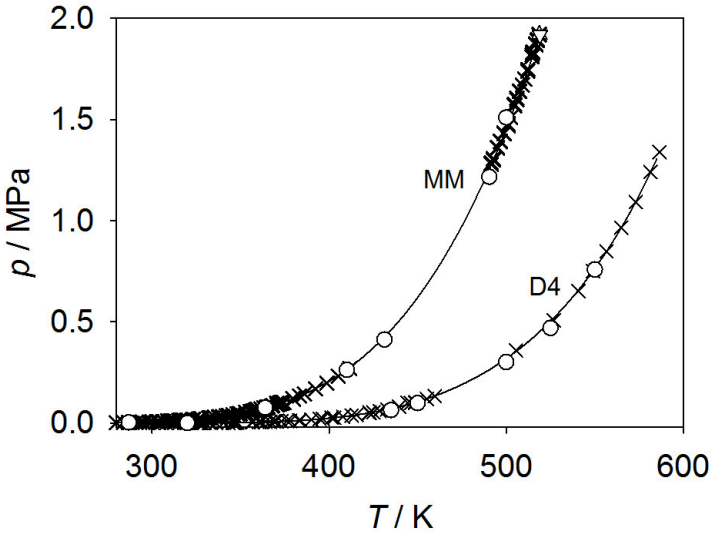

Figure 26: Vapor pressure of hexamethyldisiloxane and octamethylcyclotetrasiloxane: (○) simulation data, this work; (×) experimental data [30, 60]; (□) critical point of the present molecular model for hexamethyldisiloxane; (△), (▽) experimental critical point of hexamethyldisiloxane [30, 60]; (—) correlation of experimental data from the DIPPR database [60].

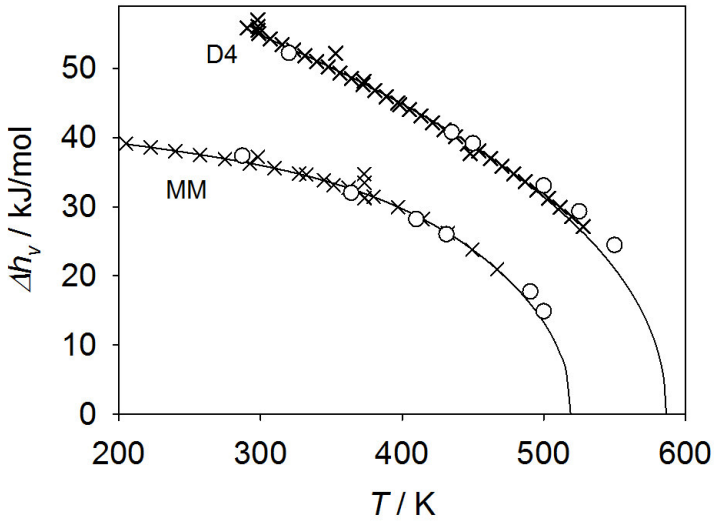

Figure 27: Enthalpy of vaporization of hexamethyldisiloxane and octamethylcyclotetrasiloxane: (○) simulation data, this work; (×) experimental data [30, 60]; (—) correlation of experimental data from the DIPPR database [60].

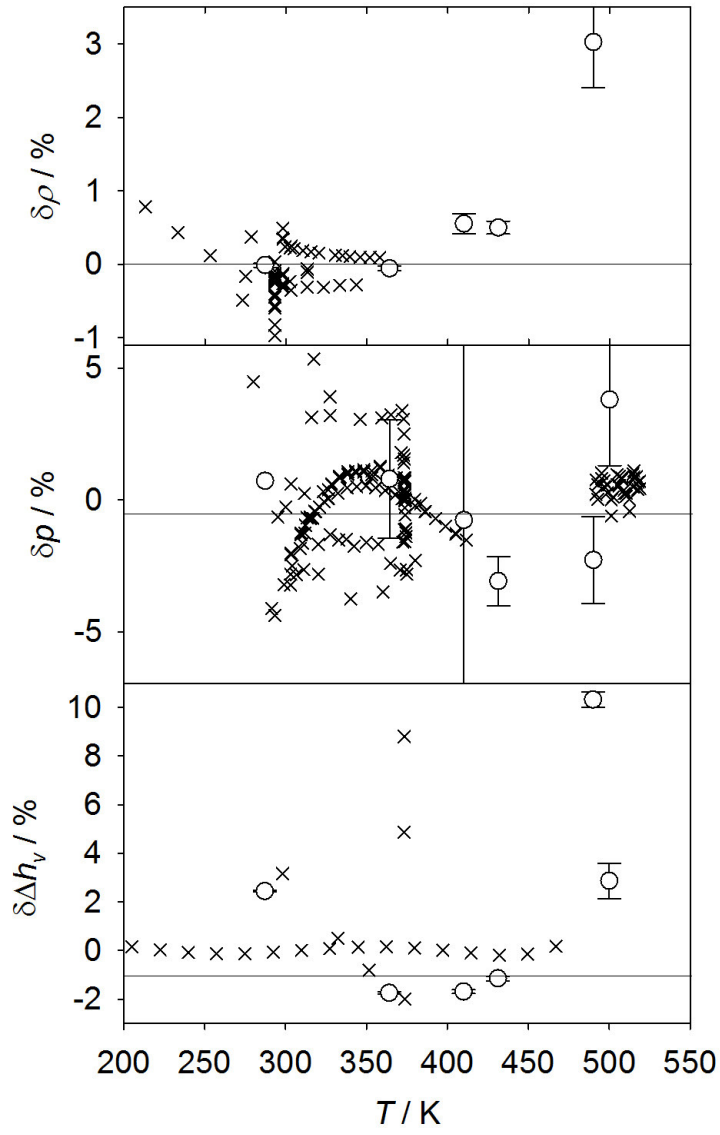

Figure 28: Relative deviations of vapor-liquid equilibrium properties of hexamethyldisiloxane from the DIPPR correlation [60] ($\delta z = (z_i - z_{dippr})/z_{dippr}$). (○) simulation data, this work; (×) experimental data [30, 60].

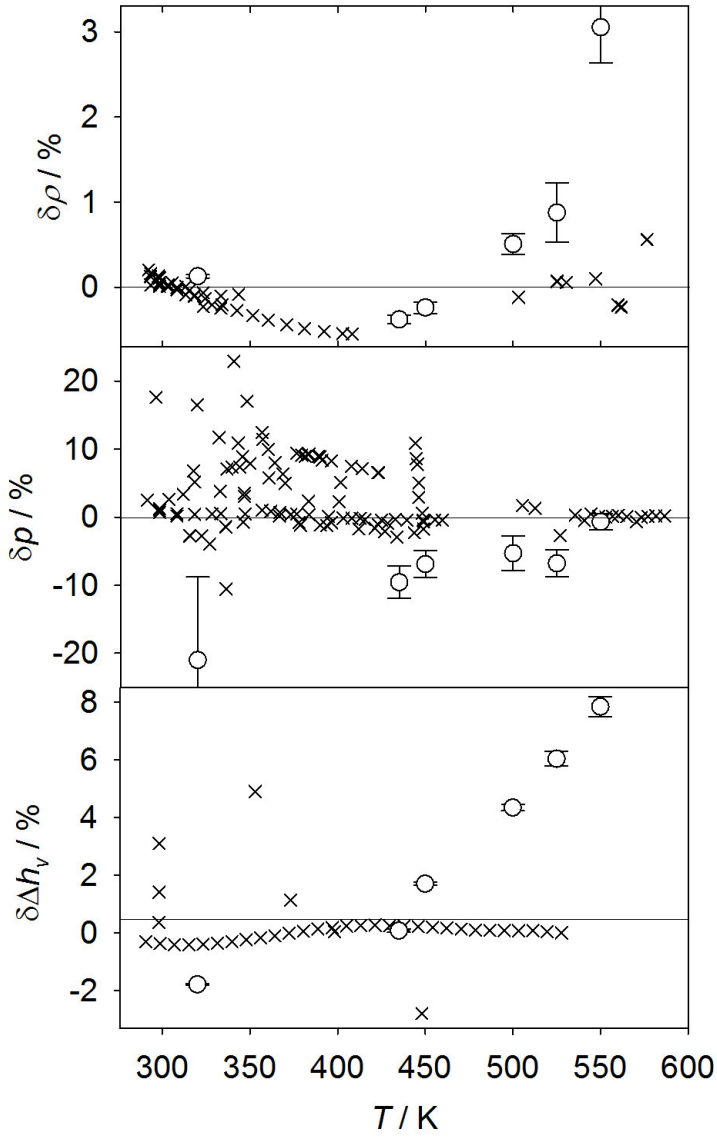

Figure 29: Relative deviations of vapor-liquid equilibrium properties of octamethylcyclotetrasiloxane from the DIPPR correlation [60] ($\delta z = (z_i - z_{dippr})/z_{dippr}$). (○) simulation data, this work; (×) experimental data [30, 60].

7.2.2 Homogeneous liquid density

The simulation results for the homogeneous liquid density of MM were compared to experimental data published by McLure *et al.* [76] and by Abbas [77]. McLure *et al.* provide data at 0.1013 MPa, Abbas performed measurements over a wide temperature and pressure range. Figure 30 shows the results of the comparison at temperatures from 303 to 427 K up to a pressure of 130 MPa. It can be seen that the agreement between simulation data and experimental data is very satisfying. In general, the relative deviation is less than 0.2 %. For the three data points at 0.1013 MPa it is slightly higher. The homogeneous liquid density of D4 was predicted by simulation in a temperature range from 303 to 427 K up to a pressure of 140 MPa and compared to experimental data by Wappmann [78], Estil and Wolf [79] as well as Herring and Winnick [80]. As can be seen in Figure 31, the relative deviations are predominantly below 0.5 %.

7.2.3 Speed of sound

The speed of sound c was calculated with Equation (44). Hereby, except for c_p^{id} which was obtained from the ideal gas part of the EOS by Colonna *et al.* [71], all data on the right hand side of Equation (44) were obtained directly by molecular simulation.

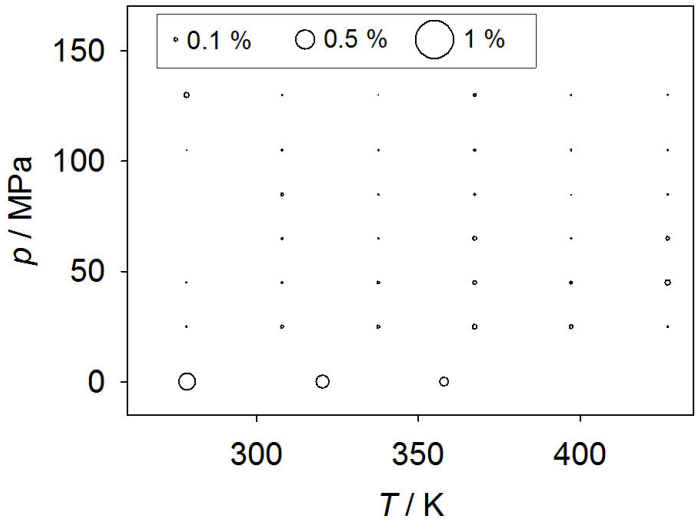

Figure 30: Density of hexamethyldisiloxane in the homogeneous region. Relative deviations between present simulation data and experimental data [76, 77] ($\delta z = (z_{\mathrm{sim}} - z_{\mathrm{exp}})/z_{\mathrm{exp}}$). The size of the bubbles indicates the magnitude of the relative deviation.

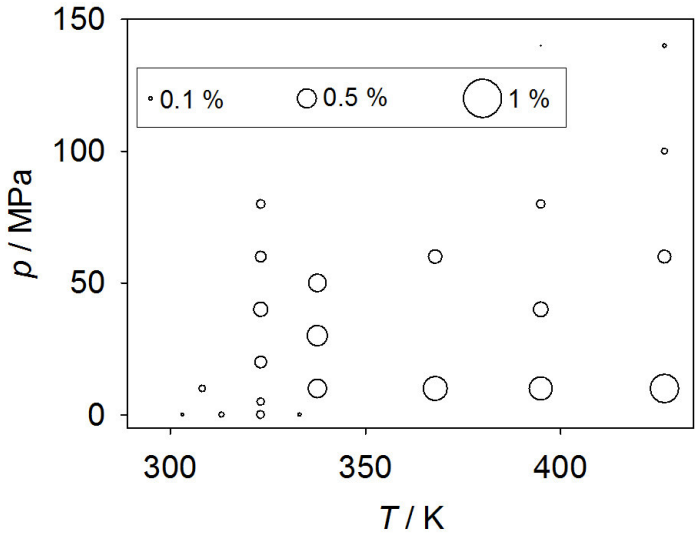

Figure 31: Density of octamethylcyclotetrasiloxane in the homogeneous region. Relative deviations between present simulation data and experimental data [78–80] ($\delta z = (z_{\mathrm{sim}} - z_{\mathrm{exp}})/z_{\mathrm{exp}}$). The size of the bubbles indicates the magnitude of the relative deviation.

For MM, the simulation results were compared with new experimental data generated in our group [81]. For D4, experimental data published by Niepmann and Schmidt [82] were found in the literature in addition to new data generated in our group [81].

As can be seen in Figure 32, the simulation results for MM are in a very good line with the new experimental data points at the four investigated isotherms 365, 413, 473 and 573 K up to a pressure of 14 MPa. Nearly all simulation points agree with the experiment within their statistical uncertainties.

The speed of sound of D4 was predicted by molecular simulation at the isotherms 350, 400, 450 and 500 K. The maximum pressure was 60 MPa. Figure 33 shows the comparison with the available experimental data. For pressures below 20 MPa, the D4 model yields results of nearly the same accuracy as the MM model. Considering the statistical uncertainties, all simulation data match very well with the experimental data. However, at higher pressures, the D4 model partly overpredicts the speed of sound. In the region between 20 and 60 MPa, the mean relative deviation of all simulation points to the experimental data is about 3.5 %.

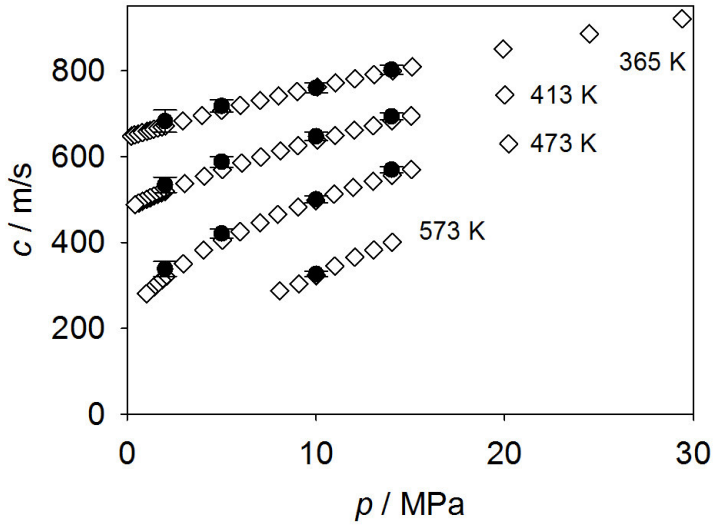

Figure 32: Speed of sound of hexamethyldisiloxane in the homogeneous region: (●) simulation data, this work; (◊) experimental data [81].

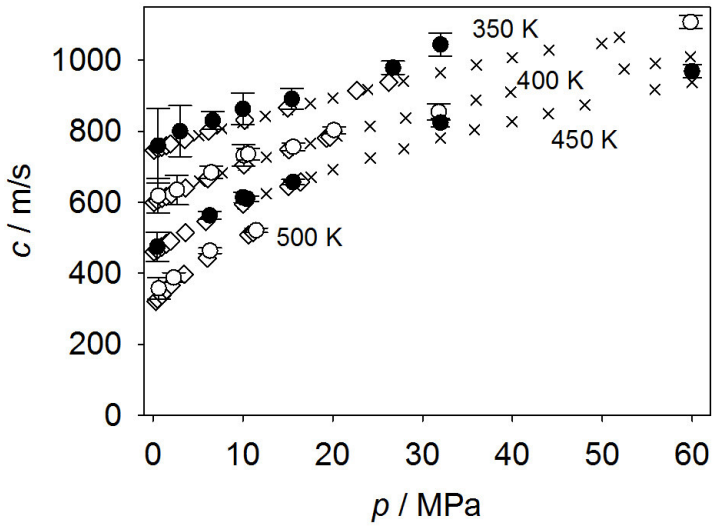

Figure 33: Speed of sound of octamethylcyclotetrasiloxane in the homogeneous region: (●), (○) simulation data, this work; (◊) experimental data [81]; (×) experimental data by Niepmann and Schmidt [82].

7.2.4 Second virial coefficient

The second virial coefficient was predicted over a temperature range from 220 to 1500 K for MM and from 270 to 1500 K for D4 by evaluating Mayer's f-function. This approach was described e.g. by Eckl *et al.* [62]. Figure 34 shows the simulation results in comparison with experimental data from the literature and a correlation of these experimental data from the DIPPR database [60]. At high temperatures the simulation data agree well with the experimental data for MM and D4. At low temperatures both models overpredict the second virial coefficient slightly. The mean absolute deviation over the respective whole temperature range is below 1.4 l/mol for both MM and D4.

7.2.5 Transport properties

Thermal conductivity and shear viscosity of liquid MM and D4 were obtained by equilibrium molecular dynamics (EMD) simulations following the Green-Kubo formalism, cf. Guevara-Carrion *et al.* [63]. Figures 35 to 38 show the simulation results for MM compared with experimental data from the literature and a correlation from the DIPPR database.

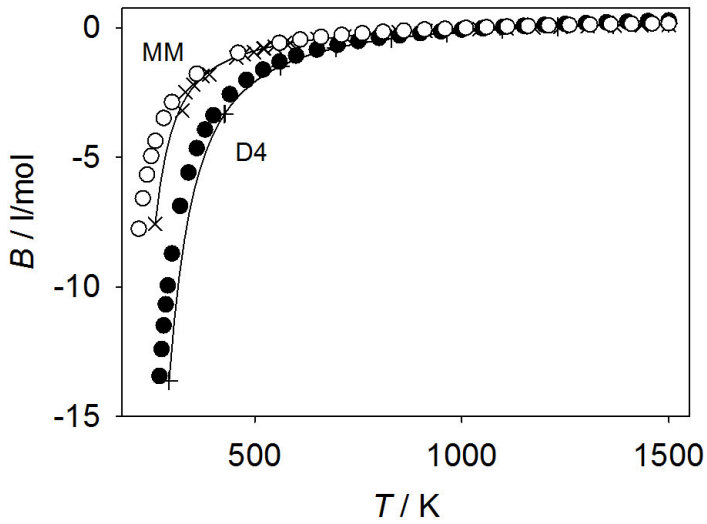

Figure 34: Second virial coefficient of hexamethyldisiloxane and octamethylcyclotetrasiloxane: (○) simulation data, this work; (×) experimental data [60]; (—) correlation of experimental data from the DIPPR database [60].

Thermal conductivity

For the thermal conductivity of MM, simulations were performed at the three isotherms 295, 411 and 508 K, cf. Figure 35. The simulations agree with the experimental data by Abbas [77] mostly within their statistical uncertainties. Only the three points at the lowest pressures are located significantly below the points by Abbas.
Figure 36 shows the simulation results for the thermal conductivity of D4 at 0.1 MPa from 290 to 440 K in comparison with experimental data by Missenard [96] and a correlation from the DIPPR database. It can be seen that the molecular model slightly underpredicts the thermal conductivity over the whole temperature range. Thus the mean relative deviation of all simulation points from the correlation is 17 %.

Shear viscosity

For the shear viscosity of MM experimental data at 0.1 MPa, published by Abbas [77], Kirk [83], Lavygin *et al.* [84], Rowe *et al.* [85], Hunter *et al.* [86], Hurd [87] and Wilcock [88] were found in the literature. Comparable with the results for the thermal conductivity of MM at low pressures, the shear viscosity from simulations at 0.1 MPa are about 0.1 Pa s below the experimental data in the entire temperature range from 280 to 350 K, cf. Figure 37. The mean relative deviation of the simulation data with respect to the correlation from the DIPPR

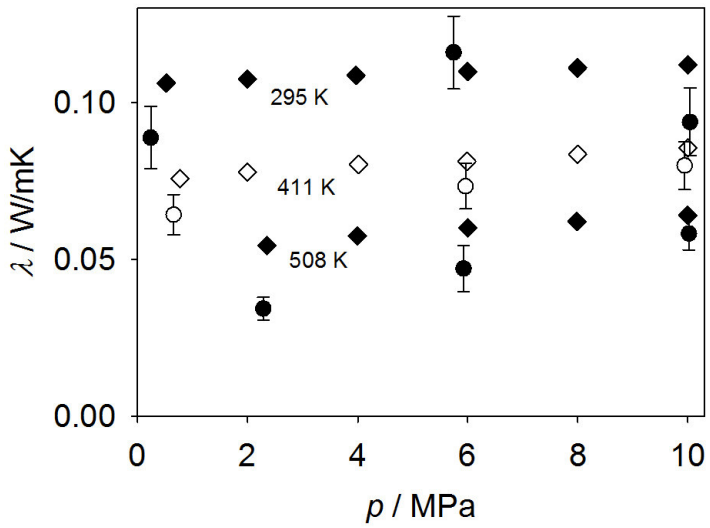

Figure 35: Thermal conductivity of hexamethyldisiloxane: (○), (●) simulation data, this work; (◊), (♦) experimental data by Abbas [77]. The black bullets represents the same isotherms as the black trapezoids.

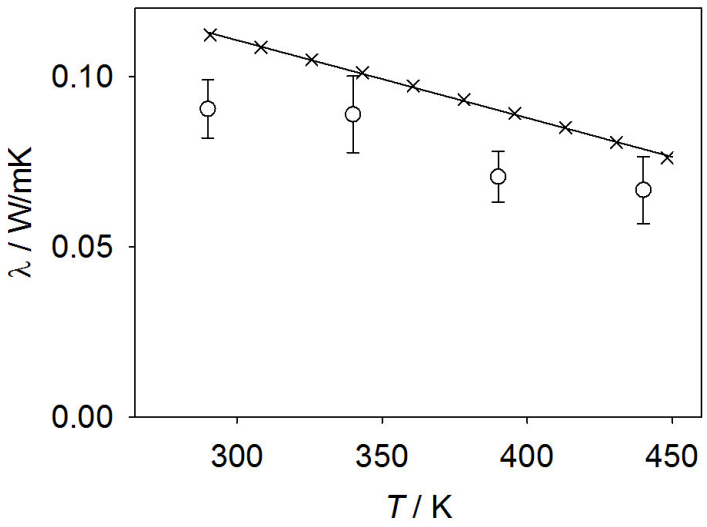

Figure 36: Thermal conductivity of octamethylcyclotetrasiloxane at 0.1 MPa: (○) simulation data, this work; (×) experimental data by Missenard [96]; (—) correlation of experimental data from the DIPPR database [60].

database is about 18 %.

Figure 38 illustrates the comparison between the simulation results for the shear viscosity of D4 and experimental data at 0.1 MPa by Hunter *et al.* [86], Hurd [87], Wilcock [88], Mills[97], Marsh [98], Reuthe [100] and Waterman [99]. The simulations were carried out at temperatures between 300 and 370 K. With the exception of the simulations at 300 K, the simulation results agree with the experimental data from the literature within their statistical uncertainties.

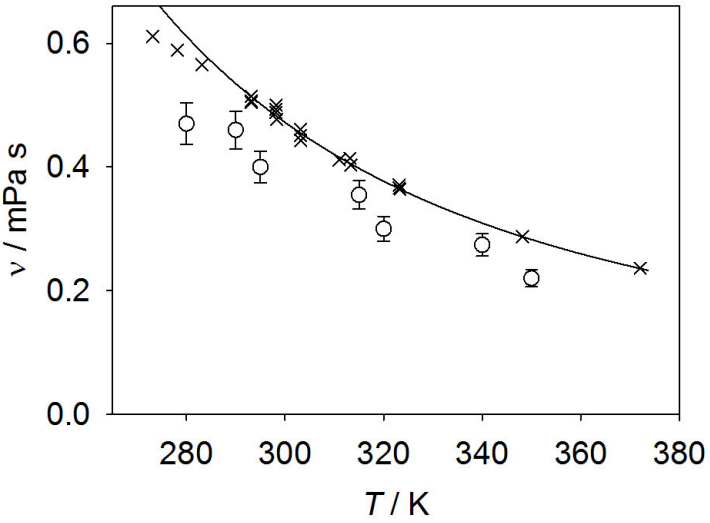

Figure 37: Shear viscosity of hexamethyldisiloxane at 0.1 MPa: (○) simulation data, this work; (×) experimental data by Abbas [77], Kirk [83], Lavygin *et al.* [84], Rowe *et al.* [85], Hunter *et al.* [86], Hurd [87] and Wilcock [88]; (—) correlation of experimental data from the DIPPR database [60].

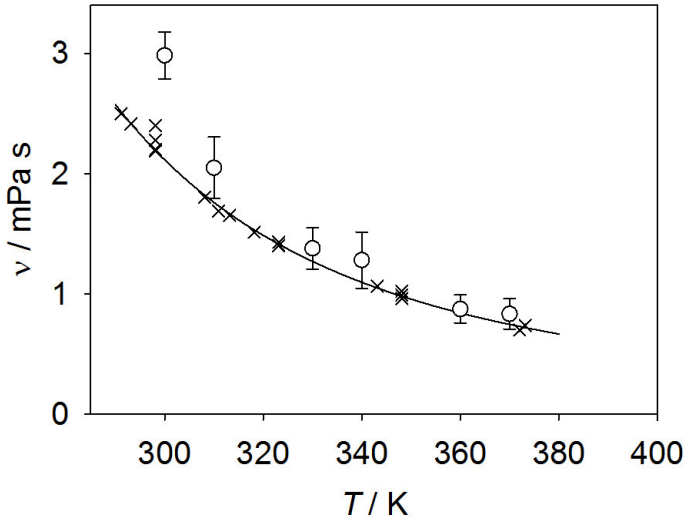

Figure 38: Shear viscosity of octamethylcyclotetrasiloxane at 0.1 MPa: (○) simulation data, this work; (×) experimental data by Hunter *et al.* [86], Hurd [87], Wilcock [88], Mills [97], Marsh [98], Waterman [99] and Reuthe [100]; (—) correlation of experimental data from the DIPPR database [60].

7.3 Conclusion

New force field models for hexamethyldisiloxane (MM) and octamethylcyclotetrasiloxane (D4) were presented in this work. The geometry (bond lengths and angles) of both molecules was determined with the help of QC calculations. The intermolecular interactions were considered by nine LJ sites and nine point charges in case of MM and 16 LJ sites and 16 point charges in case of D4. For MM two parameters were adjusted to experimental VLE data from the literature and for D4 one parameter.

To validate the new models, simulation results were compared with experimental data from the literature and correlations of these data taken from the DIPPR database. Both models provide satisfying deviations in terms of the VLE properties saturated liquid density, vapor pressure and Enthalpy of vaporization. The MM model yields very good results for the homogeneous liquid density (the relative deviations are below 0.2 % in general), the speed of sound (nearly all simulation points agree with the experiment within their statistical uncertainties), the second virial coefficient and the thermal conductivity at higher pressures. At low pressures the thermal conductivity and the shear viscosity were underpredicted. The D4 model yields slightly higher deviations for the homogeneous liquid density. However, it performs very well in terms of the speed of sound, the second virial coefficient and the shear viscosity. The thermal conductivity at 0.1 MPa was underpredicted slightly over the whole examined temperature range.

8 Decafluorobutane

This work arose within the scope of the project "Development of a database and predictive models for new alternative refrigerants", which was funded by the Bundesministerium für Bildung und Forschung (BMBF) and the equivalent institution in South Africa. The objective of this project was to investigate new alternative refrigerants with similar or even better features than common refrigerants, such as chlorofluorocarbons (CFC). Hereby, the considered properties are VLE behavior, Ozone Depletion Potential (ODP), Global Warming Potential (GWP) and manufacturing costs.
Perfluorocarbons (PFC) are one of the substance groups which were investigated within the project. Due to the fact that PFC have a large capacity to dissolve gases, there is a potential as physical solvents in adsorption chillers or petrochemical refinery gas absorption processes. The aim of this work was to obtain a deeper knowledge on PFC using the example of decafluorobutane (C_4F_{10}).
For this purpose, a new force field model for C_4F_{10} was developed, which consists of 14 LJ sites and 14 point charges to describe the intermolecular interactions. Hereby, the foundation was laid to carry out further molecular simulations of mixtures containing C_4F_{10} to investigate its capability as a solvent. In addition, the pure substance parameters of the Peng-Robinson EOS considering the Mathias-Copeman mixing rule were adjusted for further work.

8.1 Molecular model for decafluorobutane

A rigid and electroneutral force field model for C_4F_{10} was developed in this work, cf. Figure 39. The geometry was determined by QC calculations using the software package GAMESS(US) [56] with the Hartree-Fock method and the 6-31G basis set.
To describe the dispersive and repulsive interactions, the LJ 12-6 potential was used and one LJ site was placed on each of the four carbon (C) and ten fluorine (F) atoms. The LJ energy and size parameters for the C site σ_C, ε_C and for the F site σ_F, ε_F were initially adopted from a force field model for 1,1,1,2,3,3,3-heptafluoropropane (R227ea) by Eckl *et al.* [101]. Subsequently, σ_F and ε_F were adjusted to experimental VLE data from the literature (saturated liquid density and vapor pressure).

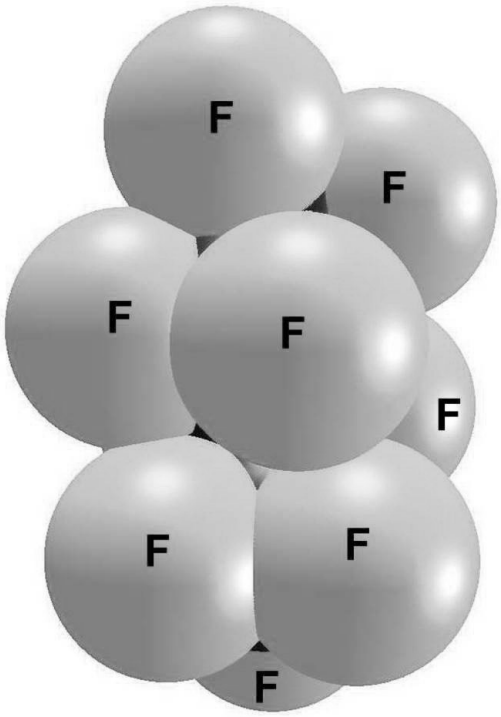

Figure 39: Present molecular force field model for decafluorobutane. F: fluorine Lennard-Jones site, not labeled: carbon Lennard-Jones site. Note that the sphere diameters correspond to the Lennard-Jones size parameters, which are depicted according to the molecular geometry scale.

To model the electrostatic interactions, a point charge were placed on each of the 14 atoms. The charge magnitudes were calculated with a Mullikan population analysis [57] with the result that positive charges are located at the C atoms and negative at the F atoms. The molecule as a whole is electroneutral.
Finally, the reduced unit method [59] was used to fine-tune all parameters for the geometry, LJ sites and point charges simultaneously. The resulting parameters of the force field model are listed in Table 7.

8.2 Simulation results for decafluorobutane

The present force field model for C_4F_{10} was validated by comparing the simulation results with experimental data from the literature [102–108] and with correlations of the experimental data from the DIPPR database [60]. The model was validated in terms of the saturated liquid density, vapor pressure, Enthalpy of vaporization and the second virial coefficient. The uncertainties of the DIPPR correlations are stated to be less than 3 % for the saturated liquid

Table 7: Parameters of the new molecular model for decafluorobutane developed in this work. Lennard-Jones interaction sites and point charge magnitudes are denoted by the modeled atom. Coordinates are given with respect to the center of mass in a principal axes system.

interaction site	x Å	y Å	z Å	σ Å	ε/k_B K	q e
C1	-1.6822	0.2798	-0.9876	2.8020	10.5549	0.8774
C2	-0.1821	0.0740	-0.7473	2.8020	10.5549	0.4975
C3	0.2340	0.1133	0.7276	2.8020	10.5549	0.4975
C4	1.6400	-0.4323	1.0036	2.8020	10.5549	0.8774
F1	-2.3735	-0.7873	-0.5805	2.8884	58.6998	-0.2648
F2	-0.6419	-0.6210	1.4543	2.8884	58.6998	-0.2871
F3	0.1571	-1.1281	-1.2709	2.8884	58.6998	-0.2871
F4	1.6681	-1.7578	0.8472	2.8884	58.6998	-0.2648
F5	-1.8919	0.4583	-2.2953	2.8884	58.6998	-0.2700
F6	-2.1085	1.3612	-0.3243	2.8884	58.6998	-0.2697
F7	1.9808	-0.1374	2.2616	2.8884	58.6998	-0.2700
F8	0.1968	1.3969	1.1467	2.8884	58.6998	-0.2833
F9	0.4816	1.0506	-1.4033	2.8884	58.6998	-0.2833
F10	2.5217	0.1296	0.1680	2.8884	58.6998	-0.2697

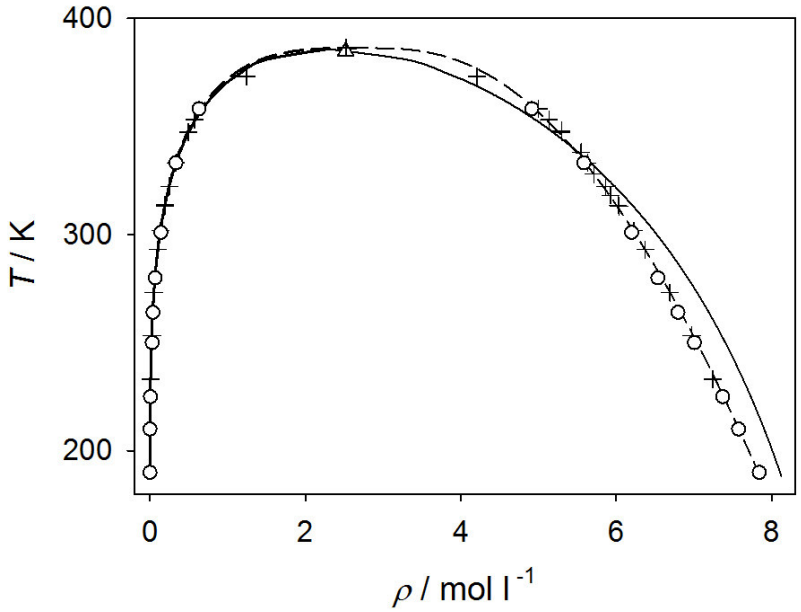

Figure 40: Saturated densities of perfluorobutane: (○) simulation data, this work; (△) critical point of the present molecular model; (+) experimental data [102, 103]; (- - -) DIPPR correlation of experimental data [60]; (—) Peng-Robinson EOS. The statistical uncertainties of the simulation data are within symbol size.

density, less than 5 % for the vapor pressure, less than 10 % for the Enthalpy of vaporization and ± 0.76 l/mol for the second virial coefficient. In the following, the main results are summarized. All present C_4F_{10} simulation data are given in numerical form in the appendix. Figure 40 illustrates the simulation results for the saturated densities in a temperature range from 190 to 358 K compared with the experimental data and the DIPPR correlation. Moreover, the Peng-Robinson EOS is shown (cf. Section 8.3 for the discussion of the Peng-Robinson EOS). The relative deviations of the simulation and experimental data points from the DIPPR correlation are plotted in Figure 41 for the saturated liquid density, vapor pressure and Enthalpy of vaporization. As can be seen from these diagrams, the agreement between simulation, experiment and correlation is very satisfying for the saturated liquid density over the entire temperature range. The most serious deviation between simulation and experimental data was found at high temperatures near the critical point. However, the mean relative deviation over the temperature range from 190 to 358 K is only 0.6 %.

Figure 42 shows the vapor pressure curve of C_4F_{10} from simulation, experiment and the DIPPR correlation. As can be seen in Figure 41, there is a good agreement between these data at temperatures above about 270 K. At lower temperatures, the simulation data scatter around the zero line and the error bars are larger. The maximum can be found at 250 K,

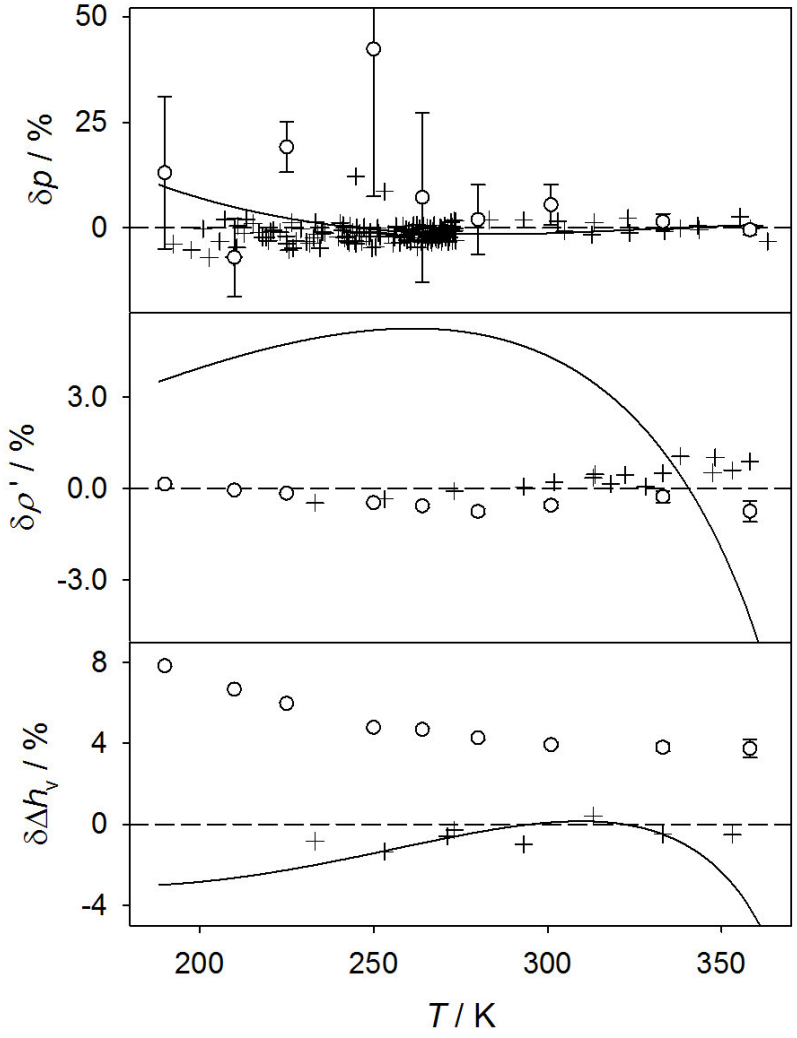

Figure 41: Relative deviations of vapor-liquid equilibrium properties of decafluorobutane from the DIPPR correlation [60] ($\delta z = (z_i - z_{\text{dippr}})/z_{\text{dippr}}$): (○) simulation data, this work; (+) experimental data [102–104]; (—) Peng-Robinson EOS. The statistical uncertainties of the molecular simulation data are not shown if they are within symbol size.

which is due to the insufficiency of Widom's test molecule method at low temperatures. The chemical potential was calculated with Widom's method at high temperatures. Due to the fact that the simulation results based on Widom's method are worse at lower temperatures, the gradual insertion method was used instead at temperatures below 250 K. The deviation plot points out that the simulation data agree with the experimental data for almost every temperature within their uncertainties. The mean relative deviation over the temperature range from 190 to 358 K is 5.9 %.

The simulated Enthalpy of vaporization is plotted in Figure 43 as a function of the temperature in a range of 190 to 358 K. Figure 41 illustrates that the smallest relative deviation with respect to the experimental data and the DIPPR correlation occurs at high temperatures and rises gradually up to about 8 % at 190 K with falling temperature. The mean relative deviation over the temperature range from 190 to 358 K is 5.1 %.

Figure 44 shows the simulation results for the speed of sound compared with experimental data by Vacek *et al.* [106] at 0.1 MPa. It can be seen that the simulation points agree with the experiment over the whole temperature range from 272 to 305 K within their statistical uncertainties.

Figure 45 presents the molecular simulation results in comparison to experimental data [105, 107, 108] and to the DIPPR correlation [60] for the second virial coefficient. The achieved agreement is very satisfying. The average absolute deviation is only 0.08 l/mol, which is well within the uncertainty of the DIPPR correlation.

8.3 Peng-Robinson equation of state

To describe the VLE behavior of C_4F_{10} with a cubic EOS, the Peng-Robinson EOS considering the Mathias-Copeman alpha function (cf. Section 4 for details) was used. Hereby, the three parameters c_1, c_2 and c_3 from Equation (23) were adjusted to all vapor pressure data which can be found in the Dortmunder Datenbank [30] simultaneously.

The saturated liquid and vapor densities $\rho' = 1/v'$ and $\rho'' = 1/v''$ at a given temperature T_S were calculated in the first step with Equation (19) in combination with the Maxwell criterion [29]. Subsequently, the obtained values for v' or v'' were applied in Equation (19) to calculate the vapor pressure p_S. Finally, the Enthalpy of vaporization Δh_v was determined by inserting v' and v'' in Equation (30).

Figures 40, 42 and 43 illustrate the Peng-Robinson EOS for ρ', ρ'', p_S and Δh_V in addition to the results from molecular simulation, experiment and the DIPPR correlations. The relative deviations with respect to the DIPPR correlations are plotted in Figure 41. For the vapor pressure at temperatures above 230 K, the Peng-Robinson EOS lies exactly within the exper-

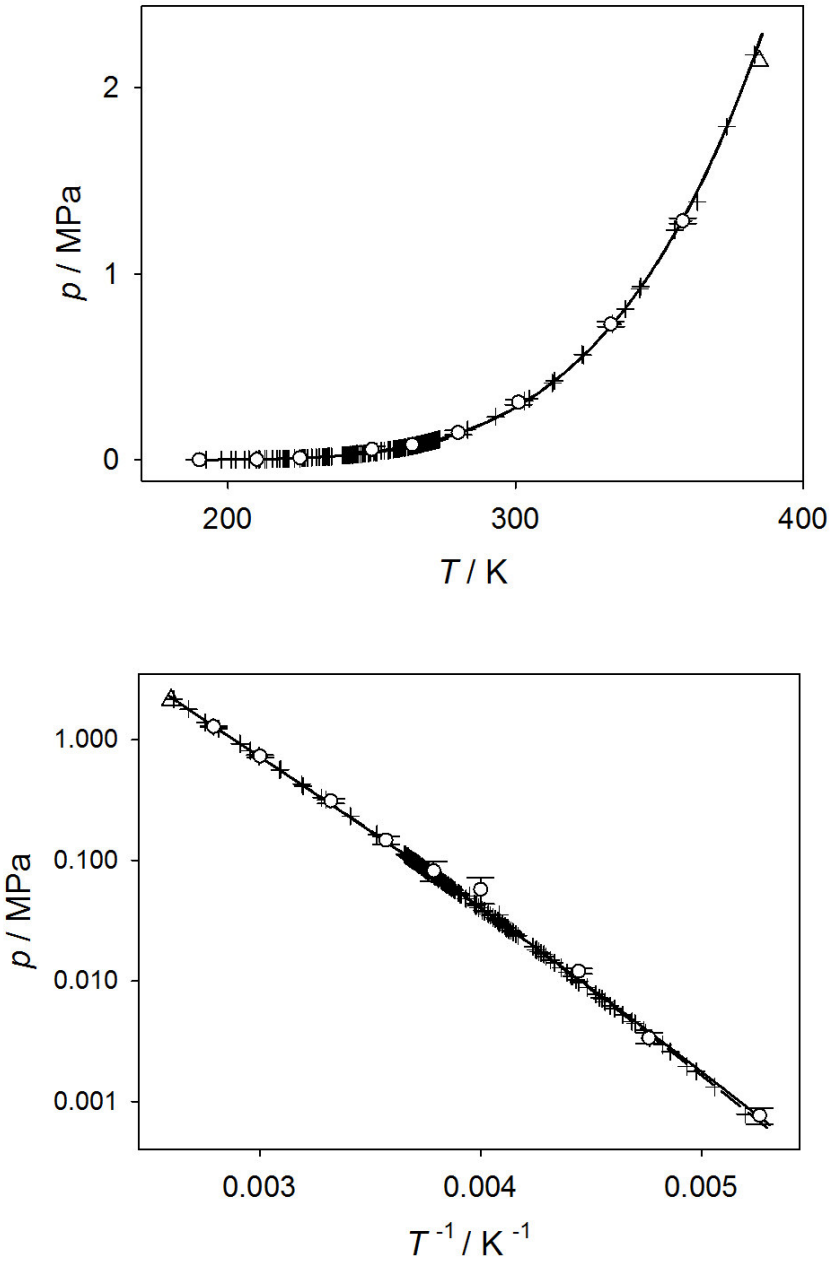

Figure 42: Vapor pressure of perfluorobutane: (○) simulation data, this work; (△) critical point of the present molecular model; (+) experimental data [102–104]; (- - -) DIPPR correlation of experimental data [60]; (—) Peng-Robinson EOS.

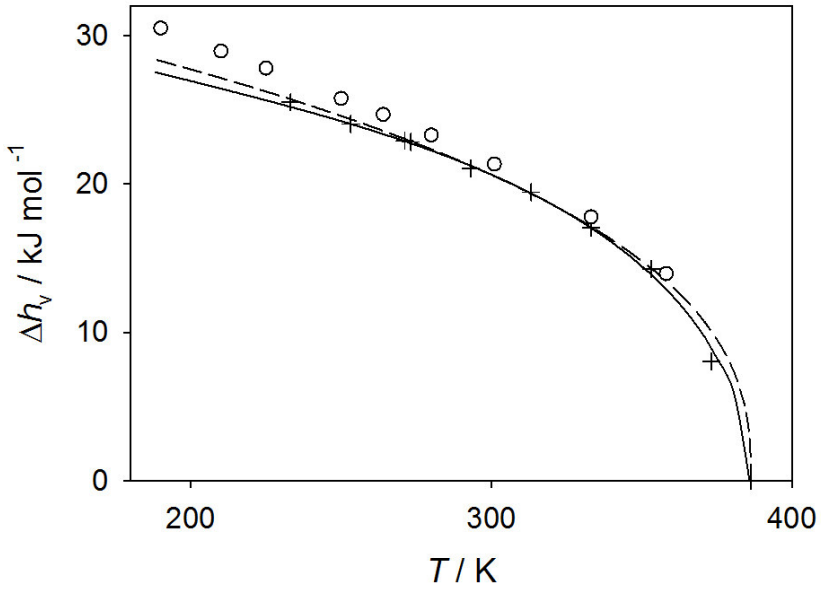

Figure 43: Enthalpy of vaporization of perfluorobutane: (○) simulation data, this work; (+) experimental data [102]; (- - -) DIPPR correlation of experimental data [60]; (—) Peng-Robinson EOS. The statistical uncertainties of the simulation data are within symbol size.

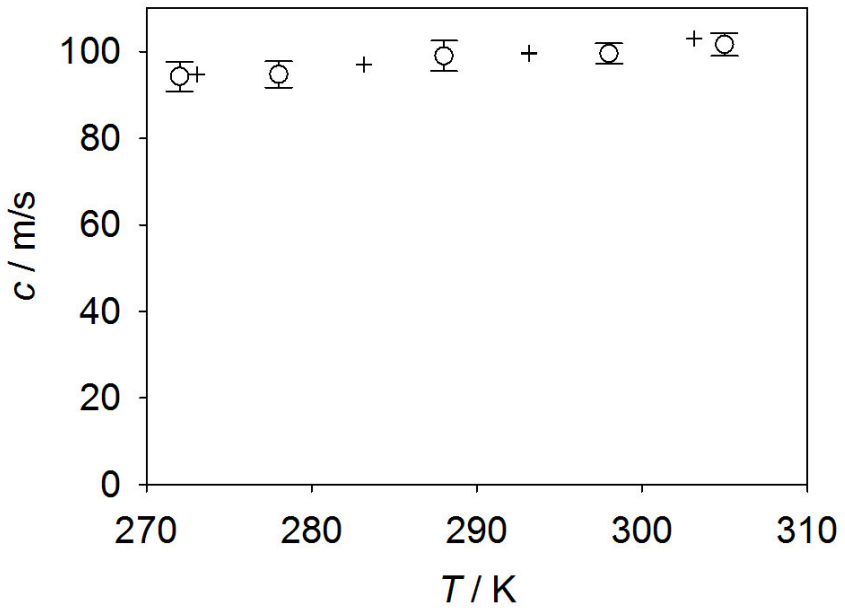

Figure 44: Speed of sound of perfluorobutane at 0.1 MPa: (○) simulation data, this work; (+) experimental data by Vacek *et al.* [106].

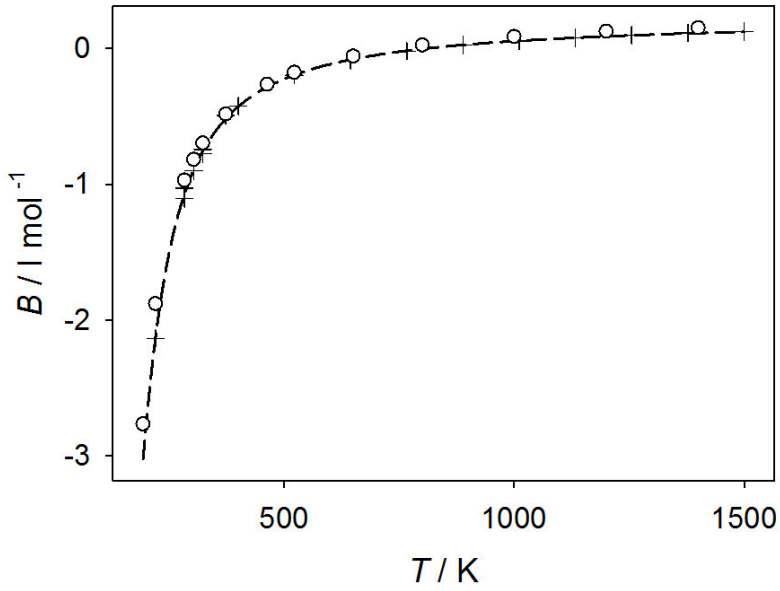

Figure 45: Second virial coefficient of perfluorobutane: (○) simulation data, this work, (+) experimental data [105, 107, 108], (- - -) DIPPR correlation of experimental data [60].

imental data points. Below 230 K the deviations are slightly higher. It is supposed that the very good agreement between Peng-Robinson equation and experiment is due to the fact that the parameters c_1, c_2 and c_3 from the Mathias-Copeman alpha function were solely adjusted to the experimental vapor pressure.

For the saturated liquid density, the relative deviations are larger than 3 % for temperatures below 300 K. At higher temperatures, the deviation curve drops down steeply. Thus, the saturated liquid density is underpredicted significantly near the critical point.

For the Enthalpy of vaporization, the Peng-Robinson EOS shows no relevant deviation from the experimental data in a temperature range between approximately 250 and 340 K. However, for smaller temperatures, the deviation decreases gradually and in the direction of the critical point, towards higher temperatures it decreases very strongly.

8.4 Conclusion

A new rigid and electroneutral force field model for C_4F_{10} was presented in this work. The model consists of 14 LJ sites and 14 point charges to describe the dispersive, repulsive and electrostatic interactions. During the modeling process two LJ parameters were adjusted to

experimental VLE data from the literature. The validation of the model by means of experimental data from the literature led to mean relative deviations of 0.6 % for the saturated liquid density, 5.9 % for the vapor pressure, 5.1 % for the Enthalpy of vaporization and an absolute deviation of 0.08 l/mol for the second virial coefficient.
In addition, three pure fluid parameters of the Peng-Robinson EOS using the Mathias-Copeman mixing rule were adjusted to experimental vapor pressure data from the literature. The Peng-Robinson EOS yields very good results in terms of the vapor pressure. However, for the saturated liquid density and the Enthalpy of vaporization the deviations with respect to experimental data are significant.

9 Mixture of carbon dioxide + 2,2-dimethyl-1-propanol

The present experimental work was carried out in the context of the research project "Understanding the role of electrostatic and dispersive interactions in fluid phase equilibria: A step towards fast and accurate first-principles predictions", which was funded by the Alexander von Humboldt Stiftung. The aim of the project was to handle well known, but until now unresolved, issues of the COSMO-SAC model [8, 109, 110], such as the neglect of the dispersive interactions in mixtures and the treatment of the long-range electrostatic interactions, with the help of molecular simulation. COSMO-SAC belongs to the COSMO based approaches, which allow to predict thermodynamic properties without any species-dependent parameter. The first step to reach the above discussed project aim was to assess a revised COSMO-SAC version by Hsieh *et al.* [8] on the basis of experimental data for various mixtures of supercritical carbon dioxide ($ScCO_2$) + low molar mass alcohols. Hereby, the low molar mass alcohols comprize methanol, ethanol, the propanols, butanols and pentanols. The phase behavior of mixtures of CO_2 + low molar mass alcohols is crucial for the design and optimization of extraction processes using these alcohols as co-solvents.

A literature research revealed that experimental data on the VLE are available for all binary mixtures of CO_2 + low molar mass alcohols, except for the mixture CO_2 + 2,2-dimethyl-1-propanol. This gap was closed in the present work by investigating the saturated liquid line of CO_2 + 2,2-dimethyl-1-propanol experimentally at the two isotherms 333.2 and 353.2 K up to a maximum pressure of 12.8 MPa. For this purpose, the existing experimental setup described in Section 2.1 was used in a modified version. The modifications were necessary to be able to load the measurement cell with 2,2-dimethyl-1-propanol, which is in the solid state under ambient conditions. For this purpose, a second high pressure spindle press was installed (cf. Section 9.1). Because of these modifications it was essential to modify the experimental procedure as well, (cf. Section 9.2).

Based on the measurement results, the Peng-Robinson EOS with the quadratic mixing rule was adjusted for further applications.

9.1 Modification of the experimental setup

The employed experimental setup is shown in Figure 46. It is a modification of the apparatus which was used for gas solubility measurements of the binary mixtures nitrogen + acetone and oxygen + acetone, cf. Section 6. Compared to the former installation, which is described in Section 2.1 in detail, a second high pressure spindle press was added to load the high pressure equilibrium cell with 2,2-dimethyl-1-propanol. To measure the temperature of the cell and the high pressure pumps, the calibrated platinum resistance thermometers T1 to T4 with a basic resistance of 100 Ω (Pt100) were used. The temperature measuring error was about ± 0.04 K. The calibrated pressure transducers P1 and P2 (model Super THE, Honeywell test & measurement, measuring ranges: 6.8 and 20 MPa for P1 and P2, respectively) with an accuracy of 0.05 % of their respective full measuring ranges were used to determine the pressure in the view cell and the supply pipes.

9.2 Modified experimental procedure

At the beginning of the measurement procedure, the high pressure spindle press A was cooled down to about 298 K and filled with CO_2 from the bottle. Hereby, the high spindle press was loaded completely with CO_2 in the liquid state. The high pressure spindle press B was loaded with 2,2-dimethyl-1-propanol from the reservoir via valve V1. Due to the fact that the melting temperature of 2,2-dimethyl-1-propanol is about 325 K at 0.1 MPa, it was filled in the solid state into the reservoir first and melted there. Therefore, the climate chamber was heated up to 353 K. After the spindle press was filled up with liquid 2,2-dimethyl-1-propanol completely, valve V1 was closed and the desired amount of 2,2-dimethyl-1-propanol was pumped into the heated equilibrium cell via valve TW-V1. The decant mass m_{prop} was determined volumetrically as described in Section 2.1.2. Next, the climate chamber and the equilibrium cell were brought to the desired measurement temperature and the liquid CO_2 was filled into the cell with the high pressure spindle press A until the CO_2 was solved completely in 2,2-dimethyl-1-propanol. The solvation process was supported by a magnetic stirrer and was observed visually with an endoscope. Coming from the homogeneous liquid state, in the next step, the pressure in the cell was decreased with the high pressure spindle press A in very small steps, until the first bubbles appeared and the saturated state was reached. At this state, the vapor pressure of the mixture was measured with the pressure transducer P2. In a last step, the composition was calculated from the mass m_{prop} and the mass of CO_2 m_{CO2}, which was filled into the cell and obtained volumetrically as well.

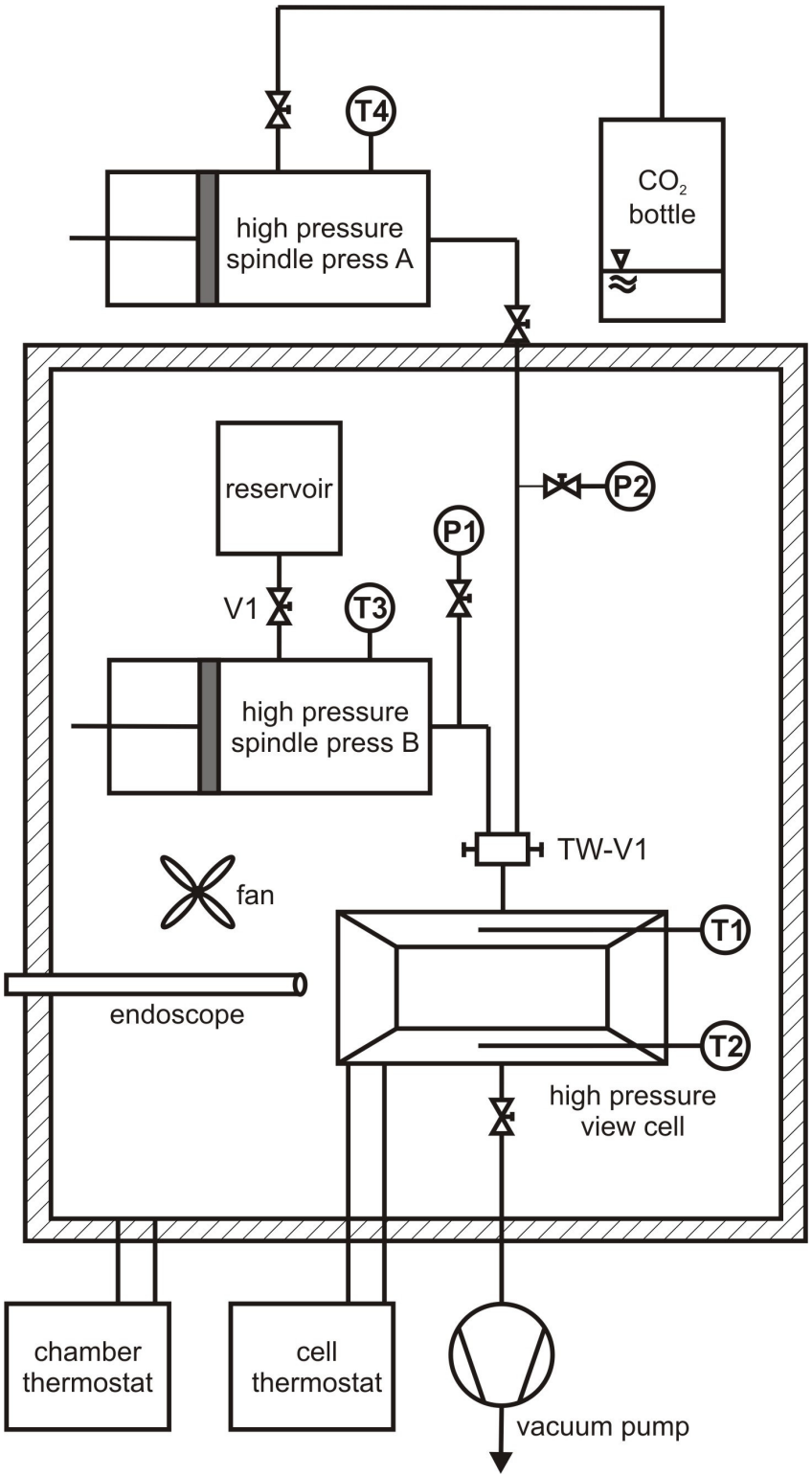

Figure 46: Schematic of the experimental setup for the measurements of CO_2 + 2,2-dimethyl-1-propanol. V1 indicates a valve, TW-V1 a three-way valve, TX a thermometer and PX a pressure transducer.

9.3 Results

Experimental results

The experimental results for the system CO_2 + 2,2-dimethyl-1-propanol are illustrated in Figure 47 and are listed in numerical form in the appendix. The saturated liquid line of this system was investigated at the two isotherms 333 and 353 K up to a maximum pressure of 12.8 MPa. Since the critical temperature of CO_2 is about 304 K, the saturated liquid line exhibits the typical course of a mixture with one supercritical component. Thus it shows a nearly linear course far away from the critical line of the mixture at lower mole fractions of CO_2 x_{CO2}. With rising x_{CO2}, the linear slope turns into a degressive slope until the critical point of the mixture is reached with a much slower rising of the pressure. In a comparable temperature range, where CO_2 is supercritical, other mixtures of CO_2 + low molar mass alcohols show a similar behavior, such as CO_2 + ethanol, CO_2 + 2-propanol and CO_2 + 1-butanol [30].

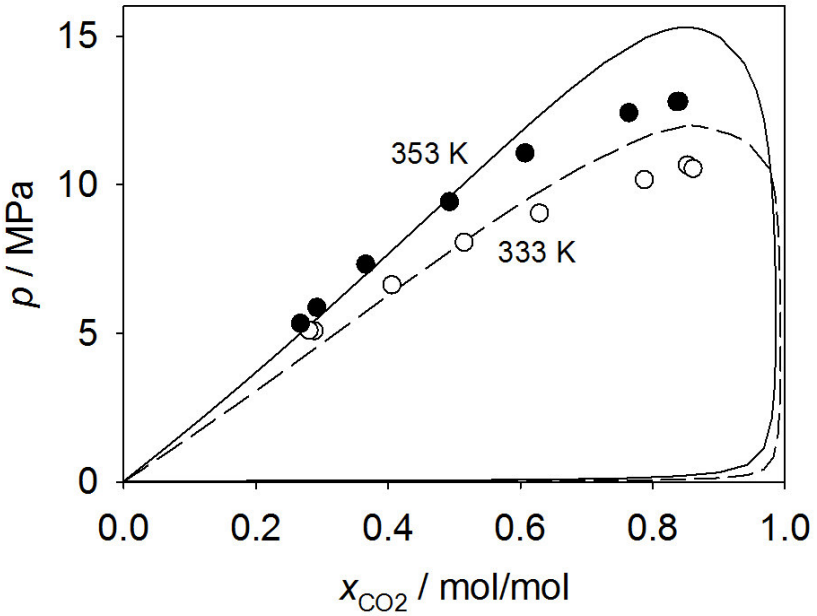

Figure 47: Saturated liquid line of carbon dioxide + 2,2-dimethyl-1-propanol: (○), (●) experimental data, this work; (—), (- - -) Peng-Robinson EOS with the quadratic mixing rule, this work. The solid line represents the same isotherm as the solid symbols.

Peng-Robinson equation of state

The Peng-Robinson EOS was adjusted to all obtained experimental data simultaneously. For this purpose, the EOS parameters a and b for the pure substances were calculated with Equations (20) and (21), cf. Section 4. Considering the quadratic mixing rule, the mixture parameters a_m and b_m were determined with Equations (25) and (26). Hereby the parameter k_{ij} = 0.1 yields the best results compared with the experimental data.
The adjusted Peng-Robinson EOS is illustrated in Figure 47 in addition to the present experimental data points at 333 and 353 K. It can be seen that the Peng-Robinson EOS agrees well with the experiment at liquid mole fractions x_{CO2} less than about 0.5 mol/mol for both temperatures. In this composition region, the EOS exhibits a nearly linear slope that is comparable to the experimental data points. With rising x_{CO2}, the Peng-Robinson EOS provides a higher pressure than the experiment. Thus the critical pressure of the mixture calculated with the Peng-Robinson EOS is about 12 % higher than the critical pressure estimated on basis of the experimental data for 333 K and about 19 % higher for 353 K. This behavior near the critical line is typical for the Peng-Robinson EOS using the quadratic mixing rule, cf. e.g. the system nitrogen + acetone, which is discussed in Section 6.

9.4 Conclusion

New experimental data for the saturated liquid line of CO_2 + 2,2-dimethyl-1-propanol at the two isotherms 333.2 and 353.2 K up to a pressure of 12.8 MPa were presented. With these data the gap in the literature database for the binary mixtures CO_2 + low molar mass alcohols was closed. The measurements were carried out with a synthetic method using an experimental setup, which allows to load the measurement cell with solid 2,2-dimethyl-1-propanol.
The course of the measured saturated liquid line of CO_2 + 2,2-dimethyl-1-propanol agrees with the behavior of other mixtures of the group CO_2 + low molar mass alcohols. In addition, the Peng-Robinson EOS was adjusted to the present experimental data points. Hereby, the quadratic mixing rule was used.

10 Hydrazine and its derivatives

Hydrazines have a wide variety of applications. Along with their use as high-energy propellants in thrusters for rockets, satellites and space shuttles, they also have a number of commercial applications, including their role as essential building blocks in the synthesis of various polymers, pesticides, pharmaceuticals and chemotherapeutic agents. Furthermore, they are used as explosives to military fuel cells, in metal finishing (nickel plating), in boiler water-feed deoxygenation, in photographic development etc. [111–114].

Due to the safety issues associated with the handling of hydrazine and its derivatives, molecular modeling and simulation can play a particularly important role for the investigation of the thermodynamic properties of these fluids. However, classical molecular simulations, comprising MD and MC calculations, are still uncommon for hydrazine and its derivatives in the scientific literature, especially for the description of VLE of these fluids. On the other hand, few force field parameters and models have recently been published for these chemicals [112, 115]. The force field developed by Borodin [115] accurately describes the thermodynamic and transport properties of hydrazine and its derivatives in one liquid state. Unfortunately, no validation against VLE data has been done, being much more difficult. A force field recently developed by Gutowski *et al.* [112] was validated against experimental saturated densities, vapor pressure, Enthalpy of vaporization, isobaric heat capacity and self-diffusion coefficient. While it yields satisfactory results for the saturated liquid density and the Enthalpy of vaporization, the vapor pressure predicted for hydrazine and its derivatives deviates significantly from experimental data.

In a joint project with the company Lonza AG, Chemical Research and Development, Switzerland, new molecular models for hydrazine (N_2H_4), monomethylhydrazine (CH_3-NH-NH_2) and 1,1-dimethylhydrazine ((CH_3)$_2$-N-NH_2) were developed. The parameterization of the molecular interaction models for these pure substances was carried out on the basis of the QC calculations, followed by optimizations to experimental data on saturated liquid density and vapor pressure. The molecular interaction models were then used to predict important thermodynamic properties and to study the fluid phase behavior. Thereby, a large set of experimental thermodynamic data for pure hydrazines and binary hydrazine mixtures was considered for comparison with the present molecular simulation data.

10.1 Molecular models

All molecules studied in the present work do not exhibit significant conformational changes. Hence their internal degrees of freedom were neglected and the molecular models were chosen to be rigid. In a first step, the geometric data of the molecules, i.e. bond lengths, angles and dihedrals, were determined by QC calculations. Therefore, a geometry optimization was performed via an energy minimization using the GAMESS (US) package [56]. The Hartree-Fock level of theory was applied with a relatively small (6-31G) basis set.

10.1.1 Hydrazine

The present hydrazine (N_2H_4) model consists of two LJ sites, located at the positions of the nitrogen atoms, plus six point charges, i.e. one for every atom, cf. Figure 48. All LJ parameters and the charge magnitudes were initially taken from the monomethylamine model of Schnabel et al. [23]. During the model parameter optimization to vapor pressure and saturated liquid density, the distance between two atoms of nitrogen as determined by QC (1.414 Å) was slightly reduced, leading to a distance of 1.4 Å and the point charge magnitudes were adjusted. Finally, the reduced unit method [116] for fine-tuning the model parameters to the experimental VLE data was used, leading to a slight modification of all model parameter values. The full parameter set of the new hydrazine model is listed in Table 8.

It should be noted that the final geometric and electrostatic model parameter values correspond well with the theoretical results recently presented by Kaczmarek *et al.* [117]. In Ref. [117], structural and electronic properties of the hydrazine molecule were studied by a series of classical and quantum ab initio simulations at room temperature. Therefore, time-

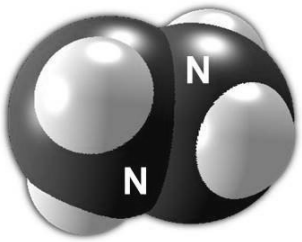

Figure 48: Present molecular force field model for hydrazine. N: nitrogen Lennard-Jones site, not labeled: hydrogen Lennard-Jones site. Note that the nitrogen sphere diameters correspond to the Lennard-Jones size parameters, which are depicted according the molecular geometry scale.

average statistical analyses of ab initio MD and ab initio path integral MD simulations of hydrazine were carried out [117]. The values of the normalized distribution functions, corresponding to the present optimized structural molecular model parameters, lie close to the respective normal distribution maximum. The dipole moment magnitude calculated for the present molecular model is about 2.25 D and agrees well with the static equilibrium value of about 2.22 D by Kaczmarek *et al.* [117]. However, both dipole moments are above the experimental value of 1.85 D reported by Seddon *et al.* [118].

10.1.2 Monomethylhydrazine

The intermolecular interactions of monomethylhydrazine (CH_3-NH-NH_2) were described by three LJ sites, i.e. one for every atomic group, cf. Figure 49. In addition, three point charges were located at the positions of the hydrogen atoms and the nitrogen atom of the NH_2 group. The LJ parameters of the NH_2 and NH groups and the charge magnitudes of the NH_2 group were taken from the present hydrazine model. The LJ parameters of the CH_3 group were taken from the ethanol (and monomethylamine) model by Schnabel *et al.* [23, 119].

During the model parameter optimization to vapor pressure and saturated liquid density, the distance between the CH_3 group and the NH group was increased, leading to a distance of 1.7 Å which is larger than the one determined by QC (1.458 Å) and the experimental value of 1.47 Å from Schmidt [113]. The full parameter set of the molecular monomethylhydrazine model is listed in Table 8.

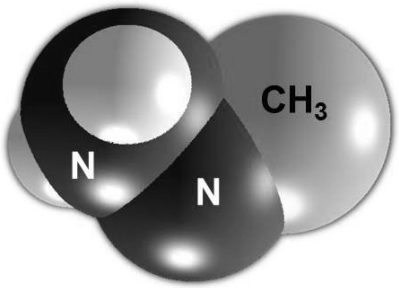

Figure 49: Present molecular force field model for monomethylhydrazine. CH_3: methyl Lennard-Jones site, N: nitrogen Lennard-Jones site, not labeled: hydrogen Lennard-Jones site. Note that the nitrogen and methyl sphere diameters correspond to the Lennard-Jones size parameters, which are depicted according the molecular geometry scale.

10.1.3 Dimethylhydrazine

The present molecular model for 1,1-dimethylhydrazine ($(CH_3)_2$-N-NH_2) is based on the hydrazine and monomethylhydrazine models described above, cf. Figure 50. This model consists of four LJ sites, i.e. one for every atomic group, plus three point charges, located at the positions of the hydrogen atoms and the nitrogen atom of the NH_2 group, like in case of the monomethylhydrazine model. The LJ parameters and the charge magnitudes for the NH_2 group were taken from the hydrazine model. The LJ parameters for the nitrogen atom were taken from a nitrogen model developed earlier [47], the LJ parameters for the CH_3 group were taken from the ethanol (and monomethylamine) model by Schnabel *et al.* [23, 119].

In case of the dimethylhydrazine model, only the geometry parameters, initially determined by QC, were optimized to the experimental homogeneous liquid density. For this, the distances between the nitrogen atom and the CH_3 groups were adjusted, leading to a distance of 1.59 Å, which is somewhat larger than the distance determined by QC (1.46 Å) and than the experimental value of 1.47 ± 0.03 Å by Beamer [113, 120]. The full parameter set of the new molecular dimethylhydrazine model is listed in Table 8.

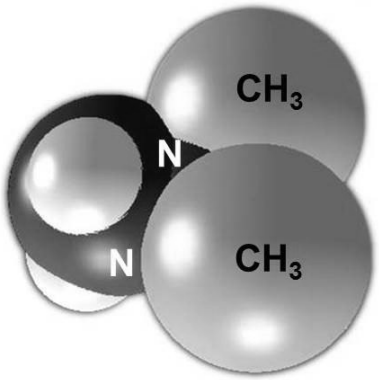

Figure 50: Present molecular force field model for dimethylhydrazine. CH_3: methyl Lennard-Jones site, N: nitrogen Lennard-Jones site, not labeled: hydrogen Lennard-Jones site. Note that the sphere diameters correspond to the Lennard-Jones size parameters, which are depicted according the molecular geometry scale.

Table 8: Parameters of the molecular models for hydrazine, monomethylhydrazine and dimethylhydrazine developed in this work. LJ interaction sites are denoted by the modeled atomic groups. Electrostatic interaction sites are denoted by point charge. Coordinates are given with respect to the center of mass in a principal axes system.

interaction site	x Å	y Å	z Å	σ Å	ε/k_B K	q e
hydrazine						
NH_2	0.044	-0.062	0.705	3.3523	146.41	
NH_2	0.044	0.062	-0.705	3.3523	146.41	
point charge (N)	0.044	-0.062	0.705			-0.6616
point charge (H1)	0.271	0.869	1.076			0.3308
point charge (H2)	-0.892	-0.307	1.062			0.3308
point charge (N)	0.044	0.062	-0.705			-0.6616
point charge (H1)	-0.893	0.305	-1.062			0.3308
point charge (H2)	0.274	-0.869	-1.076			0.3308
monomethylhydrazine						
CH_3	-0.025	-0.302	1.477	3.6072	120.15	
NH	0.043	0.597	0.036	3.3587	147.83	
NH_2	-0.057	-0.305	-1.075	3.3587	147.83	
point charge (N)	-0.057	-0.305	-1.075			-0.6654
point charge (H1)	0.856	-0.705	-1.308			0.3327
point charge (H2)	-0.361	0.244	-1.875			0.3327
dimethylhydrazine						
CH_3	-0.155	1.312	0.904	3.6072	120.15	
CH_3	-0.164	-1.316	0.910	3.6072	120.15	
N	0.395	-0.053	0.197	3.3211	34.90	
NH_2	-0.081	0.070	-1.496	3.3085	141.15	
point charge (N)	-0.081	0.070	-1.496			-0.6882
point charge (H1)	0.497	-0.609	-1.990			0.3441
point charge (H2)	-1.056	-0.251	-1.590			0.3441

10.1.4 Other pure fluids

The present work is devoted to the development and assessment of molecular models for hydrazine and its two most important methylized derivatives. Apart from VLE and homogeneous liquid data for the pure hydrazines, the majority of the publicly available experimental data for binary mixtures containing hydrazines were used to validate the new molecular models. Binary hydrazine mixtures with the following components were simulated: argon (Ar),

nitrogen (N_2), carbon monoxide (CO), ammonia (NH_3) and water (H_2O). The molecular models used in this work for these compounds are briefly described in the following.

Molecular models for argon, nitrogen and carbon monoxide, used here to calculate the Henry's law constant in liquid hydrazine, monomethylhydrazine and dimethylhydrazine, were taken from Vrabec *et al.* [47] (Ar and N_2) and Stoll *et al.* [121] (CO). These are a spherical non-polar one-center LJ model for Ar, an elongated dipolar two-center LJ (2CLJD) model for CO and an elongated quadrupolar two-center LJ (2CLJQ) model for N_2. These models describe the VLE with an accuracy of about 0.5 % for the saturated liquid density, 3-4 % for the vapor pressure and 2-3 % for the enthalpy of vaporization over the whole temperature range from the triple point to the critical point [47, 121].

The molecular model for ammonia, used here to calculate VLE of binary mixtures with all three studied hydrazines, was taken from Eckl *et al.* [62]. It consists of a single LJ site for the dispersive and repulsive interactions. The electrostatic interactions as well as hydrogen bonding were modeled by a total of four superimposed partial charges. The model by Eckl *et al.* [62] shows mean unsigned deviations to experimental data of 0.7 % for the saturated liquid density, 1.6 % for the vapor pressure and 2.7 % for the enthalpy of vaporization over the whole temperature range from the triple point to the critical point [62].

The employed water model is based on the rigid four-site TIP4P model type, initially proposed by Jorgensen *et al.* [122]. This model type consists of three point charges, eccentrically superimposed to a single LJ site. The TIP4P model type was parametrized by many authors [123]. Here, the interaction parameters by Huang *et al.* [124, 125] were used. In comparison with alternative parameterizations from the literature [122, 126–129], this model better represents the VLE properties, if the whole temperature range is considered. The model by Huang *et al.* [124, 125] yields mean unsigned errors for vapor pressure, saturated liquid density and enthalpy of vaporization of 7.2, 1.1 and 2.8 %, respectively, in the temperature range from 300 to 600 K, which is about 46 to 93 % of the critical temperature [125].

10.1.5 Simulation results for the pure fluids

Hydrazine

The results for saturated densities, vapor pressure and Enthalpy of vaporization obtained with the present model are compared with the available experimental data [30, 60, 112] and to the simulation results by Gutowski *et al.* [112] in Figures 51 to 55. The present data are given in numerical form in the appendix. While the model by Gutowski *et al.* [112] covers

the saturated liquid density well only at lower temperatures, deviating from experimental data by +0.2 % at 298 K to -5.1 % at 450 K [112], the present model is excellent in the whole temperature range for this property, yielding a mean unsigned error of about 0.5 %, cf. Figure 51. Gutowski *et al.* [112] overestimated the vapor pressure by more than 130 % at 450 K, while the average deviation for the present model is about 7.6 %, cf. Figures 52 and 53. Gutowski *et al.* [112] did not calculate VLE data above 450 K, but it can be seen from the temperature trend that the deviations would increase there. Both models were also validated against the enthalpy of vaporization. The model by Gutowski *et al.* [112] exhibits a minimum difference between experiment and simulation of 1.6 kJ/mol at 298.15 K, which is about 3.5 %, however, the deviations again increase significantly with increasing temperature, cf. Figure 54. The results obtained with the present model overestimate the available experimental data on average by about 2.3 %. The critical values of temperature, density

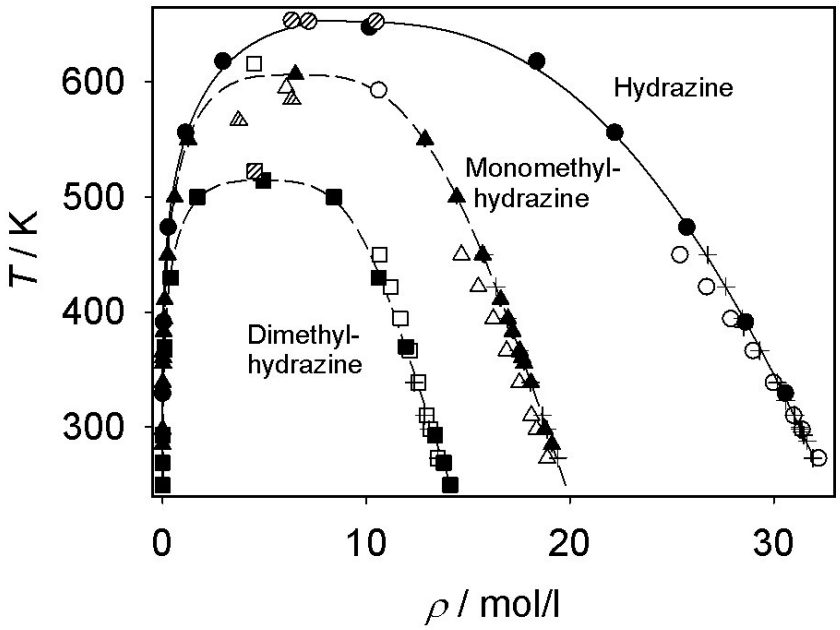

Figure 51: Saturated densities of hydrazine (●), monomethylhydrazine (▲) and dimethylhydrazine (■): (striped symbols) experimental critical point [30, 60, 112, 130]; (+) experimental data [30, 60]; simulation data: (solid symbols) this work, (empty symbols) Gutowski *et al.* [112] (saturated liquid only); (——) correlation of experimental data [60]; (- - -) correlation of present simulation data [135]. The statistical uncertainties of the present simulation data are within symbol size.

and pressure were calculated from the present simulation data with a method suggested by Lotfi *et al.* [61]. The obtained values are listed in Table 9. The simulated critical data for temperature and pressure of 647.6 K and 13.04 MPa are in good agreement with the experimental values of 653.00 K and 14.69 MPa from the DDB [30] and with the experimental values of 653.15 K and 14.69 MPa from the DIPPR [60] and the Merseburger Datenbank (MDB) [130]. The critical density from the present simulations is 10.16 mol/l, while the experimental value for this property is about 6.33 mol/l according to the DIPPR and MDB, 7.18 mol/l according to experimental data by Haws and Harden [131] and 10.41 mol/l according to the DDB. It should be noted that the critical constants of hydrazine are very difficult to determine experimentally, because of the tendency of hydrazine to undergo decomposition at higher temperatures [113, 132]. By visual inspection of Figure 51 it can be inferred that the critical density reported in the DIPPR and MDB as well as the experimental critical value by Haws and Harden [131] does not correspond well with the experimental data on the saturated liquid line. Gutowski *et al.* [112] predicted a critical temperature and density of 593 K and 10.61 mol/l.

Table 9: Critical properties on the basis of the present molecular models in comparison to experimental data.

substance	T_c^{sim} K	T_c^{exp} K	ρ_c^{sim} mol/l	ρ_c^{exp} mol/l	p_c^{sim} MPa	p_c^{exp} MPa	exp. Ref.
hydrazine	647.6	653	10.16	10.41	13.04	14.69	[30]
hydrazine	647.6	653.15	10.16	6.33	13.04	14.69	[60, 130]
hydrazine	647.6	653	10.16	7.18	13.04	14.69	[113, 131, 132]
monomethyl-hydrazine	606.6	567	6.53	3.69	7.66	8.04	[30]
monomethyl-hydrazine	606.6	567	6.53	3.69	7.66	8.24	[130]
monomethyl-hydrazine	606.6	585	6.53	6.29	7.66	8.21	[113]
dimethyl-hydrazine	514.5	523	4.95	4.58	5.00	5.40	[113]

Figure 55 presents the isobaric heat capacity of hydrazine in the homogeneous liquid at ambient pressure. Note that only the residual isobaric heat capacity $c_p^r(T,p)$ was calculated here by molecular simulation. To obtain the total isobaric heat capacity c_p, the solely temperature dependent ideal gas contribution $c_p^0(T)$ from the DIPPR database [60] was added $c_p(T,p) = c_p^0(T) + c_p^{res}(T,p)$. The isobaric heat capacity from the model by Gutowski *et al.* [112] is in reasonable agreement with the experiment (10 % deviation), while the difference between experiment and simulation is about 17% for the present model.

Figure 56 compares the simulation results with experimental data on the homogeneous density of liquid hydrazine at 0.1013 MPa. The achieved agreement over a temperature range of about 150 K is excellent, yielding a mean unsigned error of only about 0.05%.

For hydrazine, data on the second virial coefficient from the DIPPR database [60] are available for comparison with the simulation results. There are two different datasets: approximate values by Drago and Sisler [133] and values estimated with the method by Tsonopoulos [60, 134]. The DIPPR correlation is based on the estimated values, cf. Figure 57. The present simulation results agree well with the estimated data [60, 134], only at low temperatures some noticeable deviations are present, yielding a mean error of about 0.11 l/mol. The approximate second virial coefficient data between 363 and 393 K by Drago and Sisler [133] are between +2.14 and +4.20 l/mol (far out of scale in Figure 57) and seem to be wrong. Figure 58 compares the predictions based on the present molecular model with the experimental data on the shear viscosity that are available in DDB [30]. The results obtained with the present model overestimate the experimental shear viscosity data by about 64 %.

Monomethylhydrazine

The results for saturated densities, vapor pressure and Enthalpy of vaporization are compared with the available experimental data [30, 60, 112] and to the simulation results by Gutowski *et al.* [112] in Figures 51 to 55. The present data are given in numerical form in the appendix. The present model describes the vapor pressure and the saturated densities much better than the model by Gutowski *et al.* [112], which underestimates the experimental saturated liquid density from 2.8 % at 273 K to 7.7 % at 450 K [112]. These deviations are minor for the present model, yielding a mean unsigned error of about 0.2 % over the entire temperature range, cf. Figure 51. The vapor pressure by Gutowski *et al.* [112] is on average by 54% below the experimental data, while the average deviation for the present model is about 7.0 %, cf. Figures 52 and 53. The enthalpy of vaporization deviates from the experimental data for both molecular models, cf. Figure 54. The simulation results by Gutowski *et al.* [112] are higher than the experimental data by about 6.7 % and also show a significant scatter,

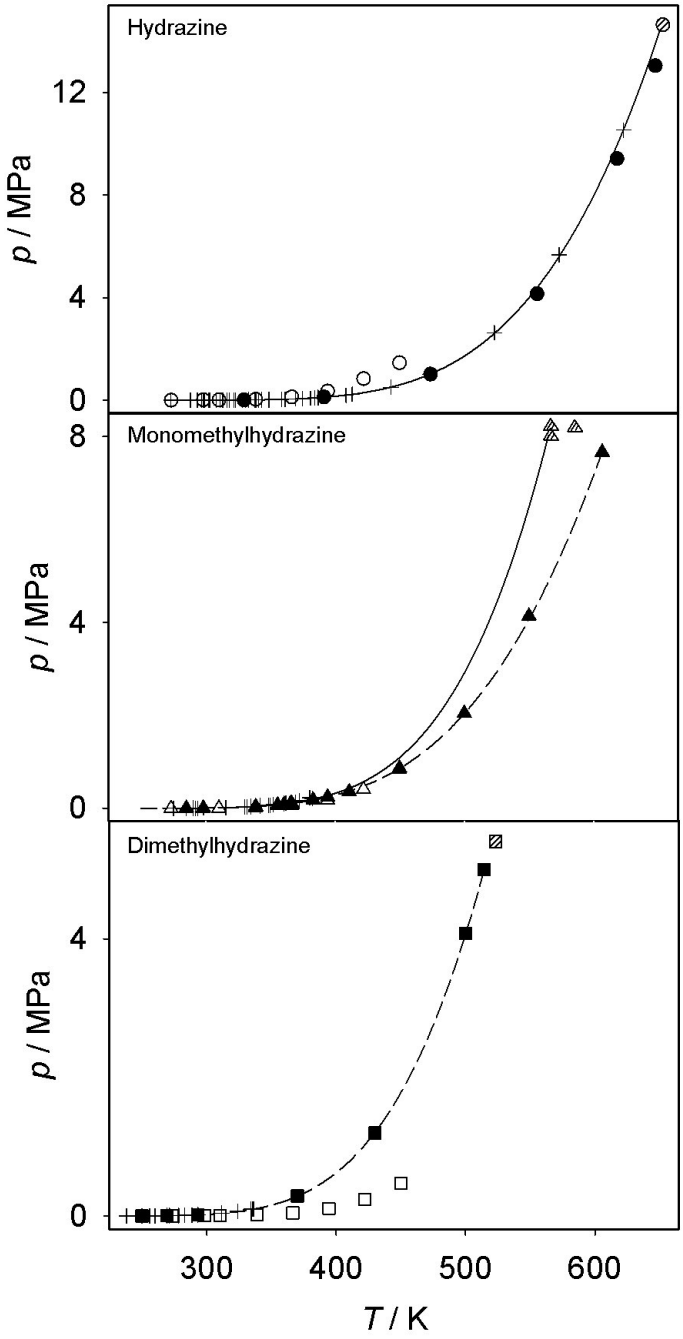

Figure 52: Vapor pressure of hydrazine (●), monomethylhydrazine (▲) and dimethylhydrazine (■): (striped symbols) experimental critical point [30, 60, 130]; (+) experimental data [30]; simulation data: (solid symbols) this work, (empty symbols) Gutowski *et al.* [112]; (——) correlation of experimental data [60, 130]; (- - -) correlation of present simulation data [135]. The statistical uncertainties of the present simulation data are within symbol size.

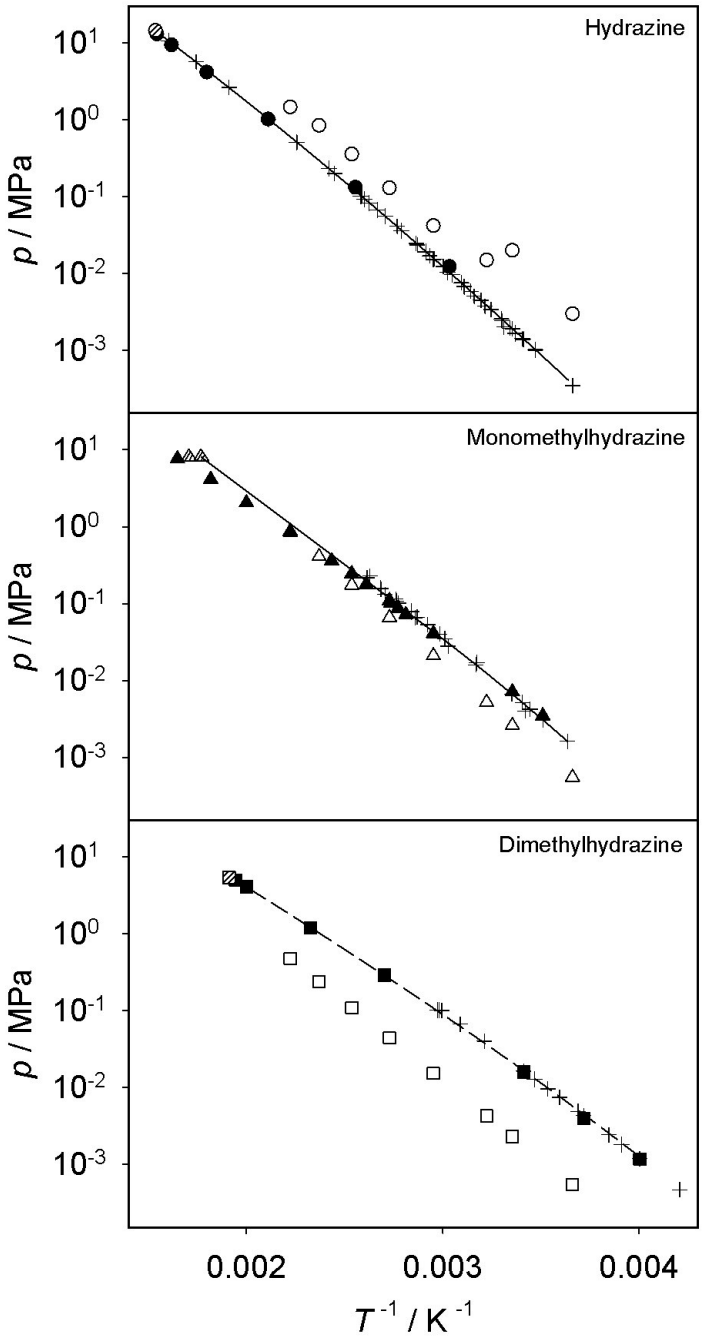

Figure 53: Logarithmic vapor pressure of hydrazine (●), monomethylhydrazine (▲) and dimethylhydrazine (■): (striped symbols) experimental critical data [30, 60, 130]; (+) experimental data [30]; simulation data: (solid symbols) this work, (empty symbols) Gutowski *et al.* [112]; (——) correlation of experimental data [130]; (- - -) correlation of present simulation data [135]. The statistical uncertainties of the present simulation data are within symbol size.

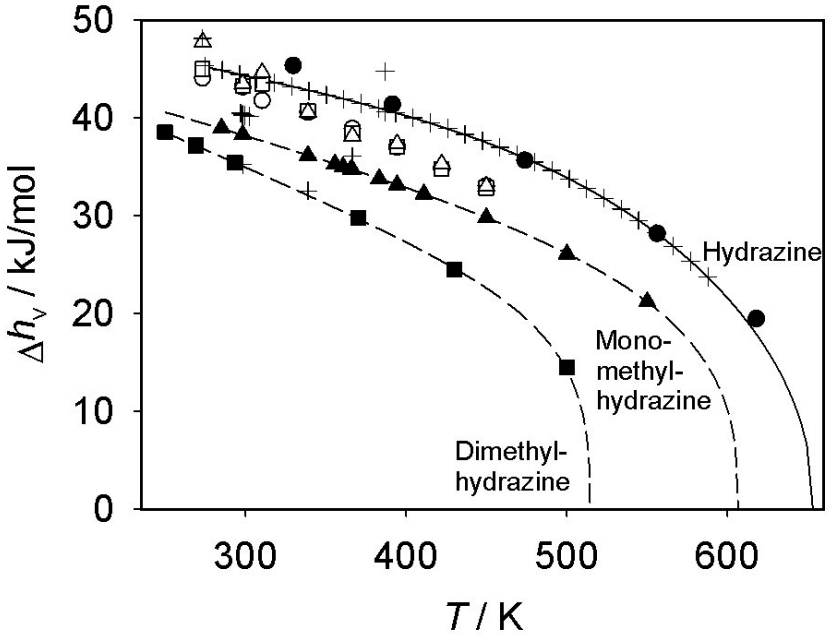

Figure 54: Enthalpy of vaporization of hydrazine (●), monomethylhydrazine (▲) and dimethylhydrazine (■): (+) experimental data [30]; simulation data: (solid symbols) this work, (empty symbols) Gutowski *et al.* [112]; (——) correlation of experimental data [60]; (- - -) correlation of present simulation data [135]. The statistical uncertainties of the present simulation data are within symbol size.

cf. Figure 54. The results obtained with the present model underestimate the available experimental enthalpy of vaporization data by about 5.1 %.

The critical values of temperature, density and pressure predicted with the present model using the method by Lotfi *et al.* [61] are given in Table 9. The critical temperature of 606.6 K is by almost 22 K higher than the experimental value by Schmidt [113] and by almost 40 K higher than the experimental value from the DDB and MDB databases [30, 130]. The present critical density is 6.53 mol/l, while the experimental value for this property is only about 3.69 mol/l according to the DDB and MDB and 6.29 mol/l according to experimental data by Schmidt [113]. The present critical pressure of 7.66 MPa is in good agreement with the experimental values of 8.04, 8.24 and 8.21 MPa from the DDB and MDB databases and by Schmidt [113], respectively. In this case, the critical temperature of 595 K and the critical density of 6.07 mol/l predicted by Gutowski *et al.* [112] are slightly closer to the experimental data.

The isobaric heat capacity of the homogeneous liquid at ambient pressure from simulation is

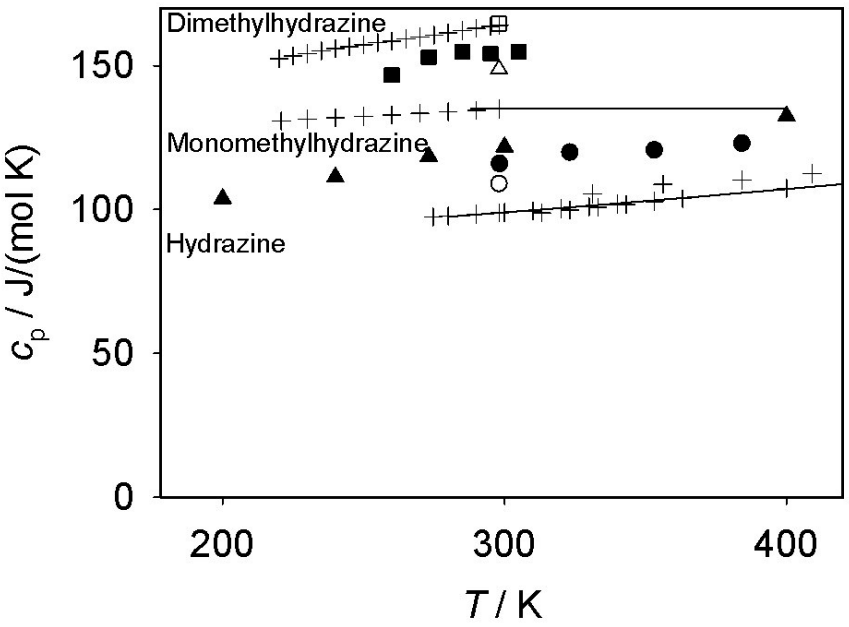

Figure 55: Isobaric heat capacity of liquid hydrazine (●), monomethylhydrazine (▲) and dimethylhydrazine (■) at 0.1013 MPa: (+) experimental data [30, 60, 136]; simulation data: (solid symbols) this work, (empty symbols) Gutowski *et al.* [112]; (—) correlations of experimental data [60, 130]. The statistical uncertainties of the present simulation data are within symbol size.

in reasonable agreement with the experimental data for both models. The average deviation is 9.7 % for the model by Gutowski *et al.* [112] and -8.8 % for the present model, cf. Figure 55.

Figure 57 shows the second virial coefficient predicted with the present model. Unfortunately, no other data were available for comparison.

Dimethylhydrazine

The results for saturated densities, vapor pressure and Enthalpy of vaporization are compared with the available experimental data [30, 60, 112] and to the simulation results by Gutowski *et al.* [112] in Figures 51 to 55. The present data are given in numerical form in the appendix. The saturated liquid density based on the model by Gutowski *et al.* [112] follows an opposite trend relative to hydrazine and monometylhydrazine, i.e. the density from simulation is larger than that from experiment [112]. Over the temperature range from 273 to 339 K, the values by Gutowski are in excellent agreement with the experiment, being only slightly

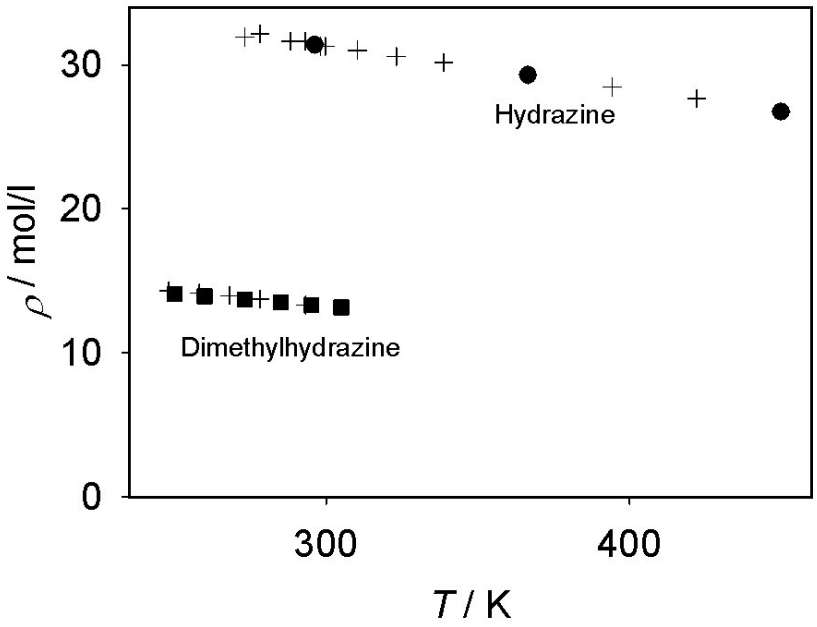

Figure 56: Density of liquid hydrazine (●) and dimethylhydrazine (■) at 0.1013 MPa: (+) experimental data [30]; (solid symbols) simulation data, this work. The statistical uncertainties of the present simulation data are within symbol size.

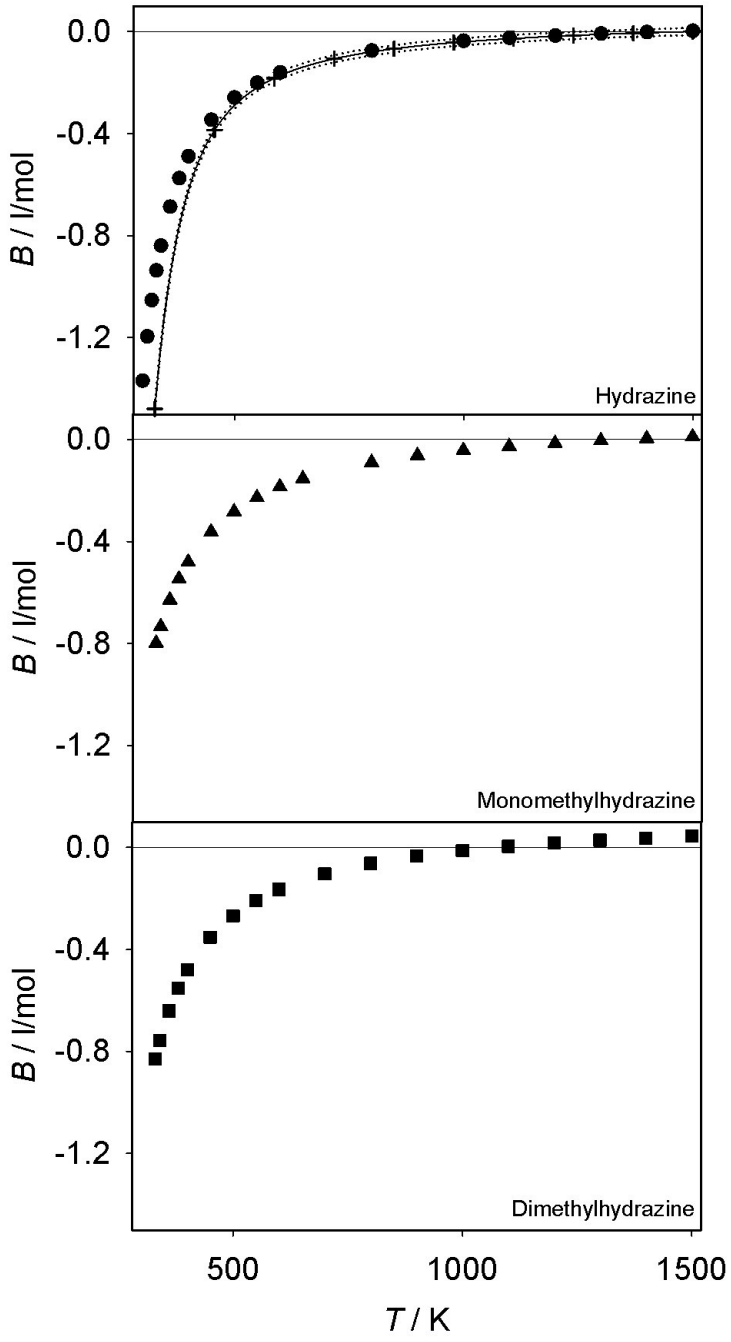

Figure 57: Second virial coefficient of hydrazine (●), monomethylhydrazine (▲) and dimethylhydrazine (■): (solid symbols) simulation data, this work; (+) second virial coefficients estimated with the method by Tsonopoulos [60, 134]; (——) correlation of estimated data [60, 134]; (· · ·) uncertainty of the correlation.

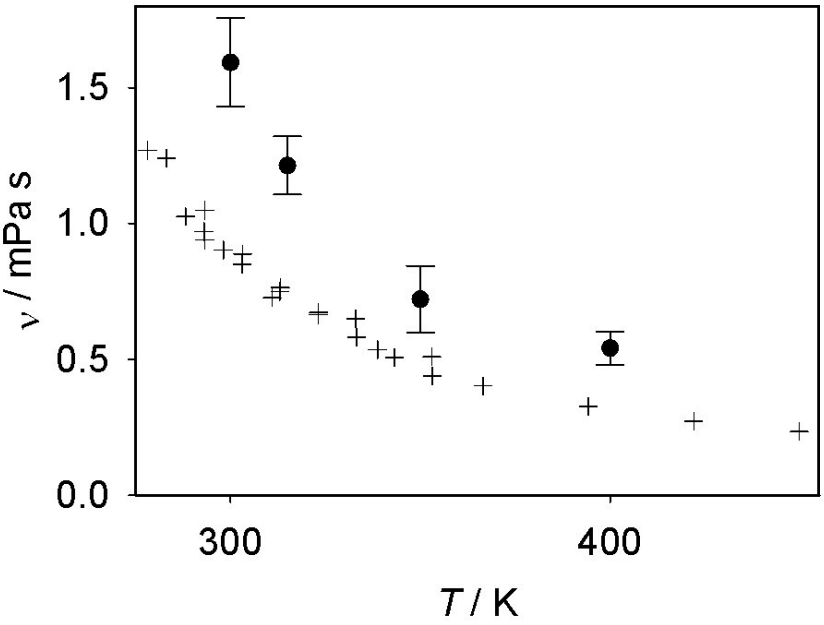

Figure 58: Shear viscosity of liquid hydrazine at 0.1013 MPa: (+) experimental data [30]; (●) simulation data, this work.

higher (0.5 to 1.7 %) [112]. At higher temperatures the deviations are increasing. For the present model, the average deviation from the experimental saturated liquid density is about 1.3 % over the whole temperature range. In case of the vapor pressure, the present model yields very good results, deviating from the experiment only by about 3.7 %, while the values by Gutowski *et al.* [112] underestimate the experimental vapor pressure by more than 80 % above 340 K.

The critical properties were determined through fits to the present VLE simulation results as suggested by Lotfi *et al.* [61]. Table 9 compares these properties to the experimental data from Schmidt [113]. The present critical data for temperature and density of 514.46 K and 4.95 mol/l are in good agreement with the experimental values of 523 K and 4.58 mol/l, while Gutowski *et al.* [112] predicted a critical temperature of 616 K, which is too high by more than 90 K, and a critical density of 4.49 mol/l. The present critical pressure of 5.0 MPa is in very good agreement with the experimental value of 5.4 MPa reported by Schmidt [113].

The enthalpy of vaporization presented by Gutowski *et al.* [112] at 298 and 339 K is higher than the experimental values by around 8 kJ/mol, which is 24% in relative terms. For the present model, these deviations are minor, yielding a mean unsigned error of about 1.0 %, cf. Figure 54. It should be noted that Gutowski *et al.* [112] predicted enthalpy of vaporization data which are only little dependent on the type of hydrazine, cf. Figure 54. This finding

is contradictory to the available experimental data. On the other hand, the homogeneous liquid isobaric heat capacity of dimethylhydrazine by Gutowski *et al.* [112] is in excellent agreement with the experiment [136], differing by only 0.4 %, while the deviation for the present model is about 5.9 %, cf. Figure 55.

Figure 56 compares the present simulation results with experimental data on the density of homogeneous liquid dimethylhydrazine at ambient pressure. The achieved agreement is good, yielding a mean unsigned error of about 1.1%.

Figure 57 shows the second virial coefficient predicted with the present model. Unfortunately, no other data were available for comparison.

10.2 Mixtures containing hydrazines

Based on the discussed three molecular hydrazine models, VLE data were predicted for all three binary combinations with water as well as for the mixture dimethylhydrazine + hydrazine. Also all binary combinations of the three hydrazines with ammonia at different temperatures were simulated. This choice was driven by the availability of experimental VLE data. Present simulation data for all mixtures are given in numerical form in the appendix. Please note that the appendix also contains the saturated densities and the Enthalpy of vaporization for all regarded mixtures. These data are not further discussed here, because of the lack of experimental data for comparison. For orientation and comparison, the results of the Peng-Robinson equation of state (EOS) [5] with one adjusted binary parameter k_{ij} of the quadratic mixing rule are also presented. Generally, the EOS was optimized to the experimental vapor pressure at the same state point as the molecular mixture model.

10.2.1 Water + hydrazine

For most uses, hydrazine is produced as hydrazine hydrate in a formulation with water [113, 137]. Hydrazine hydrate, or simply the aqueous solution of hydrazine, finds use in water treatment as oxygen scavenger in high pressure boilers and in the synthesis of various chemicals and bulk drugs. Anhydrous hydrazine is the formulation used for rocket fuels and is produced by dehydration of the hydrate via azeotropic distillation with e.g. aniline as an auxiliary fluid [137]. Thus, the knowledge of the VLE properties of this mixture plays an important role for numerous industrial applications.

Figure 59 shows the isobaric VLE of water + hydrazine at 0.1013 MPa from experiment

[30, 138, 139], simulation and Peng-Robinson EOS. The mixture is azeotropic, having a temperature maximum. The azeotropic point is at $x_{H2O} \approx 0.41$ mol/mol. It should be noted that the experimental data by Uchida *et al.* [138] and by Lobry de Bruyn and Dito [139] differ somewhat from each other, especially near the azeotropic region, where the data by Lobry de Bruyn and Dito [139] lie above the data by Uchida *et al.* [138]. In the water-rich region, these data have a reverse order. The experimental vapor pressure by Uchida *et al.* [138] at 388.25 K and $x_{H2O} = 0.6925$ mol/mol was taken to adjust the binary parameter of the molecular model ($\xi = 1.3$) and of the Peng-Robinson EOS ($k_{ij} = -0.1325$). Considering the substantial experimental uncertainties, the data sets from all three approaches agree very favorably.

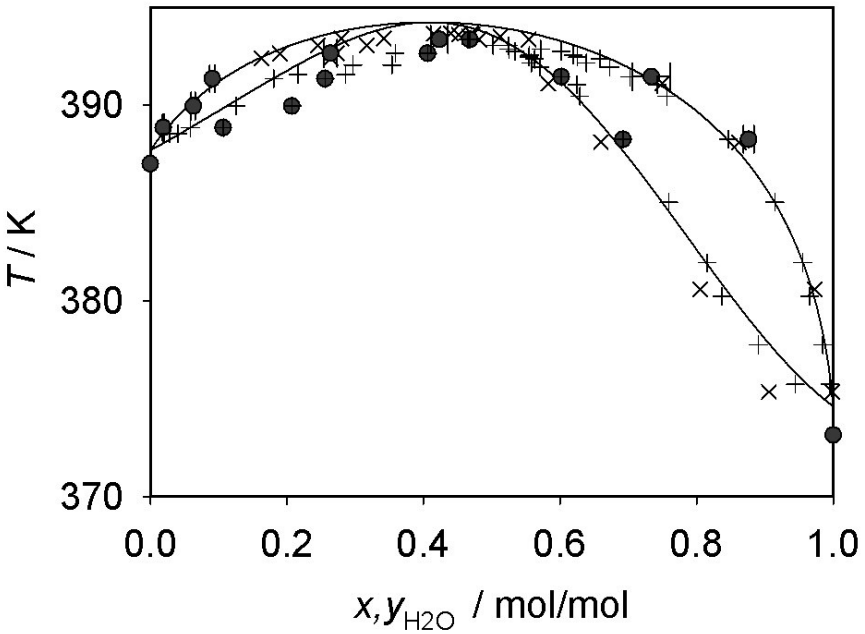

Figure 59: Isobaric vapor-liquid phase diagram of water + hydrazine at 0.1013 MPa: experimental data: (×) Lobry de Bruyn and Dito [139], (+) Uchida *et al.* [138]; (●) simulation data, this work (ξ=1.3); (——) Peng-Robinson EOS (k_{ij}=−0.1325).

10.2.2 Monomethylhydrazine + water

Monomethylhydrazine as a pure fluid is used as a propellant for launching rockets and satellites. It has also many other important applications, such as oxygen scavenger for boiler

feedwater, starting material for dye intermediates, catalysis for polymerization reactions etc. [140]. To recover monomethylhydrazine from aqueous solutions in order to obtain propellant grade material, VLE data of its aqueous mixture are needed.

Figure 60 depicts the VLE of monomethylhydrazine + water at ambient pressure. It can be seen that the experimental data by Ferriol *et al.* [141] and by Cohen-Adad *et al.* [142] are quite similar, however, they differ near the azeotropic region. Like aqueous hydrazine, this mixture is azeotropic, having a temperature maximum. In this case, the azeotropic point lies at $x_{\mathrm{CH3-N2H3}} \approx 0.25$ mol/mol. The experimental data by Ferriol *et al.* [141] at 372.55 K and $x_{\mathrm{CH3-N2H3}} = 0.476$ mol/mol were taken to adjust the binary parameter of the molecular model ($\xi = 1.3$) and of the Peng-Robinson EOS ($k_{ij} = -0.197$). In the water-rich region, to the left of the azeotropic point in Figure 60, VLE simulations were not feasible, because of sampling problems. Considering the substantial experimental uncertainties, the data sets from all three approaches agree very favorably.

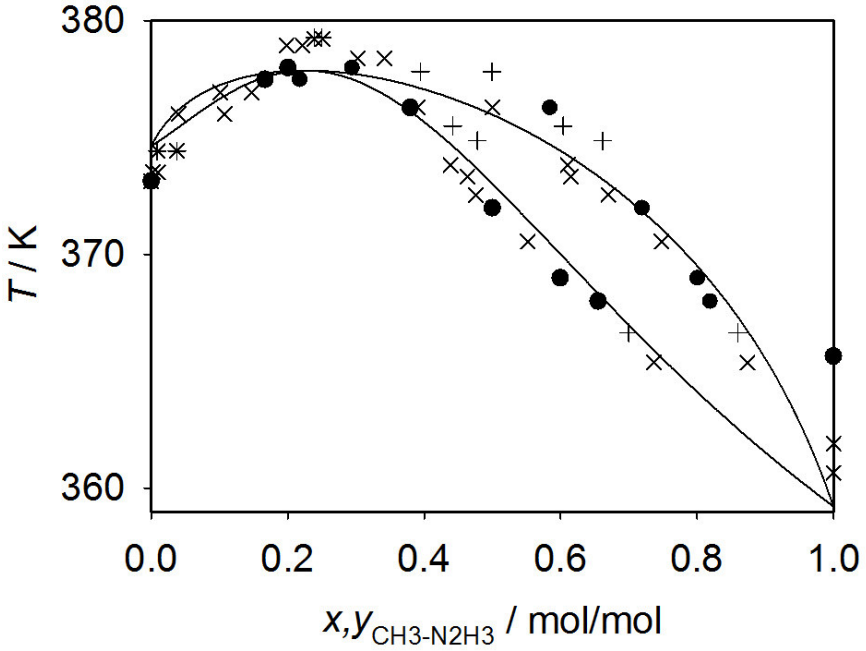

Figure 60: Isobaric vapor-liquid phase diagram of monomethylhydrazine + water at 0.1013 MPa: experimental data: (×) Ferriol *et al.* [141], (+) Cohen-Adad *et al.* [142]; (●) simulation data, this work (ξ=1.3); (——) Peng-Robinson EOS (k_{ij}=−0.197).

10.2.3 Dimethylhydrazine + water

Dimethylhydrazine is primarily used as a component of jet and rocket fuels. Other applications include it as an intermediate for chemical synthesis, as a stabilizer for organic peroxide fuel additives, as an absorbent for acid gases or as a plant growth control agent [143]. In the production of dimethylhydrazine, aqueous solutions, containing usually 10 % to 40 % of dimethylhydrazine, are initially obtained. The design of distillation processes for separating dimethylhydrazine from aqueous solutions requires VLE data for the binary system dimethylhydrazine + water [144]. Figure 61 shows the isobaric VLE of dimethylhydrazine + water at 0.1013 MPa from experiment, simulation and Peng-Robinson EOS. In contrast to the the previous two binary systems, this mixture is zeotropic. The experimental data by Carleton [144] and by Ferriol *et al.* [141] are very similar, however, the phase envelope reported by Carleton [144] is a little wider. The experimental vapor pressure by Ferriol *et al.* [141] at 345.17 K and $x_{(CH3)2-N2H2} = 0.571$ mol/mol was taken to adjust the binary parameter of the molecular model ($\xi = 1.3$) and of the Peng-Robinson EOS ($k_{ij} = -0.285$) [5]. It can be seen in the Figure 61 that the results obtained by molecular simulation agree well with the experimental results on the saturated liquid line, but overestimate the dimethylhydrazine content on the saturated vapor line for intermediate compositions. In the water-rich region and in the dimethylhydrazine-rich region, the narrow two-phase envelope is well predicted by simulation, whereas the Peng-Robinson EOS yields a qualitatively different form.

10.2.4 Dimethylhydrazine + hydrazine

Different mixtures of hydrazine and dimethylhydrazine, e.g. known as Aerozine 50 or UH25, are in wide use as rocket fuels [145]. Such mixtures are more stable than pure hydrazine and have a higher density and boiling point than pure dimethylhydrazine. The thermodynamic properties of such mixtures are of major importance for research, development and design efforts concerning their use as propellants or hydraulic working fluids in space propulsion systems [145].

The VLE of dimethylhydrazine + hydrazine is presented in Figure 62 at ambient pressure. This system is zeotropic. The experimental vapor pressure by Pannetier and Mignotte [146] at 346.35 K and $x_{(CH3)2-N2H2} = 0.4717$ mol/mol was taken to adjust the binary parameter of the molecular model ($\xi = 1.01$) and of the Peng-Robinson EOS ($k_{ij} = -0.1$). It should be noted that the description of the interactions between LJ sites of unlike molecules was in this case very close to the standard Lorentz-Berthelot combining rules. It can be seen that

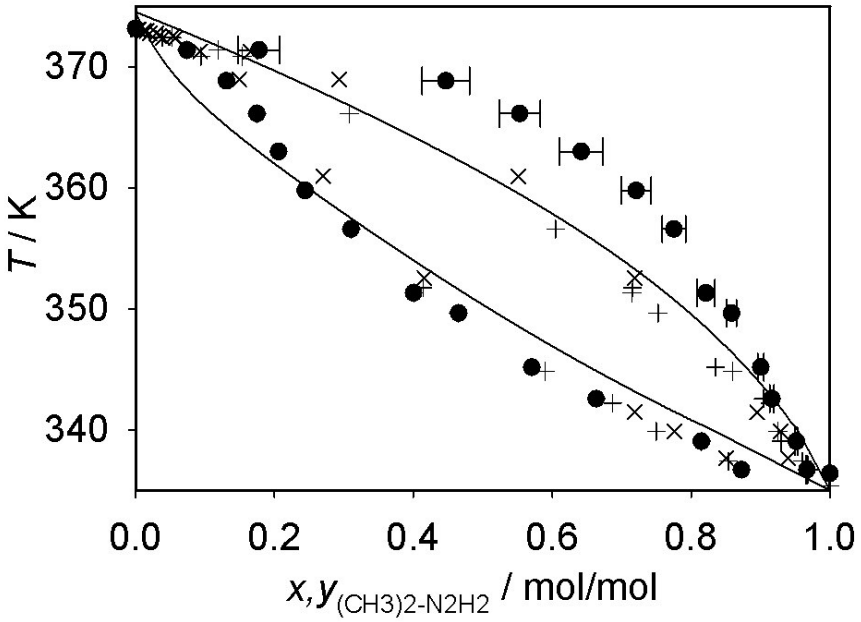

Figure 61: Isobaric vapor-liquid phase diagram of dimethylhydrazine + water at 0.1013 MPa: experimental data: (×) Carleton [144], + Ferriol *et al.* [141]; (●) simulation data, this work (ξ=1.3); (——) Peng-Robinson EOS (k_{ij}=−0.285).

simulation results match almost perfectly with the experimental data on the saturated liquid line. On the saturated vapor line, the experimental data and the simulation results exhibit some scatter, but the agreement is reasonable.

10.2.5 Binary mixtures containing ammonia

The addition of a small amount of ammonia to hydrazine improves its performance in propulsion systems, such as the rocket internal combustion engine [147]. The high octane rating of ammonia allows the compression to be higher than in case of pure hydrazine, which is highly prone to detonation, while hydrazine offsets drawbacks of ammonia, like high ignition point and low burn speed. An accurate investigation of the fluid phase behavior is therefore of interest.

Binary VLE of ammonia with the three hydrazines are presented in Figure 63 for different temperatures. The experimental data by Chang *et al.* [147] at the highest vapor pressure for each system were taken to adjust the binary parameter of the molecular models (ξ = 1.084 for hydrazine, ξ = 1.016 for monomethylhydrazine and ξ = 0.94 for dimethylhydrazine) and

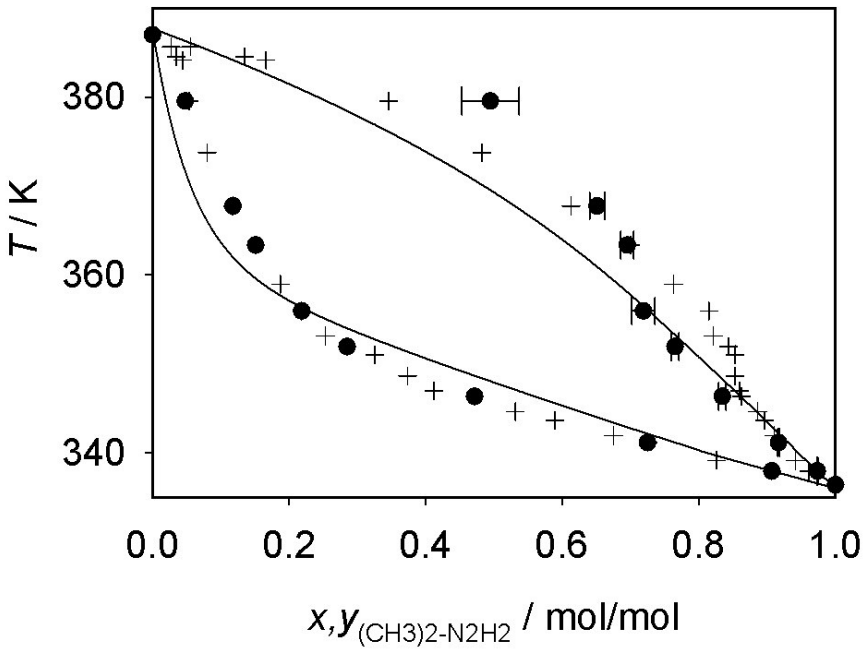

Figure 62: Isobaric vapor-liquid phase diagram of dimethylhydrazine + hydrazine at 0.1013 MPa: (+) experimental data by Pannetier and Mignotte [146]; (●) simulation data (ξ=1.01); (——) Peng-Robinson EOS (k_{ij}=−0.1).

of the Peng-Robinson EOS (k_{ij} = 0.055 for hydrazine, k_{ij} = 0 for monomethylhydrazine, k_{ij} = 0.07 for dimethylhydrazine).

It can be seen in the Figure 63 that Peng-Robinson EOS matches very well with the experimental data for hydrazine and monomethylhydrazine. For dimethylhydrazine, some deviations of the Peng-Robinson EOS from the experimental data at 293 K in the dimethylhydrazine-rich region are present, which are attributed to the misfit of the pure substance vapor pressure.

The results obtained by molecular simulation match very well with the experimental data at the different temperatures for monomethylhydrazine, yielding a mean unsigned error of about 4.0 %. For dimethylhydrazine, the simulation results agree excellently with the experimental results at 253 and 293 K, differing by only about 0.2 % and 0.7 %, respectively, but they deviate from the experimental value at 273 K and x_{NH3} = 0.396 mol/mol by about 11.8%. The simulation results for hydrazine are in reasonable agreement with the experiment, yielding a mean unsigned error of about 7.3 %.

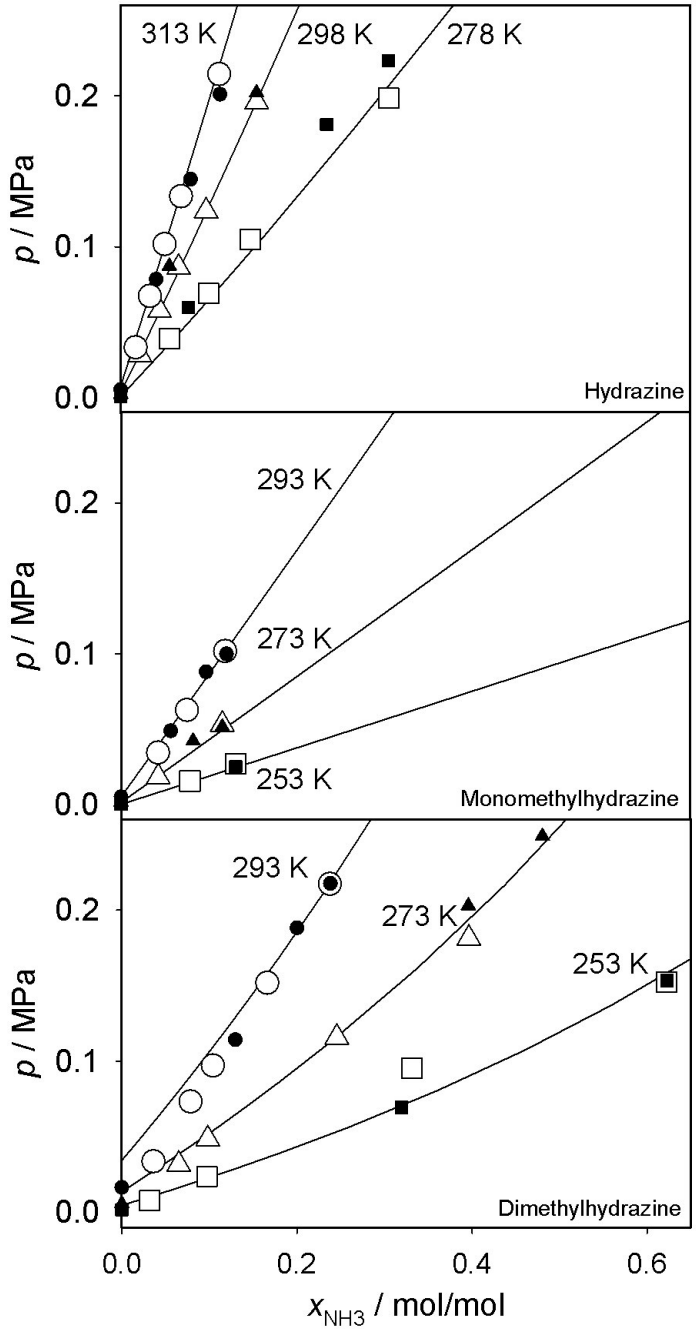

Figure 63: Isothermal vapor-liquid phase diagrams of binary mixtures containing ammonia and the hydrazines at different temperatures: (empty symbols) experimental data by Chang *et al.* [147]; simulation data, this work: (●) hydrazine (ξ=1.084), (▲) monomethylhydrazine (ξ=1.016), (■) dimethylhydrazine (ξ=0.94); (——) Peng-Robinson EOS (k_{ij}=0.055 for hydrazine, k_{ij}=0.0 for monomethylhydrazine and k_{ij}=0.07 for dimethylhydrazine). The statistical uncertainties of the present data are within symbol size.

10.3 Henry's law constant

Practical challenges in pressurizing, storing and pumping liquid propellants, like hydrazine and its derivatives, require accurate data on the solubility of ordinary gases [148]. However, absorption and desorption of these gases may cause undesirable mechanical and hydrodynamical effects in space vehicles [147]. Therefore, the solubility of a gas in these propellants should be small enough to permit its use as a pressurant in rocket booster engines [147].

On the basis of the newly developed molecular models, the Henry's law constant for the most important propellant pressurization gases Ar, N_2 and CO in the pure liquid hydrazines were predicted and compared with the experimental data by Chang *et al.* [147, 148], which is the sole publicly available source. For CO, the Henry's law constant was calculated only in liquid dimethylhydrazine, because no experimental data were available for the other two hydrazines.

Here, a straightforward route as described in [149] was followed. The Henry's law constant H_i is related to the residual chemical potential of the solute i at infinite dilution in the solvent μ_i^∞ [119, 150] by

$$H_i = \rho_s k_B T \exp(\mu_i^\infty/(k_B T)), \tag{49}$$

where ρ_s is the density of the solvent in its saturated liquid state.

The Henry's law constant is hence directly related to the unlike solvent-solute interaction and indirectly to the like solvent-solvent interaction, which yields the configurations of the solvent molecules and is fully given by the solvent model. To define the unlike LJ contribution between solute i and solvent molecules, the modified Lorentz-Berthelot combining rule, as described by Equations (17) and (18), was used.

It should be noted that the Henry's law constant decreases with increasing binary interaction parameter ξ, i.e. the solubility is enhanced due to stronger unlike dispersive attraction [119, 149]. Here, the binary interaction parameter ξ was adjusted to the experimental Henry's law constant data at the highest or at the lowest temperature for which binary experimental data exist. The temperature dependence that was obtained from simulation is thus a fully predictive property.

Figure 64 shows the predicted Henry's law constant H_i in liquid hydrazine, monomethylhydrazine and dimethylhydrazine in comparison to experimental data. All present data are given in numerical form in the appendix. Linear functions are sufficient to represent the data. It can be seen that the order of magnitude and also the temperature dependence of H_i vary very strongly for these systems. E.g., H_i ranges from around 10 to 20 GPa for Ar and N_2 in

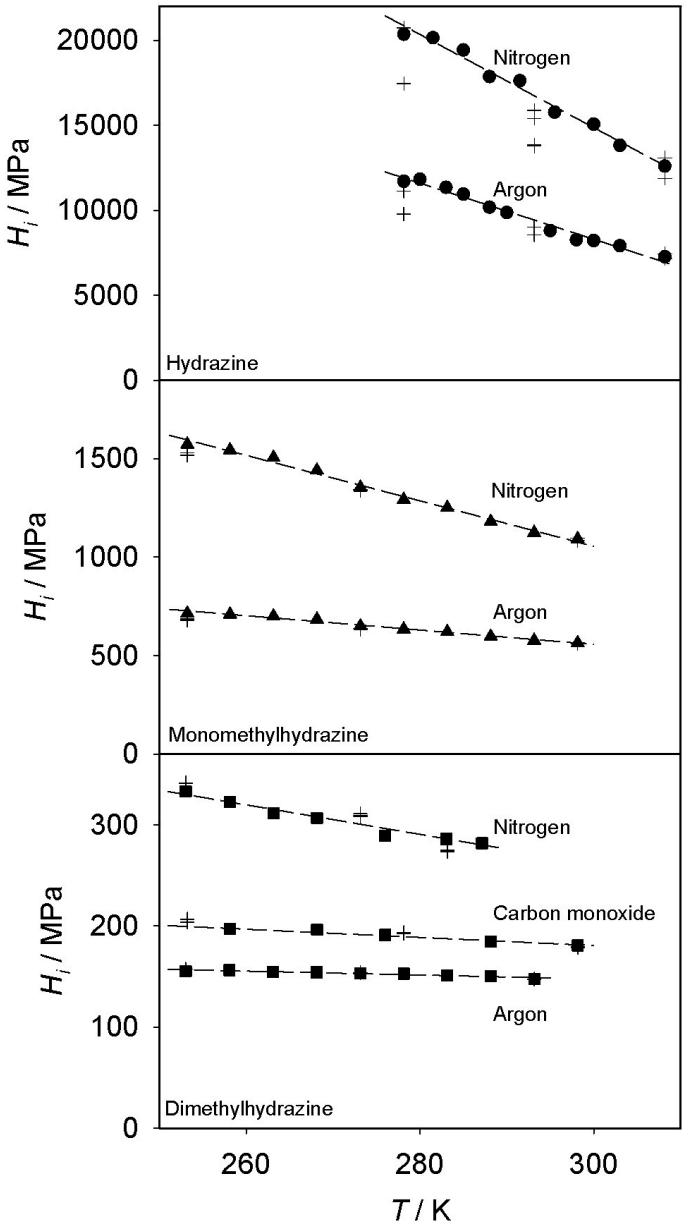

Figure 64: Henry's law constant of gases in liquid hydrazine, monomethylhydrazine and dimethylhydrazine: (+) experimental data by Chang *et al.* [147, 148]; simulation data, this work: (●) argon and nitrogen in hydrazine (ξ=1.02 for Ar and ξ=1.11 for N_2); (▲) argon and nitrogen in monomethylhydrazine (ξ=0.933 for Ar and ξ=0.976 for N_2); (■) argon, nitrogen and carbon monoxide in dimethylhydrazine (ξ=0.945 for Ar, ξ=0.955 for N_2 and ξ=1.005 for CO); (- - -) straight lines. The statistical uncertainties of the present data are within symbol size.

hydrazine to around 0.1 to 0.3 GPa for the same gases in dimethylhydrazine. Moreover, it strongly decreases with the temperature in the first case, but changes little with temperature in the second case.

The average deviation from the experimental gas solubility data for hydrazine is about 3.7% for Ar and 3.9% for N_2. The results obtained with the monomethylhydrazine model overestimate the available experimental data by about 2.5% for Ar and 1.3% for N_2. For the dimethylhydrazine model, the achieved agreement is also excellent, yielding a mean unsigned error of about 0.5% for Ar, 2.3% for N_2 and 1.7% for CO.

10.4 Discussion of the binary interaction parameter of the molecular models

In this work, a total of 14 binary mixtures containing hydrazines was studied. It should be noted that the adjusted binary interaction parameter, that acts between LJ sites of unlike molecule types, is close to the standard Lorentz-Berthelot combining rules (ξ=1), except for the aqueous systems. Table 1 lists all binary parameters. These values are in the range that was found for ξ in preceding work of our group [152] regarding 267 other binary mixtures.

For all systems containing water, the binary interaction parameter is the same (ξ=1.3) and differs quite strongly from the value ξ=1 that would be used for strictly predictive applications. As noticed by Huang *et al.* [124], this can be explained by the fact that the interactions of water are dominated by electrostatics and the comparably weak unlike dispersive interaction has to be modified significantly to adjust the mixture model.

10.5 Conclusion

Molecular modeling and simulation was applied to predict the phase behavior of pure fluids and binary mixtures containing hydrazine and two of its derivatives. New molecular models were developed for hydrazine, monomethylhydrazine and dimethylhydrazine, partly based on QC information on molecular geometry and electrostatics. Furthermore, experimental data on the saturated liquid density and the vapor pressure were taken into account to optimize the pure substance models. These pure substance properties were represented accurately from the triple point to the critical point. It was also shown that the hydrazine model is capable to predict the second virial coefficient and the density of homogeneous liquid hydrazine properly, while no experimental data for these properties were used in

the optimization procedure. Unfortunately, no experimental data on these properties were available for monomethylhydrazine. The density of homogeneous liquid dimethylhydrazine was also excellently predicted over a wide temperature range. The second virial coefficient of monomethylhydrazine and dimethylhydrazine was predicted, however, no other data were available for comparison. The new models were compared with molecular models by Gutowski *et al.* [112] and were found to yield more reliable results for most thermodynamic properties.

For an optimized description of the binary VLE, the unlike dispersive interaction was adjusted for all 14 studied binary systems to a single experimental vapor pressure of the mixture in the vicinity of ambient conditions. With these binary mixture models, VLE data were predicted for a temperature and composition range. The predictions show a good agreement with experimental binary VLE data that were not considered in the model development. The simulations also confirm that hydrazine and its derivatives are very dissimilar fluids. For instance dimethylhydrazine does not form an azeotrope with water, while the other two hydrazines do form an azeotrope. Moreover, the Henry's law constant of argon, nitrogen and carbon monoxide has a different order of magnitude and a different temperature dependence in these liquids.

In this work, molecular modeling and simulation was used to predict the fluid phase behavior and the thermodynamic properties of pure hydrazines and binary hydrazine mixture for which experimental data were available for comparison. The presented molecular models are able to reproduce the experimental data well that were not considered in the model development. Thus, these new models could also be valuable for the prediction of properties under different conditions and for systems where no experimental data are available.

11 Summary

Two newly constructed and built up experimental setups were presented in Section 2. These apparatuses operate with the synthetic method and cover a large temperature range from 203.15 to 600 K and a maximum pressure of 70 MPa. Moreover, an existing analytical experimental setup was recommissioned. In Section 3, a short introduction into molecular simulation was given with a focus on the modeling strategy for pure fluids and mixtures. An overview of the Peng-Robinson equation of state (EOS) was given in Section 4. Here, different alpha functions, the quadratic mixing rule and the Huron-Vidal mixing rule as well as the calculation of the enthalpy of pure fluids and mixtures with the Peng-Robinson EOS were discussed. Within this work, the simulation tool *ms*2 was extended to sample the radial distribution function (RDF) such that the RDF can be calculated between all possible sites on the fly. The RDF was applied to pure substances and mixtures (cf. Section 5).
A new force field model for pure acetone was presented, (cf. Section 6). It was successfully validated with various experimental data from the literature and an accurate EOS. The properties which were used for the validation are vapor-liquid equilibrium (VLE) data, data in the homogeneous liquid state (density, residual enthalpy and speed of sound), second virial coefficient, diffusion coefficient, thermal conductivity as well as the shear viscosity. Overall, the agreement between data from molecular simulation and reference data was very good. The VLE behavior of the mixtures nitrogen + acetone and oxygen + acetone was studied with molecular simulation and experiment on the basis of the new experimental setups and the new force field model for acetone. Thus, a large database was generated from simulation and experiment, especially for nitrogen + acetone. This mixture was studied for temperatures between 223 and 480 K, which is near the critical temperature of acetone. For oxygen + acetone, only few experimental measurements at low temperatures and pressures were made due to safety issues. The molecular model mixture parameter was adjusted to these data in order to predict properties over a much wider temperature and pressure range by molecular simulation. In addition, the Peng-Robinson EOS was adjusted for both systems as a basis for further applications.
New force field models for hexamethyldisiloxane (MM) and octamethylcyclotetrasiloxane (D4) were developed, (cf. Section 7). A modeling approach with nine LJ sites and nine point charges for MM and 16 LJ sites and 16 point charges for D4 was chosen for these rel-

atively large molecules. Despite the fact that these large molecules were described as rigid, the agreement between the simulation results and experimental data from the literature are very satisfying for both MM and D4. Because there are comparatively few experimental data available for MM and D4, the new models are suitable to generate simulation data for the adjustment of a hybrid EOS based on the Helmholtz energy.
Moreover, a force field model for decafluorobutane, which is a large molecule as well, was presented (cf. Section 8). For this model, 14 LJ sites and 14 point charges were used. The outcome of the validation with experimental data was that this model is suitable to predict the thermodynamic properties of decafluorobutane accurately. Thus, it can be applied in further studies of mixtures containing decafluorobutane. In addition, the Peng-Robinson EOS with the Mathias-Copeman alpha-function was discussed. The results for VLE properties, like the saturated liquid density and the Enthalpy of vaporization, are worse.
For the mixture carbon dioxide + 2,2-dimethyl-1-propanol new experimental data at the two isotherms 333.2 and 353.2 K were presented (cf. Section 9). This mixture could not be studied by molecular simulation due to the size of the large 2,2-dimethyl-1-propanol molecule. In this case, the internal degrees of freedom have to be considered. The obtained experimental data close the gap in the literature for the mixtures of carbon dioxide + low molar mass alcohols and were needed to validate a recently developed COSMO-SAC model.
For the hazardous substances hydrazine, monomethylhydrazine and 1,1-dimethylhydrazine new force field models were developed and validated successfully with existing experimental data from the literature (cf. Section 10). On the basis of available experimental mixture data containing the three hydrazines, mixture parameters were adjusted. Simulation results for the VLE behavior and the Henry's law constant of the studied mixtures were presented. It can be stated that molecular simulation is very adequate to study such mixtures on the basis of pure fluid force field models. In addition, the Peng-Robinson EOS using the quadratic mixing rule was adjusted to the considered mixtures.

In conclusion, the present work has pointed out that molecular simulation in combination with experiment is very suitable to obtain thermodynamic properties. The advantages of both methods were exploited. Applying the experimental approach, studies were directly done with the substance. Thus, accurate results can be achieved which were used to adjust and to validate force field models. For this purpose, not many experimental data points were necessary. In addition, substances consisting of very large molecules can usually be examined more easily by experiment.
Due to the fact that molecular simulations are generally cheaper than experiments, this approach was applied wherever applicable. The study of the VLE behavior of the mixture nitrogen + acetone shows that there are only small deviations between the data from molecular

simulation and experiment over a wide temperature and pressure range. Moreover, molecular simulation can be applied for hazardous substances without any extra effort, as can be seen with the mixture oxygen + acetone and the three hydrazines. Even molecules with a relatively large size like the two siloxanes MM and D4 as well as decafluorobutane were modelled successfully.

Bibliography

[1] http://www.sfbtrr75.de/website/index.php.

[2] Weigand, B.; Tropea, C. *Droplet dynamics under extreme boundary conditions: The collaborative research center SFB-TRR 75.* ICLASS, 2012.

[3] Oldenhof, E.; Weckenmann, F.; Lamanna, G.; Weigand, B.; Bork, B.; Dreizler, A. *Experimental investigation of isolated acetone droplets at ambient and near-critical conditions, injected in a nitrogen atmosphere*. Progress in Propulsion Physics **2013**, 4, 257-270.

[4] Chrigui, M.; Gounder, J.; Sadiki, A.; Masri, A.; Janicka, J. *Partially premixed reacting acetone spray using LES and FGM tabulated chemistry*. Combust. Flame **2012**, 159, 2718-2741.

[5] Peng, D.Y.; Robinson, D.B. *A new two-constant equation of state*. Ind. Chem. Eng. Fundam. **1976**, 15, 59-64.

[6] Deublein, S.; Eckl, B.; Stoll, J.; Lishchuk, S.V.; Guevara-Carrion, G.; Glass, C.W.; Merker, T.; Bernreuther, M.; Hasse, H.; Vrabec, J. *ms2: A molecular simulation tool for thermodynamic properties*. Comput. Phys. Commun. **2011**, 182, 2350-2367.

[7] Reiser, S.; Deublein, S.; Vrabec, J.; Hasse, H. *Molecular dispersion energy parameters for alkali and halide ions in aqueous solution*. J. Chem. Phys. **2014**, 140, 044504.

[8] Hsieh, C.M.; Sandler, S.I.; Lin, S.T. *Improvements of COSMO-SAC for vapor-liquid and liquid-liquid equilibrium predictions*. Fluid Phase Equilib. **2010**, 297, 90-97.

[9] Fonseca, J.M.S.; Dohrn, R.; Peper, S. *High-pressure fluid-phase equilibria: Experimental methods and systems investigated (2005–2008)*. Fluid Phase Equilib. **2011**, 300, 1-69.

[10] Rumpf, B.; Maurer, G. *Solubilities of hydrogen cyanide and sulfur dioxide in water at temperatures from 293.15 to 413.15 K and pressures up to 2.5 MPa*. Fluid Phase Equilib. **1992**, 81, 241-260.

[11] Rumpf, B.; Maurer, G. *An experimental and theoretical investigation on the solubility of carbon dioxide in aqueous solutions of strong electrolytes*. Ber. Bunsen. Phys. Chem. **1993**, 97, 85-97.

[12] Span, R.; Lemmon, E.W.; Jacobsen, R.T.; Wagner, W.; Yokozeki, W. *A reference quality thermodynamic property formulation for nitrogen*. J. Phys. Chem. Ref. Data **2000**, 29, 1361-1433.

[13] Schmidt, R.; Wagner, W. *A new form of the equation of state for pure substances and its application to oxygen*. Fluid Phase Equilib. **1985**, 19, 175-200.

[14] Lemmon, E.W.; Span, R. *Short fundamental equations of state for 20 industrial fluids*. J. Chem. Eng. Data **2006**, 51, 785-850.

[15] Gremer, F.; Herres, G.; Gorenflo, D. *VLLE for mixtures of water and alcohols: Measurements and correlations.* Wiley-VCH, Weinheim, 2004.

[16] Walcher, W. *Praktikum der Physik.* Teubner, Stuttgart, 1974.

[17] Vrabec, J.; Hasse, H. *Grand Equilibrium: vapour-liquid equilibria by a new molecular simulation method*. Mol. Phys. **2002**, 100, 3375-3383.

[18] Vrabec, J.; Fischer, J. *Vapour liquid equilibria of mixtures from the NpT plus test particle method*. Mol. Phys. **1995**, 85, 781-792.

[19] Eckl, B. *Development of molecular models of real fluids for applications in process engineering.* PhD thesis, University of Stuttgart, 2010.

[20] Allen, M.P.; Tildesley, D.J. *Computer simulations of liquids.* Oxford University Press, Oxford, 1987.

[21] Gray, C.G.; Gubbins, K.E. *Theory of molecular fluids. 1. Fundamentals.* Clarendon Press, Oxford, 1984.

[22] Schnabel, T.; Vrabec, J.; Hasse, H. *Unlike Lennard-Jones parameters for vapor-liquid equilibria*. J. Mol. Liq. **2007**, 135, 170-178.

[23] Schnabel, T.; Vrabec, J.; Hasse, H. *Molecular simulation study of hydrogen bonding mixtures and molecular models for mono- and dimethylamine*. Fluid Phase Equilib. **2008**, 263, 144-159.

[24] Mathias, P.M.; Copeman, T.W. *Extension of the Peng-Robinson equation of state to complex mixtures: Evaluation of the various forms of the local composition concept*. Fluid Phase Equilib. **1983**, 13, 91-108.

[25] Smith, J.M.; VanNess, H.C.; Abbott, M.M. *Introduction to chemical engineering.* McGraw-Hill, New York, 1996.

[26] Huron, M.J.; Vidal, J. *New mixing rules in simple equations of state for representing vapour-liquid equilibria of strongly non-ideal mixtures*. Fluid Phase Equilib. **1979**, 3, 255-271.

[27] Abrams, D.; Prausnitz, J.M. *Statistical thermodynamics of liquid mixtures: A new expression for the excess Gibbs energy of partly or completely miscible systems*. AIChE J. **1975**, 21, 116-128.

[28] Yokozeki, A.; Shiflett, M.B. *Vapor–liquid equilibria of ammonia + ionic liquid mixtures*. Appl. Energy **2007**, 84, 1258-1273.

[29] Dohrn, R. *Berechnung von Phasengleichgewichten.* Vieweg, Braunschweig / Wiesbaden, 1994.

[30] Dortmunder Datenbank, Mixture Properties, Version 6.3.0.384, 2010.

[31] Ahmar, E.E.; Valtz, A.; Naidoo, P.; Coquelet, C.; Ramjugernath D. *Isothermal vapor-liquid equilibrium data for the perfluorobutane (R610) + ethane system at temperatures from (263 to 353) K*. J. Chem. Eng. Data **2011**, 56, 1918–1924.

[32] Mathews, J.F. *Critical constants of inorganic substances*. Chem. Rev. **1972**, 72, 71-100.

[33] Orbey, H.; Sandler, S.I. *modeling vapor-liquid equilibria: Cubic equations of state and their mixing rules.* Cambridge University Press, New York, 1998.

[34] Marrero-Morejon, J.; Pardillo-Fontdevila, E. *Estimation of pure compound properties using group-interaction contributions*. AIChE J. **1999**, 45, 615-621.

[35] Tillner-Roth, R.; Harms-Watzenberg, F.; Baehr, H.D. *Eine neue Fundamentalgleichung für Ammoniak. DKV-Tagungsbericht* **1993**, 20, 167-181.

[36] Jabloniec, A.; Horstmann, S.; Gmehling, J. *Experimental determination and calculation of gas solubility data for nitrogen in different solvents*. Ind. Eng. Chem. Res. **2007**, 46, 4654-4659.

[37] Just, G. *Löslichkeit von Gasen in organischen Lösungsmitteln*. Z. Phys. Chem. **1901**, 37, 342-367.

[38] Horiuti, J. *On the solubility of gas; coefficient of dilatation by absorption*. Sci. Papers Inst. Phys. Chem. Res. (Japan) **1931**, 17, 125-256.

[39] Kretschmer, C.B.; Nowakowska J.; Wiebe R. *Solubility of oxygen and nitrogen in organic solvents from -25 to 50 C*. Ind. Eng. Chem. **1946**, 38, 506-509.

[40] Nitta, T.; Nakamura, Y.; Ariyasu, H.; Katayam, T. *Solubilities of nitrogen in binary solutions of acetone with cyclohexane, benzene, chloroform and 2-propanol*. J. Chem. Eng. (Japan) **1980**, 13, 97-103.

[41] Vosmansky, J.; Dohnal, V. *Gas solubility measurements with an apparatus of the Ben-Naim-Baer type*. Fluid Phase Equilib. **1987**, 33, 137-155.

[42] Tsuji, K.; Ichikawa, K.; Yamamoto, H.; Tokunaga, J. *Solubilities of oxygen and nitrogen in acetone-water mixed solvent*. Kagaku Kogaku Ronbunshu **1987**, 13, 825-830.

[43] Stubbs, J.M.; Potoff, J.J.; Siepmann, J.I. *Transferable potentials for phase equilibria. 6. united-atom description for ethers, glycols, ketones, and aldehydes*. J. Phys. Chem. B **2004**, 108, 17596-17605.

[44] Kamath, G.; Georgiev, G.; Potoff, J.J. *Molecular modeling of phase behavior and microstructure of acetone-chloroform-methanol binary mixtures*. J. Phys. Chem. B **2005**, 109, 19463-19473.

[45] Ferrando, N.; Lachet, V.; Boutin, A. *Monte Carlo simulations of mixtures involving ketones and aldehydes by a direct bubble pressure calculation*. J. Phys. Chem. B **2010**, 114, 8680-8688.

[46] Jorgensen, W.L.; Madura, J.D.; Swenson, C.J. *Optimized intermolecular potential functions for liquid hydrocarbons*. J. Am. Chem. Soc. **1984**, 106, 6638-6646.

[47] Vrabec, J.; Stoll, J.; Hasse, H. *A set of molecular models for symmetric quadrupolar fluids*. J. Phys. Chem. B **2001**, 105, 12126-12133.

[48] Levi, M.G. *Sull'energia basica dell' ossido di nrgento in soluzione. Gazz. Chim. Ital.* **1901**, 31, 513-541.

[49] Fischer, F.; Pfleiderer, G. *Über die Löslichkeit von Sauerstoff in verschiedenen organischen Lösungsmitteln*. Z. Anorg. Allg. Chem. **1922**, 124, 61-69.

[50] Finlayson, T.C. *Industrial oxygen*. Trans. Inst. Chem. Engr. **1923**, 1, 3-83.

[51] Schlaepfer, P.; Audykowski, T.; Bukowiecki, A. *Über die Lösungsgeschwindigkeit des Sauerstoffs in verschiedenen Flüssigkeiten*. Schweizer Archiv für Wiss. u. Technik **1949**, 15, 299-307.

[52] Sinn, E.; Matthes, K.; Naumann, E. *Experimentelle Untersuchungen über die Löslichkeit von Sauerstoff in flüssigen organischen Substanzen*. Wiss. Z. Fr.-Schiller-Univ. Jena, Math.-Naturwiss. R. **1967**, 16, 523-529.

[53] Naumenko, N.K. *Investigation on the solubility of oxygen in organic solvents.* PhD thesis, Leningrad, 1970.

[54] Bub, G.K.; Hillebrand, W.A. *Solubility of oxygen in 2-propanone, 2-butanone, 2-pentanone; 2-hexanone*. J. Chem. Eng. Data **1979**, 24, 315-319.

[55] Luehring, P.; Schumpe, A. *Gas solubilities (H2, He, N2, CO, O2, Ar, CO2) in organic liquids at 293.2 K*. J. Chem. Eng. Data **1989**, 34, 250-252.

[56] Schmidt, M.W.; Baldridge, K.K.; Boatz, J.A.; Elbert, S.T.; Gordon, M.S.; Jensen, J.H.; Koseki, S.; Matsunaga, N.; Nguyen, K.A.; Windus, T.L.; Dupuis, M.; Montgomery Jr., J.A. *General atomic and molecular electronic structure system*. J. Comput. Chem. **1993**, 14, 1347-1363.

[57] Mulliken, R.S. *Criteria for the construction of good self-consistent-field molecular orbital wave functions, and the significance of LCAO-MO population analysis*. J. Chem. Phys. **1964**, 36, 3428-3440.

[58] Huang, Y.-L.; Heilig, M.; Hasse, H.; Vrabec, J. *Vapor-Liquid equilibria of hydrogen chloride, phosgene, benzene, chlorobenzene, ortho-dichlorobenzene and toluene by molecular simulation*. AIChE J. **2011**, 52, 1043-1060.

[59] Stoll, J. *Molecular models for the prediction of thermalphysical properties of pure fluids and mixtures.* Fortschritt-Berichte VDI, Reihe 3, vol. 836, VDI-Verlag, Düsseldorf, 2005.

[60] Rowley, R.L.; Wilding, W.V.; Oscarson, J.L.; Yang, Y.; Zundel, N.A.; Daubert, T.E.; Danner, R.P. *The DIPPR data compilation of pure compound properties.* Design Institute for Physical Properties, AIChE, New York, 2006.

[61] Lotfi, A.; Vrabec, J.; Fischer, J. *Vapour liquid equilibria of the Lennard-Jones fluid from the NpT plus test particle method*. Mol. Phys. **1992**, 76, 1319-1333.

[62] Eckl, B.; Vrabec, J.; Hasse, H. *An optimized molecular model for ammonia*. Mol. Phys. **2008**, 106, 1039-1046.

[63] Guevara-Carrion, G.; Nieto-Draghi, C.; Vrabec, J.; Hasse, H. *Prediction of transport properties by molecular simulation: methanol and ethanol and their mixture*. J. Phys. Chem. B **2008**, 112, 16664-16674.

[64] Ertl, H.; Dullien, F.A.L. *Self-diffusion and viscosity of some liquids as a function of temperature*. AIChE J. **1973**, 19, 1215-1223.

[65] McCall, D.W.; Douglass, D.C.; Anderson, E.W. *Diffusion in liquids*. J. Chem. Phys. **1959**, 31, 1555-1557.

[66] Krüger, G.J.; Weiss, R. *Diffusionskonstanten einiger organischer Flüssigkeiten*. Z. Naturforsch. **1979**, 25a, 777-780.

[67] Holz, M.; Mao, X.; Seiferling, D.; Sacco, A. *Experimental study of dynamic isotope effects in molecular liquids: Detection of translationrotation coupling*. J. Chem. Phys. **1996**, 104, 669-679.

[68] Wheeler, D.R.; Rowley, R.L. *Shear viscosity of polar liquid mixtures via non-equilibrium molecular dynamics: Water, methanol, and acetone*. Mol. Phys. **1998**, 94, 555-564.

[69] Wohlfarth, C.; Wohlfahrt, B. Lechner, M.D. (ed.). C3, SpringerMaterials - The Landolt-Börnstein database, DOI: 10.1007/10639283_4, 2013.

[70] Merker, T.; Franke, N.; Gläser, R.; Schleid, T.; Hasse, H. *Gas solubility in binary liquid mixtures: Carbon dioxide in cyclohexane + cyclohexanone*. J. Chem. Eng. Data **2011**, 56, 2477-2481.

[71] Colonna, P.; Nannan, N.R.; Guardone, A.; Lemmon, E.W. *Multiparameter equations of state for selected siloxanes*. Fluid Phase Equilib. **2006**, 244, 193-211.

[72] Lustig, R. *Direct molecular NVT simulation of the isobaric heat capacity, speed of sound and Joule-Thomson coefficient*. Mol. Sim. **2011**, 37, 457-465.

[73] Lustig, R. *Statistical analogues for fundamental equation of state derivatives*. Mol. Phys. **2012**, 110, 3041-3052.

[74] Rutkai, G.; Thol, M.; Lustig, R.; Span, R.; Vrabec, J. *Communication: Fundamental equation of state correlation with hybrid data sets*. J. Chem. Phys. **2013**, 139, 041102.

[75] Schnabel, T.; Srivastava, A.; Vrabec, J.; Hasse, H. *Hydrogen bonding of methanol in supercritical CO2: Comparison between 1H-NMR spectroscopic data and molecular simulation results*. J. Phys. Chem. B **2007**, 111, 9871-9878.

[76] McLure, I.A.; Pretty, A.J.; Sadler, P.A. *Specific volumes, thermal pressure coefficients, and derived quantities of five dimethylsiloxane oligomers from 25 to 140 C*. J. Chem. Eng. Data **1977**, 22, 372-376.

[77] Abbas, R. *Anwendung der Gruppenbeitragszustandsgleichung VTPR für die Analyse von reinen Stoffen und Mischungen als Arbeitsmittel in technischen Kreisprozessen.* PhD thesis, TU Berlin, 2011.

[78] Wappmann, S.J.; Tarassov, I.N.; Lüdemann, H.-D. *Densities of octamethylcyclotetrasiloxane + methane and 2,2-dimethylpropane + methane from 10 to 200 MPa and from 294 to 433 K*. J. Chem. Eng. Data **1996**, 41, 84-88.

[79] Easteal, A.J.; Woolf, L.A. *Self-diffusion and volumetric measurements for octamethylcyclotetrasiloxane under pressure at 323 K*. J. Chem. Soc. Faraday Trans. 1 **1984**, 80, 549-551.

[80] Herring, W.A.; Winnick, J. *Excess volumes of octamethylcyclotetrasiloxane + carbon tetrachloride*. J. Chem. Thermodyn. **1974**, 6, 957-964.

[81] Dubberke, personal communication, 2013.

[82] Niepmann, R.; Schmidt, U. *Speeds of sound in liquid octamethylcyclotetrasiloxane*. J. Chem. Thermodyn. **1980**, 12, 1133-1137.

[83] Kirk, E.; Othmer, F. *Encyclopedia of chemical technology, 3rd ed.* Interscience, New York, 1978.

[84] Lavygin, I.A.; Skorokhodov, I.I.; Sobolevskii, M.V.; Nazarova, D.V.; Latarev, M.B.; Kudinova, O.M.; Vorapayeva, G.V. *The type of intermolecular reactions and intramolecular mobility in polyorganosiloxanes*. Polym. Sci. USSR **1976**, 18, 107-113.

[85] Rowe, V.K.; Spencer, H.C.; Bass, S.L. *Toxicological studies on certain commercial silicones and hydrolyzable silane intermediates*. J. Ind. Hyg. **1948**, 30, 332-352.

[86] Hunter, M.J.; Warrick, E.L.; Hyde, J.F.; Currie, C.C. *Organosilicon polymers. II. The open chain dimethylsiloxanes with trimethylsiloxy end groups*. J. Am. Chem. Soc. **1946**, 68, 2284-2290.

[87] Hurd, C.B. *Studies on siloxanes. I. The specific volume and viscosity in relation to temperature and constitution*. J. Am. Chem. Soc. **1946**, 68, 364-370.

[88] Wilcock, D.F. *Vapor pressure-viscosity relations in methylpolysiloxanes*. J. Am. Chem. Soc. **1946**, 68, 691-696.

[89] Nezbeda, I.; Kolafa, J. *A new version of the insertion particle method for determining the chemical potential by Monte Carlo simulation*. Mol. Sim. **1991**, 5, 391-403.

[90] Widom, B. *Some topics in the theory of fluids*. J. Chem. Phys. **1963**, 39, 2808-2812.

[91] Green, M.S. *Markoff random processes and the statistical mechanics of time-dependent phenomena. II. Irreversible processes in fluids*. J. Chem. Phys. **1954**, 22, 398-413.

[92] Kubo, *R. Statistical-mechanical theory of irreversible processes. I. General theory and simple applications to magnetic and conduction problems*. J. Phys. Soc. Jpn. **1957**, 12, 570-586.

[93] Schoen, M.; Hoheisel, C. *The mutual diffusion coefficient D 12 in binary liquid model mixtures. Molecular dynamics calculations based on Lennard-Jones (12-6) potentials*. Mol. Phys. **1984**, 52, 33-56.

[94] Lustig, R. *Angle-average for the powers of the distance between two separated vectors*. Mol. Phys. **1988**, 65, 175-179.

[95] Flyvbjerg, H.; Petersen, H.G. *Error estimates on averages of correlated data*. J. Chem. Phys. **1989**, 91, 461-466.

[96] Missenard, A. *Conductivite Thermique des Solides, Liquides, Gaz et de Leurs Melanges*. Editions Eyrolles, Paris **1965**.

[97] Mills, R. *Intradiffusion of benzene in mixtures with octamethylcyclotetrasiloxane at 25 C*. Trans. Faraday Soc. **1971**, 67, 1654-1660.

[98] Marsh, K.N. *Mutual diffusion in octamethylcyclotetrasiloxane mixtures*. Trans. Faraday Soc. **1968**, 64, 894-901.

[99] Waterman, H.I.; Van Herwijen, W.; Denhartog, H.W. *Statistical-graphical survey of series of linear and cyclic dimethylsiloxanes*. J. Appl. Chem. **1958**, 8, 625-631.

[100] Reuther, H. *Über Silikone XIV: Über das Viskosität-Temperatur-Verhalten von Silikonölen unter Besonderer Berücksichtigung des Bereichs unter 0 C*. Chem. Tech. **1953**, 5, 268.

[101] Eckl, B.; Huang, Y.-L.; Vrabec, J.; Hasse, H. *Vapor pressure of R227ea + ethanol at 343.13 K by molecular simulation*. Fluid Phase Equilib. **2007**, 260, 177-182.

[102] Brown, J.A.; Mears, W.H. *Physical properties of n-perfluorobutane. J. Phys. Chem.* **1958**, 62, 960-962.

[103] Fowler, R.D.; Hamilton Jr., J.M.; Kasper, J.S.; Weber, C.; Burford III, W.B.; Anderson, H.C. *Physical and chemical properties of pure fluorocarbons*. Ind. Eng. Chem. **1947**, 39, 375-378.

[104] Mausteller, J.W. *The production of fluorocarbons by the electrochemical method.* PhD thesis, Pennsylvania State College, 1951.

[105] Tripp, T.B.; Dunlap, R.D. *Second virial coefficients for the systems: n-Butane + perfluoro-n-butane and dimethyl ether + 1-hydroperfluoropropane*. J. Phys. Chem. **1962**, 66, 635-639.

[106] Vacek, V.; Hallewell, G.; Lindsay, S. Proceedings of the 14th Symposium on Thermophysical Properties, Boulder, Co, June 25-30, pp. 11-14, 2000.

[107] Brostow, W.; McEachern, D.M.; Perez-Gutierrez, S. *Pressure second virial coefficients of hydrocarbons, fluorocarbons, and their mixtures: Interactions of walks*. J. Chem. Phys. **1979**, 71, 2716-2722.

[108] McCann, D.W. *A group contribution method for second virial coefficients.* MSc thesis, Pennsylvania State University, 1982.

[109] Lin, S.T.; Sandler, S.I. *A priori phase equilibrium prediction from a segment contribution solvation model*. Ind. Eng. Chem. Res. **2002**, 41, 899-913.

[110] Wang, S.; Sandler, S.I. *Refinement of COSMOSAC and the application. Ind*. Eng. Chem. Res. **2007**, 46, 7275-7288.

[111] Collins, G.E.; Rose-Pehrsson, S.L. *Fluorescent detection of hydrazine, monomethylhydrazine, and 1,1-dimethylhydrazine by derivatization with aromatic dicarbaldehydes*. Analyst **1994**, 119, 1907-1913.

[112] Gutowski, K.E.; Gurkan, B.; Maginn, E.J. *Force field for the atomistic simulation of the properties of hydrazine, organic hydrazine derivatives, and energetic hydrazinium ionic liquids*. Pure Appl. Chem. **2009**, 81, 1799-1828.

[113] Schmidt, E.W. *Hydrazine and its derivatives: Preparation, properties, applications.* Wiley, New York, 1984.

[114] Von Burg, R.; Stout, T. *Toxicology update: Hydrazine*. J. Appl. Toxicol. **1991**, 11, 447-450.

[115] Borodin, O. *Polarizable force field development and molecular dynamics simulations of ionic liquids*. J. Phys. Chem. B **2009**, 113, 11463-11478.

[116] Merker, T.; Vrabec, J.; Hasse, H. *Engineering molecular models: Efficient parameterization procedure and cyclohexanol as case study*. Soft Materials **2012**, 10, 3-24.

[117] Kaczmarek, A.; Shiga, M.; Marx, D. *Quantum effects on vibrational and electronic spectra of hydrazine studied by "on-the-fly" ab initio ring polymer molecular dynamics*. J. Phys. Chem. A **2009**, 113, 1985-1994.

[118] Seddon, W.A.; Fletcher, J.W.; Sopchyshyn, F.C. *Pulse radiolytic formation of solvated electrons in hydrazine*. Can. J. Chem. **1976**, 54, 2807-2812.

[119] Schnabel, T.; Vrabec, J.; Hasse, H. *Henry's law constants of methane, nitrogen, oxygen and carbon dioxide in ethanol from 273 to 498 K: Prediction from molecular simulation*. Fluid Phase Equilib. **2005**, 233, 134-143.

[120] Beamer, W. *The molecular structure of two dimethylhydrazines by electron diffraction*. J. Am. Chem. Soc. **1948**, 70, 2979-2982.

[121] Stoll, J.; Vrabec, J.; Hasse, H. *A set of molecular models for carbon monoxide and halogenated hydrocarbons*. J. Chem. Phys. **2003**, 106, 1039-1046.

[122] Jorgensen, W.L.; Chandrasekhar, J.D.; Madura, R.W.; Impey, R.W.; Klein, M.L. *Comparison of simple potential functions for simulating liquid water*. J. Chem. Phys. **1983**, 79, 926-935.

[123] Vega, C.; Abascal, J.L.F. *Simulating water with rigid non-polarizable models: A general perspective*. Phys. Chem. Chem. Phys. **2011**, 13, 19663-19688.

[124] Huang, Y.-L.; Merker, T.; Heilig, M.; Hasse, H.; Vrabec, J. *Molecular modeling and simulation of vapor-liquid equilibria of ethylene oxide, ethylene glycol and water as well as their binary mixtures*. Ind. Eng. Chem. Res. **2012**, 51, 7428-7440.

[125] Huang, Y.-L. *Molecular modeling and simulation of real fluids for applications in process Engineering.* PhD thesis, University of Paderborn, 2010.

[126] Horn, H.W.; Swope, W.C.; Pitera, J.W.; Madura, J.D.; Dick, T.J.; Hura, G.L.; Head-Gordon, T. *Development of an improved four-site water model for biomolecular simulations: TIP4P-Ew*. J. Chem. Phys. **2004**, 120, 9665-9678.

[127] Abascal, J.L.F.; Vega, C. *A general purpose model for the condensed phases of water: TIP4P/2005*. J. Chem. Phys. **2005**, 123, 234505-234516.

[128] Abascal, J.L.F.; Sanz, E.; García Fernández, R.; Vega, C. *A potential model for the study of ices and amorphous water: TIP4P/Ice*. J. Chem. Phys. **2005**, 122, 234511-234519.

[129] Guissani, Y.; Guillot, B. *A computer simulation study of the liquid-vapor coexistence curve of water*. J. Chem. Phys. **1993**, 98, 8221-8235.

[130] Merseburger Datenbank MDB for thermophysical data of pure compounds, Revision 7.1.0, 2010.

[131] Haws, J.L.; Harden, D.G. *Thermodynamic properties of hydrazine*. J. Spacecr. Rockets **1965**, 2, 972-974.

[132] Audrieth, L.F.; Ackerson Ogg, B. *The Chemistry of Hydrazine.* John Wiley, New York, 1951.

[133] Drago, R.S.; Sisler, H.H. *Liquid-vapor equilibria in the system ammonia-hydrazine at elevated temperatures*. J. Phys. Chem. **1956**, 60, 245-249.

[134] Tsonopoulos, C. *Second virial coefficients of water pollutants*. AIChE J. **1978**, 24, 1112-1115.

[135] Guggenheim, E.A. *The principle of corresponding states*. J. Chem. Phys. **1945**, 13, 253-261.

[136] Aston, J.G.; Wood, J.L.; Zolki, T.P. *The thermodynamic properties and configuration of unsymmetrical dimethylhydrazine*. J. Am. Chem. Soc. **1953**, 75, 6202-6204.

[137] www.atsdr.cdc.gov/ToxProfiles/tp100-c4.pdf

[138] Uchida, S.; Ogawa, S.; Yamaguchi, M. *Studies in distillation*. Jap. Sci. Rev. Eng. Sci. **1950**, 1, 41-49.

[139] de Bruyn, C.A.; Dito, J.W. *The boilingpoint curve for the system: Hydrazine + water*. Proc. Sec. Sci., K. Akad. Wet. Amsterdam **5**, 1902-1903, 171-183.

[140] Sridhar, S.; Ravindra, R.; Khan, A.A. *Recovery of monomethylhydrazine liquid propellant by pervaporation technique*. Ind. Eng. Chem. Res. **2000**, 39, 2485-2490.

[141] Ferriol, M.; Laachach, A.; Cohen-Adad, M.T.; Getzen, F.W.; Jorat, L.; Noyel, G.; Huck, J.; Bureau, J.C. *Vapor-liquid equilibria in the binary systems water-methylhydrazine and water-1,1-dimethylhydrazine. Thermodynamic modeling in relation to the structure of the liquid phase*. Fluid Phase Equilib. **1992**, 71, 287-299.

[142] Cohen-Adad, M.T.; Allali, I.; Getzen, F.W. *Modelization of liquid associated binary mixtures: Application to liquid vapor equilibria of binary systems containing water, hydrazines and hydrazones*. J. Solution Chem. **1987**, 16, 659-678.

[143] U.S. Environmental Protection Agency. Health and environmental effects profile for 1,1-dimethylhydrazine. EPA/600/x-84/134. environmental criteria and assessment office, Office of Health and Environmental Assessment, Office of Research and Development, Cincinnati, OH, 1984

[144] Carleton, L.T. *Phase equilibria in dimethylhydrazine-water system*. Ind. Eng. Chem. Chem. Eng. Data Series **1956**, 1, 21-24.

[145] Copeland, J.P.; Simmons, J.A.; Spurlock, J.M. *Determination of thermodynamic properties of aerozine-50.* Phase I Report for Manned Spacecraft Center, National Aeronautics and Space Administration, Atlantic Research Corporation, 1967.

[146] Pannetier, G.; Mignotte, P. *Equilibre liquide-vapeur du binaire hydrazine-dimethylhydrazine asymetrique*. Bull. Soc. Chim. Fr. **1961**, 143, 985-988.

[147] Chang, E.T.; Gokcen, N.A.; Poston, T.M. *Thermodynamic properties of gases in propellants. Solubilities of gaseous ammonia, carbon monoxide, carbon dioxide, and sulfur hexafluoride*. J. Chem. Eng. Data **1971**, 16, 404-408.

[148] Chang, E.T.; Gokcen, N.A.; Poston, T.M. *Thermodynamic properties of gases in propellants. II. Solubilities of helium, nitrogen and argon gas in hydrazine, methylhydrazine, and unsymmetrical dimethylhydrazine*. J. Phys. Chem. **1968**, 72, 638-642.

[149] Huang, Y.-L.; Miroshnichenko, S.; Hasse, H.; Vrabec, J. *Henry's law constant from molecular simulation: A systematic study of 95 systems*. Int. J. of Thermophys. **2009**, 30, 1791-1810.

[150] Shing, K.S.; Gubbins, K.E.; Lucas, K. *Henry constants in nonideal fluid mixtures. Computer simulation and theory*. Mol. Phys. **1988**, 65, 1235-1252.

[151] Guevara-Carrion, G.; Hasse, H.; Vrabec, J. *Thermodynamic properties for applications in chemical industry via classical force fields*. Top. Curr. Chem. **2012**, 307, 201-250.

[152] Vrabec, J.; Huang, Y.-L.; Hasse, H. *Molecular models for 267 binary mixtures validated by vapor-liquid equilibria: a systematic approach*. Fluid Phase Equilib. **2009**, 279, 120-135.

[153] Vrabec, J.; Kettler, M.; Hasse, H. *Chemical potential of quadrupolar two-centre Lennard-Jones fluids by gradual insertion*. Chem. Phys. Lett. **2002**, 356, 431-436.

Appendix

A Systems containing acetone

A.1 Experimental and simulation results

Table A.1: Henry's law constant of nitrogen in acetone and of oxygen in acetone calculated on basis of the experimental data generated in this work. The number in parentheses indicates the uncertainty in the last digit.

T	H_{N2}	H_{O2}
K	MPa	MPa
223	252 (16)	
253		150 (9)
283		143 (9)
303	187 (12)	
323	171 (11)	
343	157 (10)	
363	141 (9)	

Table A.2: Nitrogen + acetone: Experimental vapor-liquid equilibrium data along the saturated liquid line and along the saturated vapor line for the vapor pressure p, the saturated liquid mole fraction x_{N2} and the saturated vapor mole fraction y_{N2}. The number in parentheses indicate the uncertainty in the last digit.

T	p	x_{N2}	y_{N2}	T	p	x_{N2}	y_{N2}
K	MPa	mol/mol	mol/mol	K	MPa	mol/mol	mol/mol
223.2	9.68 (1)	0.032 (2)		323.2	1.34 (1)		0.930 (5)
223.2	2.97 (1)	0.011 (1)		323.2	2.00 (1)	0.011 (1)	
223.2	3.79 (1)	0.014 (1)		323.2	2.35 (1)	0.013 (1)	
243.1	7.13 (1)	0.026 (2)		323.2	4.38 (1)	0.025 (2)	
273.1	7.70 (1)	0.033 (2)		323.2	6.65 (1)	0.037 (2)	
303.2	0.39 (1)		0.887 (5)	323.2	8.15 (1)	0.045 (3)	
303.2	0.43 (1)		0.902 (5)	323.2	9.73 (1)	0.053 (3)	
303.2	0.45 (1)		0.904 (5)	323.2	10.22 (1)	0.056 (3)	
303.2	0.56 (1)		0.925 (5)	323.2	11.14 (1)	0.060 (4)	
303.2	0.61 (1)		0.929 (5)	343.0	1.58 (1)		0.869 (5)
303.2	0.61 (1)		0.931 (5)	343.0	1.68 (1)		0.879 (5)
303.2	0.76 (1)		0.943 (5)	343.0	1.78 (1)		0.882 (5)
303.2	1.20 (1)		0.960 (5)	343.2	1.98 (1)	0.011 (1)	
303.2	2.09 (1)	0.011 (1)		343.2	4.19 (1)	0.025 (2)	
303.1	2.44 (1)	0.012 (1)		343.1	6.22 (1)	0.037 (2)	
303.2	4.64 (1)	0.024 (1)		343.1	7.71 (1)	0.047 (3)	
303.2	6.95 (1)	0.035 (2)		343.2	9.07 (1)	0.056 (3)	
303.2	8.70 (1)	0.044 (3)		343.2	10.38 (1)	0.063 (4)	
303.1	10.35(1)	0.051 (3)		363.2	2.00 (1)	0.012 (1)	
303.2	11.07(1)	0.054 (3)		363.1	2.43 (1)	0.015 (1)	
303.2	11.99(1)	0.058 (4)		363.2	4.08 (1)	0.026 (2)	
323.2	0.90 (1)		0.897 (5)	363.2	8.63 (1)	0.058 (4)	
323.0	1.03 (1)		0.909 (5)	400.0	2.65 (1)	0.016 (1)	
323.2	1.10 (1)		0.916 (5)	400.0	3.62 (1)	0.024 (2)	
323.0	1.25 (1)		0.926 (5)				

Table A.3: Oxygen + acetone: Experimental vapor-liquid equilibrium data along the saturated liquid line for the vapor pressure p and the saturated liquid mole fraction x_{O2}. The number in parentheses indicates the uncertainty in the last digit.

T	p	x_{O2}
K	MPa	mol/mol
253.1	0.108 (1)	0.0007 (1)
253.1	0.380 (1)	0.0026 (2)
253.1	0.562 (1)	0.0040 (2)
253.1	0.731 (1)	0.0053 (3)
283.1	0.121 (1)	0.0007 (1)
283.2	0.395 (1)	0.0028 (2)
283.2	0.582 (1)	0.0042 (3)
283.1	0.753 (1)	0.0056 (3)

Table A.4: Nitrogen + acetone: Experimental data along the saturated liquid line for the vapor pressure p and the saturated liquid mole fraction x_{N2}. The number in parentheses indicates the uncertainty in the last digit.

T	p	x_{N2}
K	MPa	mol/mol
396	11.97 (7)	0.111 (9)
400	13.32 (7)	0.13 (1)
400	39.26 (7)	0.34 (3)
401	32.18 (7)	0.28 (2)
401	41.45 (7)	0.36 (3)
402	14.35 (7)	0.13 (1)
402	30.98 (7)	0.27 (2)
403	26.38 (7)	0.23 (2)
404	34.31 (7)	0.32 (3)
405	22.46 (7)	0.20 (2)
449	8.43 (7)	0.102 (8)
449	11.20 (7)	0.13 (1)
450	12.49 (7)	0.15 (1)
451	21.97 (7)	0.28 (2)
453	17.86 (7)	0.24 (2)
453	18.94 (7)	0.44 (4)
454	24.65 (7)	0.35 (3)
455	23.51 (7)	0.38 (3)
480	9.4 (7)	0.116 (9)
480	11.32 (7)	0.16 (1)
480	12.31 (7)	0.19 (1)
481	11.74 (7)	0.16 (1)
482	13.28 (7)	0.30 (2)
483	12.76 (7)	0.22 (2)

Table A.5: Acetone: Vapor-liquid equilibrium simulation data for the vapor pressure p, saturated liquid density ρ', saturated vapor density ρ'' and enthalpy of vaporization Δh_v. The number in parentheses indicates the statistical uncertainty in the last digit.

T	p	ρ'	ρ''	Δh_v
K	MPa	mol/l	mol/l	kJ/mol
220		15.10 (2)		
240		14.72 (2)		
260		14.32 (2)		
300	0.0315 (8)	13.51 (1)	0.0129 (3)	31.04 (1)
350	0.198 (3)	12.47 (1)	0.073 (1)	27.95 (2)
400	0.720 (7)	11.27 (1)	0.256 (3)	24.15 (2)
450	1.85 (1)	9.64 (2)	0.676 (4)	19.05 (4)
470	2.62 (1)	8.83 (3)	1.010 (5)	16.31 (6)
480	3.05 (2)	8.33 (4)	1.208 (6)	14.76 (7)
490	3.52 (1)	7.65 (6)	1.540 (6)	12.4 (1)

Table A.6: Acetone: Simulation data for the density ρ, residual isobaric heat capacity c_p^{res}, speed of sound c and residual enthalpy h^{res} in the homogeneous region. The number in parentheses indicates the statistical uncertainty in the last digit.

T	p	ρ	c_p^{res}	c	h^{res}
K	MPa	mol/l	J/(mol K)	km/s	kJ/mol
200	5	15.503 (3)	57 (3)	1.64 (3)	-36.527 (9)
200	10	15.549 (2)	55 (2)	1.69 (2)	-36.293 (8)
200	20	15.628 (2)	52 (3)	1.73 (2)	-35.772 (8)
200	40	15.789 (2)	53 (2)	1.77 (2)	-34.810 (8)
300	5	13.604 (3)	50 (2)	1.20 (2)	-31.248 (7)
300	10	13.691 (3)	48 (1)	1.24 (1)	-31.044 (7)
300	20	13.846 (2)	46 (1)	1.311 (9)	-30.616 (6)
300	40	14.111 (3)	46 (1)	1.37 (1)	-29.713 (7)
300	95	14.696 (2)	45 (1)	1.57 (1)	-27.089 (6)
400	5	11.437 (5)	52 (1)	0.78 (1)	-26.255 (9)
400	10	11.636 (5)	50 (1)	0.82 (1)	-26.190 (8)
400	20	11.946 (4)	48 (1)	0.90 (1)	-25.928 (8)
400	40	12.445 (3)	42 (1)	1.035 (9)	-25.294 (7)
400	95	13.351 (2)	37 (1)	1.322 (8)	-22.990 (6)
500	5	7.30 (2)	140 (6)	0.27 (4)	-18.71 (2)
500	10	8.71 (1)	71 (3)	0.43 (2)	-20.38 (2)
500	20	9.726 (6)	51 (1)	0.59 (1)	-21.14 (1)
500	40	10.719 (4)	43 (1)	0.77 (1)	-21.169 (8)
500	95	12.075 (2)	32 (1)	1.118 (4)	-19.385 (6)
550	5	1.6431 (9)	48 (1)	0.215 (1)	-6.217 (5)
550	10	6.008 (9)	113 (4)	0.25 (2)	-15.47 (1)
550	20	8.387 (8)	56 (2)	0.46 (1)	-18.44 (1)
550	40	9.820 (5)	39 (1)	0.696 (6)	-19.136 (9)
550	95	11.477 (2)	32 (1)	1.020 (6)	-17.761 (7)

Table A.7: Acetone: Simulation data for the second virial coefficient B.

T	B
K	l/mol
240	-5.7
250	-4.4
260	-3.53
400	-0.662
550	-0.269
700	-0.1320
850	-0.0640
1000	-0.0238
1500	0.03778
2000	0.06216
2500	0.07464

Table A.8: Acetone: Simulation data for the self-diffusion coefficient D_i, shear viscosity ν and thermal conductovity λ anlong the saturated liquid line. The number in parentheses indicates the statistical uncertainty in the last digit.

T	D_i	T	ν	T	λ
K	10^{-10} m^2/s	K	mPa s	K	W/(m K)
200	7.59 (3)	200	1.4 (1)	190	0.19 (1)
225	14.12 (4)	225	0.77 (4)	223.15	0.21 (1)
250	22.81 (4)	250	0.51 (2)	253.15	0.19 (2)
270	30.19 (7)	270	0.39 (2)	274.15	0.19 (1)
298.15	44.39 (7)	298.15	0.29 (1)	298.15	0.17 (1)
315	53.11 (9)	315	0.24 (1)	323.15	0.16 (1)
325	59.39 (8)	325	0.22 (1)		

Table A.9: Nitrogen + acetone and oxygen + acetone: Simulation data for the Henry's law constant. The number in parentheses indicates the statistical uncertainty in the last digit.

nitrogen		oxygen	
T	H_{N2}	T	H_{O2}
K	MPa	K	MPa
225	236 (1)	243.15	137.6 (1)
250	225.9 (8)	253.15	137.5 (1)
275	211.2 (7)	263.15	137.1 (1)
300	184.3 (5)	273.15	136.2 (1)
314.25	176.4 (4)	283.15	133.1 (1)
350	147.4 (4)	293.15	131.2 (1)
390	119.3 (3)		
430	90.9 (4)		
470	62.5 (5)		

Table A.10: Oxygen + acetone: Vapor-liquid equilibrium simulation data for the vapor pressure p, saturated vapor mole fraction y_{O2}, saturated liquid density ρ', saturated vapor density ρ'' and enthalpy of vaporization Δh_v. The number in parentheses indicates the statistical uncertainty in the last digit.

T	x_{O2}	p	y_{O2}	ρ'	ρ''	Δh_v
K	mol/mol	MPa	mol/mol	mol/l	mol/l	kJ/mol
253.15	0.001	0.163 (2)	0.97 (1)	14.432 (2)	0.078 (1)	33.713 (5)
253.15	0.002	0.318 (2)	0.997 (2)	14.441 (2)	0.151 (1)	33.657 (4)
253.15	0.004	0.493 (4)	0.973 (5)	14.451 (2)	0.236 (2)	33.583 (5)
253.15	0.005	0.651 (5)	0.987 (3)	14.460 (2)	0.312 (2)	33.527 (5)
253.15	0.006	0.799 (5)	0.997 (1)	14.468 (2)	0.383 (2)	33.465 (4)
283.15	0.001	0.171 (4)	0.90 (2)	13.840 (2)	0.073 (2)	32.132 (6)
283.15	0.002	0.331 (3)	0.94 (1)	13.852 (2)	0.141 (1)	32.087 (5)
283.15	0.004	0.486 (4)	0.95 (1)	13.859 (2)	0.208 (2)	32.026 (6)
283.15	0.005	0.636 (6)	0.98 (1)	13.870 (2)	0.271 (2)	31.994 (5)
283.15	0.006	0.780 (3)	1.0 (1)	13.880 (2)	0.333 (1)	31.949 (4)

Table A.11: Nitrogen + acetone: Vapor-liquid equilibrium simulation data for the vapor pressure p, saturated vapor mole fraction y_{N2}, saturated liquid density ρ', saturated vapor density ρ'' and enthalpy of vaporization Δh_v. The number in parentheses indicates the statistical uncertainty in the last digit.

T	x_{N2}	p	y_{N2}	ρ'	ρ''	Δh_v
K	mol/mol	MPa	mol/mol	mol/l	mol/l	kJ/mol
223.15	0.007	1.73 (3)	0.994 (3)	15.055 (2)	0.95 (2)	34.867 (6)
223.15	0.078	2.31 (6)	1.0 (1)	15.076 (3)	1.28 (3)	34.692 (9)
223.15	0.012	2.95 (4)	0.9997 (2)	15.092 (2)	1.64 (2)	34.504 (6)
223.15	0.014	3.66 (5)	0.997 (1)	15.112 (2)	2.06 (3)	34.315 (5)
223.15	0.015	3.99 (7)	1.0 (1)	15.125 (3)	2.25 (4)	34.232 (7)
223.15	0.016	4.35 (7)	1.0 (1)	15.137 (2)	2.46 (4)	34.141 (6)
223.15	0.031	9.4 (2)	0.994 (1)	15.278 (6)	5.6 (1)	32.82 (2)
243.15	0.008	1.96 (2)	0.995 (1)	14.685 (2)	0.99 (1)	33.754 (6)
243.15	0.020	5.1 (1)	0.966 (9)	14.781 (3)	2.67 (6)	32.63 (4)
243.15	0.035	9.6 (1)	0.998 (1)	14.911 (4)	4.95 (6)	31.82 (1)
273.15	0.015	3.29 (5)	0.994 (2)	14.149 (5)	1.47 (2)	31.84 (1)
273.15	0.030	7.0 (1)	0.998 (1)	14.273 (8)	3.12 (5)	30.92 (1)
273.15	0.042	9.9 (1)	0.989 (2)	14.364 (5)	4.44 (5)	30.14 (2)
303.15	0.001	0.248 (8)	0.86 (3)	13.440 (2)	0.099 (3)	31.105 (6)
303.15	0.002	0.474 (6)	0.91 (1)	13.449 (2)	0.189 (2)	31.042 (6)
303.15	0.004	0.677 (6)	0.942 (7)	13.453 (2)	0.270 (3)	30.993 (6)
303.15	0.005	0.905 (9)	0.954 (8)	13.464 (2)	0.360 (4)	30.943 (6)
303.15	0.006	1.131 (8)	0.949 (5)	13.469 (2)	0.451 (3)	30.861 (6)
303.15	0.007	1.38 (1)	0.963 (6)	13.485 (4)	0.5497 (3)	30.82 (1)
303.15	0.008	1.57 (1)	0.961 (4)	13.487 (2)	0.625 (4)	30.746 (6)
303.15	0.010	2.01 (1)	0.976 (3)	13.503 (2)	0.800 (5)	30.638 (5)
303.15	0.013	2.49 (3)	0.972 (4)	13.524 (5)	0.993 (1)	30.51 (1)
303.15	0.029	5.65 (6)	0.989 (4)	13.636 (6)	2.238 (3)	29.69 (1)
303.15	0.045	9.0 (1)	0.995 (2)	13.753 (4)	3.55 (4)	28.825 (9)
303.15	0.053	10.8 (1)	0.995 (2)	13.815 (7)	4.23 (5)	28.40 (1)
303.15	0.056	11.4 (1)	0.994 (1)	13.838 (6)	4.46 (4)	28.27 (1)

Table A.11 continued.

T	x_{N2}	p	y_{N2}	ρ'	ρ''	Δh_v
K	mol/mol	MPa	mol/mol	mol/l	mol/l	kJ/mol
323.15	0.001	0.27 (1)	0.71 (3)	13.017 (2)	0.103 (3)	29.954 (8)
323.15	0.002	0.467 (9)	0.84 (2)	13.027 (2)	0.175 (5)	29.977 (7)
323.15	0.004	0.670 (8)	0.88 (1)	13.032 (5)	0.2518 (1)	29.92 (1)
323.15	0.004	0.681 (9)	0.86 (1)	13.038 (2)	0.255 (5)	29.925 (7)
323.15	0.005	0.873 (7)	0.899 (7)	13.043 (2)	0.328 (3)	29.888 (7)
323.15	0.006	1.077 (7)	0.908 (5)	13.049 (2)	0.401 (3)	29.841 (7)
323.15	0.007	1.285 (9)	0.921 (5)	13.060 (2)	0.486 (3)	29.764 (7)
323.15	0.019	3.33 (3)	0.967 (4)	13.137 (5)	1.242 (1)	29.24 (1)
323.15	0.024	4.34 (4)	0.970 (3)	13.170 (5)	1.618 (2)	28.94 (1)
323.15	0.035	6.26 (4)	0.980 (3)	13.246 (3)	2.32 (2)	28.453 (8)
323.15	0.043	7.70 (9)	0.985 (2)	13.301 (4)	2.87 (2)	28.067 (9)
323.15	0.045	8.25 (6)	0.980 (1)	13.319 (3)	3.05 (2)	27.92 (1)
323.15	0.053	9.82 (6)	0.983 (2)	13.379 (3)	3.61 (2)	27.552 (8)
323.15	0.056	10.4 (1)	0.986 (4)	13.40 (1)	3.79 (4)	27.46 (2)
343.15	0.004	0.73 (1)	0.72 (1)	12.600 (5)	0.2614 (2)	28.70 (1)
343.15	0.005	0.88 (1)	0.793 (8)	12.605 (3)	0.314 (3)	28.744 (8)
343.15	0.007	1.24 (1)	0.854 (7)	12.615 (3)	0.445 (3)	28.656 (9)
343.15	0.008	1.41 (4)	0.87 (2)	12.622 (6)	0.4997 (4)	28.65 (1)
343.15	0.008	1.434 (9)	0.864 (4)	12.627 (3)	0.501 (5)	28.673 (8)
343.15	0.009	1.62 (1)	0.884 (5)	12.641 (3)	0.583 (3)	28.585 (9)
343.15	0.010	1.82 (1)	0.882 (4)	12.642 (3)	0.643 (4)	28.535 (9)
343.15	0.012	1.97 (1)	0.899 (3)	12.650 (3)	0.699 (5)	28.520 (8)
343.15	0.020	3.30 (2)	0.937 (4)	12.704 (5)	1.163 (1)	28.17 (1)
343.15	0.027	4.41 (5)	0.963 (8)	12.754 (6)	1.545 (2)	27.92 (1)
343.15	0.038	6.30 (4)	0.958 (2)	12.813 (5)	2.20 (1)	27.33 (1)
343.15	0.056	9.19 (7)	0.975 (3)	12.924 (7)	3.17 (2)	26.59 (1)

Table A.11 continued.

T	x_{N2}	p	y_{N2}	ρ'	ρ''	Δh_v
K	mol/mol	MPa	mol/mol	mol/l	mol/l	kJ/mol
363.15	0.004	0.81 (1)	0.57 (1)	12.135 (6)	0.2814 (3)	27.34 (2)
363.15	0.029	4.43 (4)	0.907 (5)	12.280 (8)	1.481 (2)	26.68 (2)
363.15	0.043	6.44 (5)	0.940 (5)	12.361 (7)	2.13 (2)	26.16 (1)
363.15	0.058	8.67 (7)	0.948 (3)	12.44 (1)	2.84 (2)	25.51 (2)
400	0.010	1.98 (1)	0.546 (4)	11.239 (8)	0.652 (1)	24.52 (2)
400	0.020	3.01 (2)	0.694 (4)	11.27 (1)	0.959 (1)	24.50 (2)
400	0.050	6.7 (2)	0.837 (7)	11.5 (2)	2.07 (5)	23.72 (7)
400	0.060	7.89 (5)	0.843 (2)	11.48 (1)	2.423 (3)	23.18 (2)
400	0.080	10.17 (8)	0.871 (2)	11.57 (2)	3.074 (5)	22.51 (2)
400	0.100	13.31 (5)	0.870 (3)	11.753 (4)	3.99 (1)	21.74 (3)
400	0.160	21.06 (9)	0.891 (4)	12.069 (6)	6.02 (3)	19.53 (4)
400	0.200	26.2 (1)	0.891 (4)	12.281 (7)	7.25 (3)	18.06 (5)
400	0.220	29.1 (2)	0.883 (5)	12.40 (1)	7.93 (5)	17.20 (7)
400	0.240	32.4 (7)	0.870 (6)	12.56 (4)	8.7 (2)	16.30 (9)
400	0.320	43 (1)	0.849 (8)	13.0 (3)	10.7 (8)	13.3 (1)
400	0.400	50 (2)	0.820 (8)	13.4 (4)	12 (1)	10.27 (4)
400	0.420	56 (2)	0.830 (8)	13.7 (4)	13 (1)	9.84 (6)
400	0.500	60 (3)	0.83 (1)	13.9 (6)	13 (1)	7.63 (4)
450	0.100	10.5 (1)	0.64 (1)	9.94 (1)	3.21 (4)	17.1 (1)
450	0.150	14.8 (1)	0.67 (1)	10.07 (2)	4.38 (4)	15.39 (9)
450	0.200	18.5 (2)	0.69 (1)	10.14 (3)	5.35 (8)	13.6 (1)
450	0.220	20.6 (9)	0.67 (3)	10.2 (1)	6.0 (3)	12.6 (5)
450	0.240	22 (1)	0.67 (3)	10.3 (1)	6.4 (4)	11.9 (3)
450	0.260	23 (1)	0.65 (4)	10.3 (1)	6.7 (7)	11 (1)
450	0.300	25 (1)	0.65 (4)	10.2 (2)	7.3 (9)	9.3 (2)
450	0.360	28 (1)	0.59 (5)	10.1 (1)	8.2 (8)	6.1 (1)

Table A.11 continued.

T K	x_{N2} mol/mol	p MPa	y_{N2} mol/mol	ρ' mol/l	ρ'' mol/l	Δh_v kJ/mol
480	0.050	6.6 (2)	0.30 (1)	8.44 (4)	2.44 (8)	13.4 (1)
480	0.100	9.5 (2)	0.39 (1)	8.29 (3)	3.32 (4)	11.8 (1)
480	0.180	12.7 (3)	0.46 (1)	7.94 (1)	4.23 (7)	9.4 (1)
480	0.200	13.3 (3)	0.47 (2)	7.78 (1)	4.39 (6)	8.7 (3)
480	0.240	13.2 (5)	0.47 (4)	7.01 (2)	4.37 (9)	7.0 (1)
480	0.260	13.7 (5)	0.47 (4)	6.88 (2)	4.57 (6)	6.2 (1)

A.2 Simulation details

In this work, the Grand Equilibrium method [17] was used for the VLE calculations of pure acetone. To determine the chemical potential in the liquid, Widom's test molecule method [90] was applied. For this task, molecular dynamics (MD) simulations containing 864 molecules were carried out. Starting from a face-centered cubic lattice, 150 000 time steps were sampled for equilibration with the first 50 000 time steps in the canonical (NVT) ensemble. The production run was performed for 1 000 000 steps. The time step was set to 2 fs and the Gear's predictor corrector integrator was used. The chemical potential was determined by inserting 3456 test molecules every time step into the simulation volume and averaging over all results. For the corresponding vapor, the simulation volume was adjusted to lead to an average number of 500 molecules. After 5 000 initial NVT Monte Carlo (MC) cycles, starting from a face centered cubic lattice, 5 000 equilibration cycles in the pseudo-μVT ensemble were carried out. The length of the production run was 200 000 cycles. For the mixture oxygen + acetone and for nitrogen + acetone below 400 K, the same settings as described above were used for both the liquid and the vapor simulations. For the VLE of nitrogen + acetone at isotherms above 400 K, the NpT+test particle method [18] in an extended version was used. On the liquid side, one MC NpT simulation and one MC NVT simulation were carried out. The NpT simulation at a specified pressure yielded the partial molar volumes, the NVT simulation at the density obtained from the NpT run supplied the chemical potential. For the corresponding vapor, two MC NpT simulations and two MC NVT simulations at slightly different compositions were performed at the specified pressure. Again, the NpT simulations yielded the partial molar volumes. The chemical potentials were obtained from the NVT simulations. Using these data, the VLE at specified temperature and liquid composition was calculated.

For the homogeneous properties of pure acetone, MC simulations in the NpT ensemble were carried out with 864 molecules. Again, starting from a face-centered cubic lattice, 30 000 MC cycles were sampled for equilibration with the first 10 000 cycles in the NVT ensemble. The production run was performed for 200 000 cycles.

Transport properties were determined by equilibrium MD simulations (EMD) following the Green-Kubo formalism [91, 92]. For that task, MD simulations were carried out in two steps. In the first step, one simulation in the NpT ensemble was carried out at the specified temperature and pressure to obtain the density. The system was equilibrated over 100 000 time steps, thereof 50 000 in the NVT ensemble, followed by a production run of 500 000 time steps. In the second step, a NVT ensemble simulation was performed at this temperature and density to calculate the transport properties. The simulations were equilibrated in the NVT ensemble over 200 000 time steps, followed by production runs of 3 500 000 to 7 000 000 time

steps. The simulation length was chosen to obtain at least 20 000 independent time origins of the autocorrelation functions. The sampling length of the autocorrelation functions was chosen to be between 6 und 24 ps, depending on the long-time behavior of the shear viscosity autocorrelation function. The separation between the time origins was chosen such that all autocorrelation functions had decayed at least to 1/e of their normalized value to guarantee their time independence [93].

To calculate the Henry's law constant, the residual chemical potential of the gaseous component i at infinite dilution in the liquid μ_i^∞ was evaluated using Widom's test molecule method. The mole fraction of the solute in the solvent was exactly zero, as required for infinite dilution. MD simulations were carried out in the liquid state at a specified temperature and the pressure was set to the pure substance vapor pressure of the solvent, as described by the molecular model. Therefore, test molecules representing the solute i were inserted into the pure saturated liquid solvent after each time step at random spatial coordinates with random orientations and the potential energy ψ_i between the solute test molecule i and all solvent molecules was calculated. Thus only solute-solvent interactions were sampled. The number of test molecules was 3456 every time step. The residual chemical potential at infinite dilution μ_i^∞ was then obtained by

$$\mu_i^\infty = -k_\mathrm{B}T \ln \langle V \exp(-\psi_i/(k_\mathrm{B}T))\rangle / \langle V \rangle, \tag{50}$$

where V is the volume and the brackets represent the NpT ensemble average.

All thermodynamic properties were determined in the production phase of the simulations on the fly. The cut-off radius was set to 17.5 Å throughout and a center of mass cut-off scheme was applied. Lennard-Jones long-range interactions beyond the cut-off radius were corrected employing angle averaging as proposed by Lustig [94]. Electrostatic interactions were corrected with the reaction field method [20]. The statistical uncertainties of all results were estimated by block averaging according to Flyvbjerg and Petersen [95] and the error propagation law.

B Hexamethyldisiloxane and octamethylcyclotetrasiloxane

B.1 Simulation results

Table B.1: Hexamethyldisiloxane (MM) and octamethylcyclotetrasiloxane (D4): Vapor-liquid equilibrium simulation data for the vapor pressure p, saturated liquid density ρ', saturated vapor density ρ'' and enthalpy of vaporization Δh_v. The number in parentheses indicates the statistical uncertainty in the last digit.

T K	p MPa	ρ' mol/l	ρ'' mol/l	Δh_v kJ/mol
hexamethyldisiloxane (MM)				
288	0.003	4.750 (1)	0.0014 (2)	37.38 (1)
364	0.076 (2)	4.237 (1)	0.0264 (6)	32.01 (1)
431	0.412 (4)	3.703 (3)	0.136 (1)	26.00 (2)
495	1.280 (9)	2.97 (3)	0.483 (3)	16.93 (9)
octamethylcyclotetrasiloxane (D4)				
320	0.0005 (1)	3.1276 (6)	0.00017 (3)	52.22 (2)
330	0.0008 (1)	3.082 (1)	0.00030 (4)	51.02 (2)
335	0.0017 (3)	3.058 (1)	0.0006 (1)	50.40 (3)
435	0.064 (2)	2.651 (1)	0.0187 (5)	40.77 (2)
450	0.098 (2)	2.584 (2)	0.0282 (6)	39.16 (2)
500	0.301 (8)	2.334 (3)	0.086 (2)	33.06 (3)
525	0.47 (1)	2.178 (7)	0.136 (3)	29.33 (7)
550	0.759 (9)	2.015 (8)	0.241 (3)	24.46 (8)

Table B.2: Hexamethyldisiloxane (MM): Homogeneous liquid density ρ. The number in parentheses indicates the statistical uncertainty in the last digit.

T K	p MPa	ρ mol/l	T K	p MPa	ρ mol/l
278.3	44.944	5.081 (1)	367.41	84.848	4.9041 (8)
278.31	24.981	4.9757 (9)	397.2	44.932	4.5478 (7)
278.32	64.896	5.174 (1)	397.2	64.896	4.6849 (6)
278.32	84.832	5.254 (1)	397.2	104.892	4.8953 (7)
278.32	104.898	5.325 (1)	397.2	129.892	4.9997 (6)
278.33	129.898	5.4003 (9)	397.21	24.975	4.367(1)
307.89	24.947	4.822 (1)	397.21	84.834	4.7967 (6)
307.89	44.918	4.9430 (9)	427.05	24.969	4.215 (2)
307.9	64.882	5.045 (1)	427.05	44.930	4.425 (2)
307.9	84.838	5.1334 (9)	427.05	64.894	4.574 (2)
307.9	104.906	5.210 (1)	427.06	84.830	4.694 (2)
307.9	129.902	5.2961 (9)	427.06	104.890	4.794 (1)
337.63	24.967	4.6689 (9)	427.06	129.906	4.906 (1)
337.63	44.930	4.8087 (7)	437	1.359	3.688 (5)
337.63	104.898	5.1009 (6)	377.31	0.996	4.152 (2)
337.63	129.890	5.1928 (8)	278.3	0.874	4.811 (3)
337.64	64.886	4.9206 (6)	448.26	0.203	0.05800 (2)
337.64	84.832	5.0167 (9)	448.26	0.360	0.1087 (1)
367.4	24.977	4.517 (1)	448.26	0.065	0.01770 (1)
367.4	44.946	4.6769 (8)	498.28	0.219	0.05530 (2)
367.4	104.908	4.9957 (8)	278.5	0.101	4.800 (5)
367.4	129.898	5.0952 (7)	320.36	0.101	4.531 (2)
367.41	64.906	4.8018 (8)	357.96	0.101	4.276 (3)

Table B.3: Octamethylcyclotetrasiloxane (D4): Homogeneous liquid density ρ. The number in parentheses indicates the statistical uncertainty in the last digit.

T K	p MPa	ρ mol/l
426.6	140	3.3174 (7)
426.6	100	3.2183 (9)
426.6	60	3.0851 (8)
426.6	10	2.799 (1)
394.9	140	3.3808 (7)
394.9	80	3.227 (1)
394.9	40	3.077 (1)
394.9	10	2.9102 (9)
367.9	60	3.2278 (8)
367.9	10	3.003 (1)
337.7	50	3.279 (1)
337.7	30	3.203 (1)
337.7	10	3.107 (1)
308.2	10	3.202 (1)
323.19	80	3.3900 (4)
323.19	60	3.3364 (8)
323.19	40	3.278 (1)
323.19	20	3.205 (1)
323.19	5	3.125 (1)
303.14	0.1013	3.1822 (9)
313.14	0.1013	3.142 (1)
323.14	0.1013	3.101 (2)
333.13	0.1013	3.066 (1)

Table B.4: Hexamethyldisiloxane (MM): Simulation data for the Speed of sound c. The number in parentheses indicates the statistical uncertainty in the last digit.

T K	p MPa	c 10^3 m/s
365.15	10	0.76 (1)
365.15	14	0.80 (1)
365.15	2	0.68 (3)
365.15	5	0.72 (1)
413.15	10	0.65 (1)
413.15	14	0.69 (1)
413.15	2	0.53 (2)
413.15	5	0.59 (1)
473.15	10	0.50 (1)
473.15	14	0.57 (1)
473.15	2	0.34 (2)
473.15	5	0.42 (1)
573.15	10	0.33 (1)

Table B.5: Octamethylcyclotetrasiloxane (D4): Simulation data for the Speed of sound c. The number in parentheses indicates the statistical uncertainty in the last digit.

T	p	c	T	p	c
K	MPa	10^3 m/s	K	MPa	10^3 m/s
449.96	10.02	0.61 (1)	325	27.61	1.07 (4)
449.96	32	0.82 (1)	325	59	1.27 (6)
449.96	59.98	0.97 (2)	300	2.88	1.03 (8)
425.01	3.08	0.58 (3)	300	10.2	1.09 (7)
425.03	32.18	0.84 (1)	300	24.15	1.19 (5)
425.04	59.8	0.96 (2)	450	0.0389	0.48 (8)
399.82	2.65	0.63 (4)	450	0.0693	0.50 (9)
399.81	10.09	0.73 (3)	465	0.0313	0.43 (7)
399.8	31.8	0.85 (2)	465	0.0749	0.47 (6)
399.8	59.82	1.11 (2)	465	0.1235	0.44 (8)
350	3.01	0.80 (7)	480	0.0427	0.41 (7)
350	10	0.86 (4)	480	0.1092	0.39 (7)
350	32	1.04 (3)	480	0.1654	0.41 (7)
375	60	1.07 (4)	495	0.0275	0.4 (1)
375	2.91	0.65 (8)	495	0.1434	0.36 (6)
375	31.87	0.94 (3)	495	0.2245	0.37 (8)
325	3.09	0.89 (7)			

Table B.6: Hexamethyldisiloxane (MM): Simulation data for the second virial coefficient B.

T K	B l/mol	T K	B l/mol
220	-7.7605	760	-0.2147
230	-6.5832	810	-0.1595
240	-5.6713	860	-0.1126
245	-5.2902	910	-0.0722
250	-4.9493	960	-0.0372
255	-4.643	1010	-0.0065
260	-4.3667	1060	0.0207
270	-3.8887	1110	0.0448
280	-3.4907	1160	0.0664
290	-3.1552	1210	0.0858
300	-2.8691	1260	0.1034
310	-2.6227	1310	0.1194
360	-1.7766	1360	0.1339
410	-1.2861	1410	0.1472
460	-0.9684	1460	0.1594
510	-0.7468	1500	0.1685
560	-0.5837		
610	-0.4588		
660	-0.3602		
710	-0.2804		

Table B.7: Octamethylcyclotetrasiloxane (D4): Simulation data for the second virial coefficient B.

T K	B l/mol	T K	B l/mol
270	-13.4477	600	-1.0755
275	-12.4101	650	-0.8439
280	-11.4934	700	-0.6625
285	-10.6795	750	-0.5166
290	-9.9536	800	-0.3968
300	-8.7181	850	-0.2968
320	-6.8778	900	-0.2120
340	-5.5892	950	-0.1393
360	-4.6468	1000	-0.0762
380	-3.9329	1050	-0.0211
400	-3.3762	1100	0.0276
420	-2.9316	1150	0.0708
440	-2.5693	1200	0.1094
460	-2.2689	1250	0.1442
480	-2.0162	1300	0.1755
500	-1.8009	1350	0.2040
520	-1.6153	1400	0.2300
540	-1.4539	1450	0.2537
560	-1.3122	1500	0.2755
580	-1.1870		

Table B.8: Hexamethyldisiloxane (MM) and octamethylcyclotetrasiloxane (D4): Shear viscosity ν and thermal conductivity λ from molecular simulation. The number in parentheses indicates the statistical uncertainty in the last digit.

T	p	ν	T	p	λ
K	MPa	mPa · s	K	MPa	W/(m · K)
hexamethyldisiloxane (MM)					
275	0.1	0.00 (5)	295.24	10.0384	0.09 (1)
280	0.1	0.45 (3)	295.38	5.7445	0.12 (1)
290	0.1	0.49 (3)	295.50	0.2394	0.09 (1)
295	0.1	0.39 (3)	362.56	0.571	0.082 (8)
315	0.1	0.34 (2)	362.82	6.1037	0.088 (8)
320	0.1	0.31 (2)	362.84	9.7747	0.090 (9)
340	0.1	0.26 (2)	410.97	5.9604	0.073 (7)
350	0.1	0.23 (1)	411.15	9.9404	0.080 (8)
			411.52	0.6564	0.064 (6)
			459.53	1.2543	0.062 (8)
			459.71	5.9081	0.062 (6)
			459.75	9.8705	0.05 (1)
			507.37	2.2843	0.034 (4)
			507.51	5.9243	0.047 (7)
			507.56	10.0179	0.058 (5)
octamethylcyclotetrasiloxane (D4)					
300	0.1	3.0 (2)	290	0.1	0.091 (9)
310	0.1	2.0 (3)	340	0.1	0.09 (1)
330	0.1	1.4 (2)	390	0.1	0.071 (8)
340	0.1	1.3 (2)	440	0.1	0.07 (1)
360	0.1	0.9 (1)			
370	0.1	0.8 (1)			

B.2 Simulation details

The Grand Equilibrium method [17] was used for the VLE calculations. To determine the chemical potential of pure MM and D4 in the liquid, gradual insertion [17, 89] was used for the simulations at 287 K, while for higher temperatures, Widom's test molecule method [90] was applied. For the liquid run, MC simulations in the NpT ensemble were performed using 864 molecules. 70 000 MC cycles were sampled for equilibration with the first 30 000 time steps in the canonical (NVT) ensemble. The production run was performed for 400 000 steps. The chemical potential using Widom's test molecule method was determined by inserting 3 456 virtual molecules into the simulation volume and averaging over all results. For the corresponding vapor, the simulation volume was adjusted to lead to an average number of 500 molecules. After 5 000 initial NVT Monte Carlo (MC) cycles, starting from a face centered cubic lattice, 5 000 equilibration cycles in the pseudo-μVT ensemble were carried out. The length of the production run was 200 000 cycles.
For the homogeneous properties of MM and D4, MC simulations in the NpT ensemble were carried out with 864 molecules. 30 000 MC cycles were sampled for equilibration with the first 10 000 cycles in the NVT ensemble. The production runs were performed for 200 000 cycles.
To calculate the transport properties, in the first step, one simulation in the NpT ensemble was carried out at the specified temperature and pressure to obtain the density. The system was equilibrated over 100 000 time steps, thereof 50 000 in the NVT ensemble, followed by a production run of 500 000 time steps. In the second step, a NVT ensemble simulation was performed at this temperature and density to calculate the transport properties. The simulations were equilibrated in the NVT ensemble over 200 000 time steps, followed by production runs with lengths between 3 500 000 to 7 000 000 time steps. The simulation length was chosen to obtain at least 20 000 independent time origins of the autocorrelation functions. The sampling length of the autocorrelation functions was chosen to be between 6 und 24 ps, depending on the long-time behavior of the shear viscosity autocorrelation function.

C Decafluorobutane

C.1 Simulation results

Table C.1: Decafluorobutane: Vapor-liquid equilibrium simulation data for the vapor pressure p, saturated liquid density ρ', saturated vapor density ρ'' and enthalpy of vaporization Δh_v. The number in parentheses indicates the statistical uncertainty in the last digit.

T	p	ρ'	ρ''	Δh_v
K	MPa	mol/l	mol/l	kJ/mol
190	0.0008 (1)	7.838 (1)	0.0008 (1)	30.516 (8)
210	0.0034 (3)	7.572 (3)	0.0019 (2)	28.97 (1)
225	0.0120 (6)	7.369 (3)	0.0065 (3)	27.81 (1)
250	0.06 (1)	7.003 (3)	0.029 (7)	25.78 (2)
264	0.08 (2)	6.792 (3)	0.039 (7)	24.70 (1)
280	0.15 (1)	6.535 (6)	0.068 (5)	23.31 (2)
301.01	0.31 (1)	6.197 (6)	0.141 (6)	21.35 (2)
333.15	0.73 (1)	5.58 (1)	0.335 (6)	17.79 (3)
358.15	1.29 (1)	4.91 (2)	0.633 (7)	13.95 (6)

Table C.2: Decafluorobutane: Simulation data for the second virial coefficient B.

T	B
K	l/mol
193	-2.7635
220	-1.8794
283	-0.9692
303	-0.8169
323	-0.6964
373	-0.4833
463	-0.2642
522	-0.1765
650	-0.0564
800	0.0243
1000	0.0873
1200	0.1259
1400	0.1518

Table C.3: Decafluorobutane: Simulation data for the speed of sound c. The number in parentheses indicates the uncertainty in the last digit.

T	p	c
K	MPa	m/s
272	0.1	94 (3)
278	0.1	95 (3)
288	0.1	99 (4)
298	0.1	100 (2)
305	0.1	102 (3)

C.2 Simulation details

The Grand Equilibrium method [17] was used for the VLE calculations. To determine the chemical potential, gradual insertion [89, 153] was used for temperatures $T \leq 225$ K, while for higher temperatures, Widom's test molecule method [90] was applied. For gradual insertion, MC simulations in the NpT ensemble were performed using 864 molecules. 30 000 MC cycles were sampled for equilibration with the first 10 000 time steps in the canonical (NVT) ensemble. The production run was performed for 120 000 steps. For Widom's test molecule method, MD simulations using 864 molecules were performed. 30 000 time steps were sampled for equilibration with the first 10 000 time steps in the canonical (NVT) ensemble. The production run was performed for 150 000 steps. The time step was set to 2 fs. For the corresponding vapor, the simulation volume was adjusted to lead to an average number of 500 molecules. After 10 000 initial NVT MC cycles, 15 000 equilibration cycles in the pseudo-μVT ensemble were performed. The length of the production run was 150 000 cycles.

D Mixture of carbon dioxide + 2,2-dimethyl-1-propanol

D.1 Experimental results

Table D.1: Experimental vapor-liquid equilibrium data along the saturated liquid line of the mixture CO_2+ 2,2-dimethyl-1-propanola generated in this work. The number in parentheses indicates the uncertainty in the last digit.

T	p	x_{CO2}
K	MPa	mol/mol
333.2	5.09 (1)	0.280 (2)
333.2	5.08 (1)	0.288 (2)
333.2	6.63 (1)	0.405 (2)
333.2	8.07 (1)	0.515 (3)
333.2	9.04 (1)	0.629 (3)
333.2	10.17 (1)	0.788 (4)
333.2	10.66 (1)	0.853 (5)
333.2	10.54 (1)	0.861 (5)
353.2	5.33 (1)	0.267 (1)
353.2	5.87 (1)	0.294 (2)
353.2	7.33 (1)	0.366 (2)
353.2	9.43 (1)	0.492 (3)
353.2	11.07 (1)	0.607 (3)
353.2	12.42 (1)	0.764 (4)
353.2	12.79 (1)	0.837 (5)
353.2	12.80 (1)	0.840 (5)

E Hydrazine and its derivatives

E.1 Simulation results

Table E.1: Hydrazine, monomethylhydrazine, dimethylhydrazine: Vapor-liquid equilibrium simulation data for the vapor pressure p, saturated liquid density ρ', saturated vapor density ρ'' and enthalpy of vaporization Δh_v. The number in parentheses indicates the statistical uncertainty in the last digit.

T K	p MPa	ρ' mol/l	ρ'' mol/l	Δh_v kJ/mol
hydrazine				
329.6	0.0123 (5)	30.571 (9)	0.0045 (2)	45.36 (2)
391.4	0.132 (5)	28.61 (1)	0.042 (1)	41.40 (2)
473.8	1.0 (1)	25.73 (1)	0.28 (3)	35.67 (1)
556.2	4.2 (1)	22.20 (2)	1.14 (3)	28.19 (3)
618	9.42 (9)	18.37 (5)	2.96 (3)	19.48 (7)
monomethylhydrazine				
285	0.003 (4)	19.116 (3)	0.001 (2)	39.0 (1)
298.15	0.007 (7)	18.766 (4)	0.003 (4)	38.30 (1)
338.73	0.041 (1)	18.080 (4)	0.0147 (3)	36.16 (1)
355.65	0.072 (1)	17.755 (3)	0.0247 (4)	35.30 (1)
360.65	0.087 (1)	17.652 (3)	0.0295 (5)	35.02 (1)
365.65	0.101 (2)	17.543 (3)	0.0339 (5)	34.75 (1)
366.49	0.109 (2)	17.532 (4)	0.0367 (6)	34.71 (1)
383.15	0.178 (2)	17.184 (5)	0.0577 (8)	33.79 (1)
394.27	0.244 (3)	16.956 (4)	0.078 (1)	33.18 (1)
411	0.360 (4)	16.596 (5)	0.111 (1)	
449.83	0.846 (4)	15.713 (6)	0.249 (3)	29.81 (2)
500	2.05 (1)	14.44 (1)	0.594 (3)	26.08 (2)
550	4.14 (2)	12.89 (2)	1.260 (5)	21.22 (4)
dimethylhydrazine				
249.83	0.0012 (2)	14.122 (7)	0.0006 (1)	38.55 (3)
269.04	0.0040 (4)	13.800 (8)	0.0018 (2)	37.19 (4)
293.1	0.016 (1)	13.382 (6)	0.0066 (4)	35.48 (2)
370	0.290 (5)	11.949 (7)	0.101 (2)	29.81 (2)
430	1.20 (1)	10.61 (1)	0.401 (3)	24.49 (3)
500	4.08 (3)	8.42 (4)	1.71 (1)	14.5 (1)

Table E.2: Hydrazine, monomethylhydrazine, dimethylhydrazine: Isobaric heat capacitiy c_p simulation data. The number in parentheses indicates the statistical uncertainty in the last digit.

T / K	c_p / kJ/(mol · K)
hydrazine	
298.16	0.116 (1)
323.15	0.120 (1)
353.11	0.1207 (9)
384.15	0.1231 (9)
monomethylhydrazine	
200	0.104 (2)
240	0.111 (3)
273.15	0.118 (2)
300	0.122 (2)
400	0.133 (1)
dimethylhydrazine	
260	0.147 (3)
273.15	0.153 (4)
285	0.155 (3)
295	0.154 (3)
305	0.155 (3)

Table E.3: Hydrazine, dimethylhydrazine: Liquid densitiy ρ simulation data at 0.1013 MPa. The number in parentheses indicates the statistical uncertainty in the last digit.

T	ρ
K	mol/l
hydrazine	
296.24	31.3903 (3)
366.49	29.2963 (1)
449.83	26.7530 (1)
dimethylhydrazine	
260	13.934 (2)
273.15	13.718 (2)
285	13.516 (2)
295	13.345 (3)
250	14.099 (2)
305	13.169 (3)

Table E.4: Hydrazine, monomethylhydrazine, dimethylhydrazine: Simulation data for the second virial coefficient B.

	hydrazine	monomethylhydrazine	dimethylhydrazine
T	B	B	B
K	l/mol	l/mol	l/mol
300	-1.3688		
310	-1.1947		
320	-1.0531		
330	-0.9363	-0.7984	-0.8290
340	-0.8389	-0.7340	-0.7572
360	-0.6867	-0.6289	-0.6410
380	-0.5743	-0.5466	-0.5510
400	-0.4888	-0.4807	-0.4796
450	-0.3457	-0.3621	-0.3524
500	-0.2588	-0.2834	-0.2685
550	-0.2011	-0.2275	-0.2091
600	-0.1605	-0.1858	-0.1648
650		-0.1536	
700			-0.1033
800	-0.0744	-0.0897	-0.0625
900		-0.0627	-0.0337
1000	-0.0363	-0.0425	-0.0122
1100	-0.0244	-0.0270	0.0045
1200	-0.0152	-0.0147	0.0176
1300	-0.0079	-0.0047	0.0283
1400	-0.0020	0.0035	0.0371
1500	0.0029	0.0104	0.0446

Table E.5: Hydrazine: Simulation data for the shear viscosity ν of liquid hydrazine. The number in parentheses indicates the statistical uncertainty in the last digit.

T	ν
K	10^{-3} Pa · s
300	1.6 (1)
350	0.7 (1)
400	0.54 (6)
315	1.2 (1)

Table E.6: Water + hydrazine: Vapor-liquid equilibrium simulation data for the vapor pressure p and the water mole fraction y_{H2O} in the vapor phase. The number in parentheses indicates the statistical uncertainty in the last digit.

T	x_{H2O}	p	y_{H2O}
K	mol/mol	MPa	mol/mol
388.25	0.6921	0.080 (1)	0.872 (6)
388.85	0.1065	0.092 (6)	0.016 (1)
389.95	0.2072	0.085 (4)	0.060 (4)
391.35	0.2558	0.084 (4)	0.089 (5)
391.45	0.6019	0.073 (3)	0.73 (3)
392.65	0.4062	0.076 (2)	0.273 (8)
393.35	0.4676	0.077 (3)	0.39 (2)

Table E.7: Monomethylhydrazine + water: Vapor-liquid equilibrium simulation data for the vapor pressure p and the monomethylhydrazine mole fraction $y_{CH3-N2H3}$ in the vapor phase. The number in parentheses indicates the statistical uncertainty in the last digit.

T	$x_{CH3-N2H3}$	p	$y_{CH3-N2H3}$
K	mol/mol	MPa	mol/mol
365.65	1	0.1009	0
373.15	0	0.0923	1
376.29	0.3796	0.1093 (4)	0.5844 (2)
368	0.6551	0.1001 (4)	0.8189 (7)
369	0.5995	0.1012	0.8005 (7)
372	0.5	0.1013	0.7193 (8)
377.5	0.1667	0.1004 (3)	0.2175 (2)
378	0.2002	0.1027 (3)	0.2941 (2)

Table E.8: Dimethylhydrazine + water: Vapor-liquid equilibrium simulation data for the vapor pressure p and the dimethylhydrazine mole fraction $y_{(CH3)2-N2H2}$ in the vapor phase. The number in parentheses indicates the statistical uncertainty in the last digit.

T	$x_{(CH3)2-N2H2}$	p	$y_{(CH3)2-N2H2}$
K	mol/mol	MPa	mol/mol
339.04	0.8148	0.096 (3)	0.952 (2)
342.56	0.6632	0.099 (3)	0.916 (3)
345.17	0.5706	0.109 (4)	0.900 (4)
349.63	0.4653	0.109 (5)	0.858 (7)
356.58	0.3102	0.119 (9)	0.78 (2)
359.77	0.2442	0.123 (9)	0.72 (2)
366.13	0.1748	0.113 (8)	0.55 (3)
336.7	0.8727	0.092 (2)	0.967 (1)
351.3	0.4005	0.105 (8)	0.82 (1)

Table E.9: Dimethylhydrazine + hydrazine: Vapor-liquid equilibrium simulation data for the vapor pressure p and the dimethylhydrazine mole fraction $y_{(CH3)2-N2H2}$ in the vapor phase. The number in parentheses indicates the statistical uncertainty in the last digit.

T	$x_{(CH3)2-N2H2}$	p	$y_{(CH3)2-N2H2}$
K	mol/mol	MPa	mol/mol
337.95	0.907	0.099 (1)	0.9736 (5)
341.15	0.725	0.097 (1)	0.917 (1)
346.35	0.4717	0.100 (3)	0.834 (5)
351.95	0.285	0.102 (2)	0.765 (6)
355.95	0.2185	0.111 (6)	0.72 (2)
363.35	0.151	0.137 (4)	0.70 (1)
367.75	0.118	0.148 (4)	0.65 (1)
379.55	0.048	0.17 (1)	0.49 (4)

Table E.10: Vapor-liquid equilibrium simulation data for the vapor pressure p of the systems ammonia + hydrazine, ammonia + monomethylhydrazine and ammonia + dimethylhydrazine. The number in parentheses indicates the statistical uncertainty in the last digit.

T	x_{NH3}	p	T	x_{NH3}	p
K	mol/mol	MPa	K	mol/mol	MPa
ammonia + hydrazine			ammonia + dimethylhydrazine		
278.12	0.3056	0.22 (2)	253.17	0.6227	0.153 (3)
278.12	0.0775	0.06 (2)	253.17	0.3194	0.069 (3)
278.12	0.235	0.18 (2)	273.15	0.3958	0.203 (3)
298.16	0.1551	0.20 (2)	273.15	0.4803	0.249 (3)
298.16	0.0556	0.09 (2)	293.14	0.1296	0.114 (3)
313.22	0.1134	0.20 (2)	293.14	0.2002	0.188 (3)
313.22	0.0405	0.08 (2)	293.14	0.2384	0.218 (3)
313.22	0.0799	0.14 (2)			
ammonia + monomethylhydrazine					
253.17	0.1308	0.025 (4)			
273.14	0.1157	0.052 (4)			
273.14	0.0822	0.042 (4)			
293.14	0.0972	0.097 (4)			
293.14	0.1204	0.101 (4)			
293.14	0.0567	0.049 (4)			

Table E.11: Henry's law constant H_i of argon and of nitrogen in hydrazine. The number in parentheses indicates the statistical uncertainty in the last digit.

argon		nitrogen	
T	H_{Ar}	T	H_{N2}
K	10^3 MPa	K	10^3 MPa
278.15	11.703 (2)	278.15	20.350 (3)
280	11.823 (2)	281.50	20.149 (3)
283	11.350 (2)	285	19.428 (2)
285	10.949 (1)	288	17.862 (3)
288	10.182 (1)	291.50	17.617 (2)
290	9.870 (1)	295.50	15.770 (2)
295	8.802 (1)	300	15.061 (2)
298	8.271 (1)	303	13.820 (2)
300	8.2156 (9)	308.18	12.597 (2)
303	7.916 (1)		
308.18	7.270 (1)		

Table E.12: Henry's law constant H_i of argon and of nitrogen in monomethylhydrazine. The number in parentheses indicates the statistical uncertainty in the last digit.

argon		nitrogen	
T	H_{Ar}	T	H_{N2}
K	10^3 MPa	K	10^3 MPa
253.24	0.7148 (4)	253.24	1.5729 (7)
258.15	0.7094 (4)	258.15	1.5437 (6)
263.15	0.7002 (4)	263.15	1.5056 (5)
268.15	0.6842 (3)	268.15	1.4405 (5)
273.15	0.6498 (3)	273.15	1.3543 (5)
278.14	0.6340 (3)	278.14	1.2922 (4)
283.14	0.6204 (3)	283.14	1.2510 (4)
288.14	0.5972 (2)	288.14	1.1808 (3)
293.14	0.5770 (2)	293.14	1.1242 (3)
298.14	0.5642 (2)	298.14	1.0928 (3)

Table E.13: Henry's law constant H_i of argon, of nitrogen and of carbon monoxide in dimethylhydrazine. The number in parentheses indicates the statistical uncertainty in the last digit.

argon		nitrogen		carbon monoxide	
T	H_{Ar}	T	H_{N2}	T	H_{CO}
K	10^3 MPa	K	10^3 MPa	K	10^3 MPa
253.05	0.155 (2)	253.05	0.3333 (5)	258.16	0.1972 (2)
258.08	0.1564 (2)	258.15	0.3225 (2)	268.16	0.1964 (2)
263.10	0.1546 (2)	263.15	0.3115 (2)	276.00	0.1912 (2)
268.12	0.1541 (1)	268.15	0.3068 (2)	288.16	0.1844 (2)
273.15	0.1534 (1)	276.00	0.2893 (2)	298.16	0.1807 (1)
278.15	0.1528 (1)	283.05	0.2861 (2)		
283.15	0.1509 (1)	287.15	0.2818 (1)		
288.16	0.1503 (1)				
293.16	0.1475 (1)				

E.2 Simulation details

The Grand Equilibrium method [17] was used to calculate VLE data for all systems. For the liquid, Monte-Carlo simulations were performed in the isobaric-isothermal (NpT) ensemble. There, the number of molecules was 800 for pure fluids and 864 for mixtures. The gradual insertion method [89, 153] was used to calculate the chemical potential for all binary systems with water. For all other binary systems, Widom's test molecule method [90] was used. 30 000 Monte Carlo cycles, with the first 10 000 cycles in the canonical (NVT) ensemble, were performed for equilibration and 100 000 for production. Each cycle contained a number of attempts to displace and rotate molecules equal to the actual number of molecules N plus one volume move. Every cycle, $10 \times N$ fluctuating state change moves, $10 \times N$ fluctuating particle translation/rotation moves, and $50 \times N$ biased particle translation/rotation moves were sampled to determine the chemical potential. For the corresponding vapor, Monte Carlo simulations in the pseudo-μVT ensemble were performed. The simulation volume was adjusted to lead to an average number of 500 molecules in the vapor phase. After 10 000 initial NVT Monte Carlo cycles, 25 000 equilibration cycles in the pseudo-μVT ensemble were sampled. The length of the production run was 100 000 cycles. The cut-off radius was set to 15 Å throughout.

Transport properties were determined by equilibrium MD simulations following the Green-Kubo formalism [91, 92]. The system was equilibrated over 70 000 time steps, thereof 20 000 in the NVT ensemble, followed by a production run of 500 000 time steps. In the second step, a NVT ensemble simulation was performed at this temperature and density to calculate the transport properties. The simulations were equilibrated in the NVT ensemble over 100 000 time steps, followed by production runs of 1 000 000 time steps. The shear viscosity was calculated with 5 000 independent time origins of the autocorrelation functions. The sampling length of the autocorrelation functions was 2 000 time steps.

List of publications

Prior to the dissertation work:

- Vrabec, J.; Baumhögger, E.; Elsner, A.; Horsch, M.; Liu, Z.; Miroshnichenko, S.; Nazdrajic, A.; Windmann, T. *Molecular dynamics simulation of fluid dynamics on the nanoscale*, in A. Kuzmin (Ed.): Sixth International Conference on Computational Fluid Dynamics, 106-107, VVM Publishing Co., St. Petersburg, 2010.
- Horsch, M.; Lin, Z.; Windmann, T.; Hasse, H.; Vrabec, J. *The air pressure effect on the homogeneous nucleation of carbon dioxide by molecular simulation*. Atmos. Res. **2011**, 101, 519-526.
- Gorenflo, D.; Baumhögger, E.; Windmann, T.; Herres, G. *Nucleate pool boiling, film boiling and single-phase free convection at pressures up to the critical state. Part I: Integral heat transfer for horizontal copper cylinders*. Int. J. Refrig. **2010**, 33, 1229-1250.
- Gorenflo, D.; Baumhögger, E.; Windmann, T.; Herres, G. *Nucleate pool boiling, film boiling and single-phase free convection at pressures up to the critical state. Part II: Circumferential variation of the wall superheat for a horizontal 25 mm copper cylinder*. Int. J. Refrig. **2010**, 33, 1251-1263.
- Gorenflo, D.; Baumhögger, E.; Windmann, T.; Herres, G. *Ebullición libre nucleada, ebullición pelicular y convección libre monofásica a presiones próximas al estado crítico. Parte Ia: Transmisión integral de calor de la superficie externa de cilindros horizontales de cobre a refrigerantes en ebullición nucleada y pelicular*. Frío-Calor-Aire Acondicionado **2011**, 436, 26-40.
- Gorenflo, D.; Baumhögger, E.; Windmann, T.; Herres, G. *Ebullición libre nucleada, ebullición pelicular y convección libre monofásica a presiones próximas al estado crítico. Parte Ib: Transmisión integral de calor de la superficie externa de cilindros horizontales de cobre a refrigerantes en ebullición nucleada y pelicular*. Frío-Calor-Aire Acondicionado **2011**, 437, 30-40.
- Gorenflo, D.; Baumhögger, E.; Windmann, T.; Herres, G. *Ebullición libre nucleada, ebullición pelicular y convección libre monofásica a presiones próximas al estado crítico. Parte II: Transmisión integral de calor de la superficie externa de cilindros horizontales de cobre*

a refrigerantes en ebullición nucleada y pelicular. Frío-Calor-Aire Acondicionado **2011**, 438, 28-43.

Publications related to this thesis (Including a statement on the contributions of the author of the present thesis):

- Windmann, T.; Köster, A.; Vrabec, J. *Vapor-liquid equilibrium measurements of the binary mixtures nitrogen + acetone and oxygen + acetone*. J. Chem. Eng. Data **2012**, 57, 1672-1677.
  The author of this thesis studied the mixtures nitrogen + acetone and oxygen + acetone by experiment, where he was assisted by Andreas Köster in the latter case. Moreover, he calculated the Henry's law constants on the basis of the measured data. Finally, he adjusted the Peng-Robinson EOS for both mixtures.

- Elts, E.; Windmann, T.; Staak, D.; Vrabec, J. *Fluid Phase Behavior from molecular simulation: hydrazine, monomethylhydrazine, dimethylhydrazine and binary mixtures containing these compounds*. Fluid Phase Equilib. **2012**, 322-323, 79-91.
  The author developed the force field models of pure hydrazine, monomethylhydrazine and dimethylhydrazine. Moreover, he performed the molecular simulations for the pure fluids and the mixtures including the Henry's law constant. Finally, he adjusted the Peng-Robinson EOS for all mixtures.

- Köster, A.; Nandi, P.; Windmann, T.; Ramjugernath, D.; Vrabec, J. *Vapor-liquid equilibria of ethylene (C2H4) + decafluorobutane (C4F10) at 268 to 298 K from experiment, molecular simulation and the Peng-Robinson equation of state*. Fluid Phase Equilib. **2012**, 336, 104-112.
  The author developed the force field model for pure decafluorobutane and performed the respective molecular simulations assisted by Andreas Köster. Second, he adjusted the Peng-Robinson EOS with the Mathias-Copeman mixing rule for pure decafluorobutane.

- Niethammer, C.; Glass, C.W.; Bernreuther, M.; Becker, S.; Windmann, T.; Horsch, M.; Vrabec, J.; Eckhardt, W. *Innovative HPC methods and application to highly scalable molecular simulation (IMEMO)*. Innovatives Supercomputing in Deutschland **2012**, 10, 68-71.
  The author performed the molecular simulations for the mixture water + hydrazine.

- Eckelsbach, S.; Windmann, T.; Elts, E.; Vrabec, J. *Simulation of liquid-liquid equilibria with molecular models optimized to vapor-liquid equilibria and model development for Hydrazine and two of its derivatives*, in W. E. Nagel, D. B. Kröner and M. M. Resch (Eds.): High Performance Computing in Science and Engineering '12, 451-460, Springer,

Berlin, 2013.
The author developed the force field models of pure hydrazine, monomethylhydrazine and dimethylhydrazine and performed the molecular simulations for the pure fluids and the mixtures. He also adjusted the Peng-Robinson EOS for the mixtures.

- Hsieh, C.-M.; Windmann, T.; Vrabec, J. *Vapor–Liquid Equilibria of CO_2 + C1–C5 Alcohols from the Experiment and the COSMO-SAC Model*. J. Chem. Eng. Data **2013**, 58, 3420–3429.
  The author studied the mixture carbon dioxide + 2,2-dimethyl-1-propanol by experiment.

- Windmann, T.; Linnemann, M.; Vrabec, J. *Fluid Phase Behavior of Nitrogen + Acetone and Oxygen + Acetone by Molecular Simulation, Experiment and the Peng-Robinson Equation of State*. J. Chem. Eng. Data **2014**, 59, 28-38.
  The author developed the force field model of pure acetone and performed the molecular simulations for pure acetone and the mixtures nitrogen + acetone and oxygen + acetone. Moreover, he studied the mixture acetone + nitrogen by experiment assisted by Matthias Linnemann. Finally, he adjusted the Peng-Robinson EOS for the mixtures nitrogen + acetone.

- Glass, C.W.; Reiser, S.; Rutkai, G.; Deublein, S.; Köster, A.; Guevara-Carrion, G.; Wafai, A.; Horsch, M.; Bernreuther, M.; Windmann, T.; Hasse, H.; Vrabec, J. *ms2: A molecular simulation tool for thermodynamic properties, new version release*. Comput. Phys. Commun. **2014**, in press.
  The author implemented the radial distribution function into ms2.

- Thol, M.; Windmann, T.; Rutkai, G.; Dubberke, F.; Span, R.; Vrabec, J. *Helmholtz Equation of state for hexamthyldisiloxane and octamethylcyclotetrasiloxan from molecular simulation and experimental data*, 2014 in preperation.
  The author developed the force field models of pure hexamethyldisiloxane and octamethylcyclotetrasiloxane and performed the respective molecular simulations.

Student theses

The following student theses were prepared under the supervision of the author of the present doctoral thesis in the frame of his research:

- **Tianmin Du**, Überprüfung molekularer Modelle anhand thermodynamischer Stoffeigenschaften von Reinstoffen und Mischungen, BA, 2009
- **Yang Yang**, Überprüfung von molekularen Modellen anhand thermischer und kalorischer Stoffeigenschaften im homogenen fluiden Zustandsgebiet, BA, 2009
- **Roberto Francese**, Erweiterung, Inbetriebnahme und Bewertung der Analysefähigkeit eines Gaschromatographen zur Bestimmung der Zusammensetzung von binären Stoffgemischen, DA, 2010
- **Andreas Köster**, Construction and initial startup of a high pressure vapor-liquid equilibrium apparatus for binary mixtures, BA, 2010
- **Philipp Komodromos**, Inbetriebnahme und Kalibrierung des GC und Messungen des Stoffgemisches Stickstoff und Aceton, StdA, 2011
- **Florian Lorenz**, Experimentelle Bestimmung der Taulinie anhand mehrerer Proben von Stickstoff/Acetongemischen mit einem Gaschromatographen, StdA 2011
- **Philipp Komodromos**, Inbetriebnahme einer Phasengleichgewichtsapparatur und erste Messungen mit Reinstoffen und der binären Mischung Stickstoff + Aceton, DA, 2011
- **Zhiyuan Li**, Molekulare Simulation von Mischungen mit Hydrazin, BA, 2011
- **Tianming Du**, Molekulare Simulation von Stoffsystemen mit Hydrazin und Dimethylhydrazin, StdA 2012
- **Florian Lorenz**, Entwicklung und Konstruktion einer Anlage zur Vermessung von Phasengleichgewichten, Teil 1, StdA, 2012
- **Sven Indermark**, Entwicklung und Konstruktion einer Anlage zur Vermessung von Phasengleichgewichten, Teil 2, StdA, 2012
- **Simon Kimmeyer**, Calibration of a vibrating tube densitometer for density measurement of mixtures with CO2 at high pressures, BA, 2012

- **Torben Borgolte**, Experimentelle Bestimmung der Siededichte von binären Gemischen, BA, 2012
- **Fabian Günter**, Vapor–liquid equilibrium for binary mixtures of ammonia and ionic liquid, BA, 2012
- **Matthias Linnemann**, Vapor-liquid equilibrium measurement of ammonia + ionic liquid mixtures and density determination of pure ionic liquids, BA, 2012
- **Andreas Köster**, Vapor-liquid equilibria of ethylene (C2H4) + decafluorobutane (C4F10) at 268 to 298 K from experiment, molecular simulation and the Peng-Robinson equation of state, StdA, 2012
- **Andreas Köster**, Aufbau, Inbetriebnahme und Funktionstest eines Prüfstandes für ein neu entwickeltes Wärmepumpensystem im besonderen Hinblick auf das System-Regelverhalten, MA, 2012
- **Yang Yang**, Molekulare Simulation von Mischungen mit Siloxanen, StdA, 2013
- **Michael Wabiszczewicz**, Vermessung und Auswertung der Verdampfungsenthalpie der Siloxane Decamethylcyclopentasiloxan (D5), Octamethyltrisiloxan (MDM) und Hexamethyldisiloxan (MM) unter Verwendung eines Differenzkalorimeters, BA, 2014
- **Matthias Linnemann**, Inbetriebnahme und Funktionstest einer Versuchsanlage zur Vermessung von Gas-Flüssig Phasengleichgewichten und erste Messungen mit der Mischung Stickstoff + Aceton unter extremen Bedingungen, StdA, 2014